FINAL REPORT: SEPTEMBER 2017

GLASS COMPOSITION AND SOLUTION SPECIATION EFFECTS ON STAGE III DISSOLUTION

CORY L TRIVELPIECE, JARRETT A RICE AND CARLO G PANTANO
THE PENNSYLVANIA STATE UNIVERSITY
UNIVERSITY PARK, PA 16801

SUMMARY

The goal of this report is to contribute new data and insight to help understand the onset of Stage III dissolution during the long-term storage of high-level nuclear waste. The critical effect of the Stage III transition is a dramatic and unpredictable resumption in the glass dissolution rate from its otherwise low residual value to a much higher rate. The Stage II to Stage III transition is believed to be triggered by some, as yet unidentified, characteristic of the altered glass surface layer and the contacting aqueous solution, both of which depend on glass composition. This transition is enhanced by high pH, and is accompanied by the crystallization of secondary mineral phases. The crystallization probably creates a thermodynamic driving force for the continued high-rate dissolution of the glass, but it is not yet known whether super-saturation and nucleation in solution, crystallization of the amorphous surface layer or a chemical reaction between the altered surface layer and the solution is the primary mechanism. In general, information is lacking about the chemical structure of the altered layer, the speciation of soluble and colloidal species in solution, and the thermodynamic properties of metastable and equilibrium hydrated phases.

A unique feature of our approach is the use of glass fibers for leaching and corrosion testing. The use of fibers provides a uniform geometry and smooth, defect-free surface. Another focus of this study was the role of glass composition in the Stage III transition. The glass compositions of interest transcend the range between SON68 and AFCI because, based on several experimental studies, it is found that SON68 is considerably less susceptible to the Stage III transition when compared to AFCI. Our work also makes extensive use of the International Simple Glass (ISG) which contains only 6 oxide components versus the ~25 oxide components which constitute the more realistic SON68 and AFCI waste-form compositions. We evaluated the results of these studies based upon the evolution of weak-acid and strong-base species in the contacting solution, and where possible, upon the composition of the altered leach layer at the glass-solution interface.

Initially, unannealed ISG fibers were reacted in water, as well as in 1.0 M and 2.0 M NaOH, KOH, and LiOH to artificially trigger Stage III behavior (see Section 1). The fibers in alkaline solutions showed significant alteration, in most cases resulting in complete dissolution of the

5um diameter fibers. During this dissolution, a templated particulate shell formed around the original fiber space with some degree of crystallization occurring within the hollow shell. These transitions varied with the solution conditions, but in general, a process consisting of a dissolving core and a precipitating "hollow tube shell" was observed for all the samples. Interestingly, the solution analyses for these samples indicated almost complete leaching of boron from the fibers in hydroxide solution. XRD was used to characterize any crystalline phases formed during the fiber corrosion reaction and its transition into a tube. Of particular note is the formation of the Ca silicate phases in the $Ca(OH)_2$/KOH as compared to the formation of zeolitic phases in the $Ca(OH)_2$/NaOH.

The high pH conditions used here, whether intrinsic to the glass or created artificially by solution modification, is a key characteristic of Stage III. These results confirm that the amount of crystallization and the formation of specific crystalline phases are strongly dependent on the composition of the concentrated solutions in contact with the glass. These observations inspired a short study of "Mineral Precipitation in Concentrated Aqueous Solutions of Na and Li Silicate Glass" in Section 2 (not yet submitted for publication).

The high pH experiments described above were followed-up with lower pH, longer-term reactions. In Section 3, we describe long-term 90C static corrosion tests using fibers synthesized from the reference International Simple Glass (ISG). These experiments were conducted in four different alkaline solutions varying in initial pH value (pH_i) from 9.5 to 12.5. The pH_i 12.5 experiment transitioned (naturally) to Stage III corrosion in 57 days whereas the lower pH_i experiments have remained at the low residual rate of Stage II for more than one year. The pH_i 12.5 transition from Stage II to Stage III was marked by a decrease in the Al concentration in solution, an increase in the B and Si concentrations in solution, and an increase in the crystallinity of the sample. Solution analyses indicated that whereas the pH_i 9.5 - 11.5 experiments self-buffered to pH values between 9.5 - 9.7 within two days of the initiation of the experiments and remained at those values thereafter, the pH_i 12.5 experiment remained at approximately 12.4 until the transition to Stage III. X-ray diffraction (XRD) confirmed the crystallization of zeolite NaP2 during the transition to Stage III. X-ray photoelectron spectroscopy (XPS) was used to follow evolution of the altered surface layer compositions throughout the experiment and showed distinct differences between the pH_i 12.5 sample and the others, especially with respect to Al. High-resolution TEM analyses of fiber cross-sections clearly revealed two distinct altered surface layers, with the inner most layer (inter-diffusion zone) undergoing disintegration during the Stage III transition of the pH_i 12.5 sample, but the outmost nanoporous gel layer remained intact. Geochemist's Workbench was used to obtain saturation index and speciation modeling, while the altered layer compositions obtained with XPS and the solution analysis data were used to test the model proposed by Jantzen for predicting susceptibility to Stage III based on the structure and composition of the gel-layer. It was found that the structure of the gel layer that forms during the leaching of ISG glass fibers is a function of $pH/[OH^-]$. The layers formed at pH 9.5 and 10.5 tend to enrich in Si, and show a nearly fully polymerized structure. The layer formed at pH 12.5 tends to be depleted in Si, and this yielded a layer structure that was fragmented into chains and rings, presumably bound together by hydrogen bonding of the terminal hydroxyls associated with those chains and rings. These differences in gel layer structure correlate qualitatively with the solution speciation provided by GWB and predictions of the model proposed by Jantzen, et al.

Our next objective was to make glass fibers of various compositions based upon quantitative blending of two reference waste glasses which are comprised of 26 oxides with 20 common components between them. The first glass is a French waste form, referred to as SON68. The other is a waste glass developed by the United States Department of Energy for the Advanced Fuel Cycle Initiative (AFCI). SON68 has been shown to release markedly larger quantities of glass species into the contacting solution, but in the long term is consistently the more durable of the two glasses, while AFCI is more susceptible to this Stage-III transition. For this reason, these two reference (simulated) waste glasses were studied to explore compositional differences that could help explain triggers for Stage III. To do this, combinations of the two glasses were melted together in ratios by weight of 75% SON68 to 25% AFCI, 50% SON68 to 50% AFCI, and 25% SON68 to 75% AFCI. Unfortunately, the time and costs required to fabricate these blended glasses into fibers for corrosion were under-estimated in the original proposal and could not be accomplished. Instead, the blended glasses and pure end-point glasses were subjected to modified PCT tests at 90C. An additional set of blended glasses were made with excess aluminum for both PCT testing and for tests at very high SA/V (25,000 m^{-1} versus 2,000 m^{-1} in the PCT test).

These three unique and systematically varied sets of glass compositions, synthesized by blending SON68 and AFCI (the primary "model glasses" in US studies of waste glass degradation), confirmed the critical importance of SA/V and Al content in promoting the transition to Stage III. The three blends that contained ~2.5 ^{w}/o excess Al_2O_3 and were tested at an SA/V of 25,000 m^{-1}, were the only samples which exhibited the transition to Stage III within the three-year period of this study. Moreover, the solution concentration of Al at the onset of the transition was between 50 and 60 ppm for all three compositions, suggesting a tipping point when the Al concentration reaches this maximum in solution. Equally interesting was the time sequence of the transition for the three glasses; the 25% SON68 composition occurred after 420 days, the 50% SON68 composition after 778 days and the 75% SON68 composition after 905 days. The associated solution data conformed to the ALTGLASS model proposed by Jantzen, while characterization of the sample surfaces suggested the possibility of a smectite OH barrier at the glass/solution interface that formed in proportion to the SON68 concentration in the glass. Altogether, the results suggest the presence of a critical element or elemental concentration in the AFCI glass, or chemical species in solution, that triggers the transition. It is likely associated with Al reaction products in the altered layer, the solution or both. Unfortunately, the identification of this critical constituent or reaction product could not be identified amongst the 20 common and 16 different oxides which constitute SON68 and AFCI.

Section 1. Glass Corrosion Studies Using Glass Fiber

Section 2. Mineral Precipitation in Concentrated Aqueous Solutions of Na and Li Silicate Glass

Section 3. Corrosion of ISG Fibers in Alkaline Solutions

Section 4. Corrosion Behavior of SON68-AFCI Blends: Composition Effects on Stage III

SECTION 1. GLASS CORROSION STUDIES USING GLASS FIBER

CORY L TRIVELPIECE, JARRETT A RICE AND CARLO G PANTANO
MATERIALS RESEARCH INSTITUTE
THE PENNSYLVANIA STATE UNIVERSITY
UNIVERSITY PARK, PA 16801

Most of the work reported here used ISG fibers fabricated with two different sources of the ISG glass: one batch prepared at Penn State (under our previous NEUP Program) and the other obtained from MoSci Glass (prepared for the International Glass Corrosion Group). The first set of fiber was made with the Penn State ISG glass batch with a fiber diameter of ~2.5 um. Several corrosion experiments were performed with these fibers in high pH alkaline solutions. This first set of fiber experiments also revealed unexpected density and annealing effects. The second set of ISG fiber was made with the MoSci glass at a diameter of ~5um. This fiber has been used to study the density and annealing of fibers, and to compare their behavior with glass powder. This fiber is also being used to perform single pass flow through and long term static corrosion for direct comparison of corrosion behavior for fibers versus powders. The ISG fibers will provide a reference material for subsequent study of the blended SON68-AFCI fiber compositions.

2.1. EXPERIMENTAL PROCEDURES

The International Simplified Glass (ISG) was produced at Penn State by melting batches at 1350 ºC for three hours. Two separate batches were made, one for fiber and one for powder. Both batches were poured and cooled on a stainless steel plate at room temperature. The glass melt used for the fiber fabrication was then broken into smaller pieces with an average size of 1 cm x 1 cm. The cooled melt for the powder form was broken into similarly sized pieces and then crushed in a Retsch disc-mill until a very fine powder was produced. The fine powders were used to prepare concentrated solutions of ISG glass for crystal precipitation studies.

A 50 kg batch of the ISG was also produced in May 2012 by MoSci Corporation (Rolla, MO, USA) and cast into 500 gram glass ingots. The 500g ingots were annealed 569°C for 6 hrs and then cooled at 1 K/min to room temperature.

The glass pieces for the fiber production (both the Penn State and MoSci ISG) were loaded into a single-tip Pt bushing mounted to a fiber draw tower. The drawing temperature was 1125 ºC while the rotating drum spool pulled the fiber at ~1050 rpm to obtain 2.5 um fiber, and at ~350 rpm to obtain 5um fiber. The diameter of the fibers was determined using SEM micrographs of the untreated fiber which were quantitatively analyzed with ImageJ software.

A series of annealing experiments were performed to understand the relative state of the fibers and glass powders, and ultimately, to bring the fiber density to the same value as the powder density. To anneal the fiber or glass (powder precursor), the samples were placed in an oven at room temperature on a clean piece of alumina refractory and heated at ~9 K min^{-1} to 569°C, the temperature that MoSci Inc. used to anneal the ISG glass blocks. The samples soaked at 569°C for 2 hours before being cooled back to room temperature at 1 K min^{-1}. While the original Mo-Sci ingots were annealed for 6 hours before cooling at the aforementioned rate, we assumed that the small size and limited amount of fiber and glass (<3g) used in these experiments would require only a portion of that time in order to achieve the same degree of structural relaxation.

The density measurements of the fibers and powders were made via He-pycnometry; for each sample, ten cycles were performed to obtain the density. There is considerable variability in the density measurements for the fibers. Our procedures for sampling and handling the fibers for He-pycnometry are being studied and modified to reduce the measurement error and to better understand the density variability. Surface area analysis was performed with BET.

^{11}B Direct Polarization NMR (14.1 Tesla, 600 MHz 1H Frequency) was performed on selected fibers and powders to correlate changes in density with glass structure changes associated with boron coordination.

Selected fiber corrosion experiments were carried in elevated pH solutions. One and two molar hydroxide solutions were produced from ASTM Type I water and solid hydroxide pellets: NaOH, LiOH, KOH, and $Ca(OH)_2$. Fiber experiments were also carried out with weaker KOH and NaOH solutions at pH 11 and 12.5, as well as pH 12.5 $Ca(OH)_2$. The fibers were cut and placed into 60 mL PFA digestion vessels (Savillex ®) and the various solutions were added. The fibers were corroded in these solutions at 90ºC, removed from their respective containers, rinsed, and then oven dried at 70ºC. The objective of these experiments was to observe the manner in which the fibers corrode, to gauge the kinetics of their total dissolution and to begin to establish a data base of end-point crystalline phases (analogous to the VHT test).

The two main analysis techniques used for the characterization of corroded fibers thus far have been field-emission scanning electron microscopy (FESEM) and X-ray diffraction (XRD). For observations using FESEM, the dried fibers are placed in a cross section, SEM sample holder and cut along the diameter so that cross sectional images can be acquired. The remainder of the dried sample is crushed for XRD powder analysis.

2.3.1 Characterization of ISG fibers

The target composition and measured compositions of various ISG batches and fibers are presented in Table 2.1. The measured compositions for the PSU ISG powder and fiber are deficient in ZrO_2, but for the purposes of these preliminary experiments, we proceeded. The compositional analysis of the MoSci fiber is pending.

Table 2.1: ISG target compositions (in Mol% and Weight%) along with ICP-AES measured compositions for the MoSci ISG and PSU ISG.

Oxide	Batch Mol%	Batch Weight %	MoSci ISG Measured w%	PSU ISG Measured w%	PSU ISG Fiber Measured w%	MoSci ISG Fiber Measured w%
SiO_2	60.1	56.2	56.1	55.6	54.5	
B_2O_3	16.0	17.3	17.7	16.1	15.8	
Na_2O	12.6	12.2	12.6	11.2	11.2	
CaO	5.7	5.0	4.6	4.8	4.9	
Al_2O_3	3.8	6.1	6.0	6.0	6.2	
ZrO_2	1.7	3.3	3.2	0.9	1.7	

Table 2.2 presents density and related characteristics of the glass powders and fibers. Surprisingly, the density of the glass powder (PSU ISG) is comparable to the as-drawn PSU-ISG fiber. Since the powder was made from glass that was slow cooled, but not annealed, a difference in density was expected. The fiber and powder were subsequently annealed at 569C for 2 hrs. The annealed fiber density reached 2.55 g/cm^3 while the annealed powder density only 2.49 g/cm^3. The independent NMR analyses confirm that the fiber structure was modified by the annealing, and the decreased amount of [BO_3] coordination is consistent with the increase in density. The higher density for the annealed fiber is attributed to the difference in composition between the PSU ISG powder and fiber, as shown in Table 2.1 - the PSU ISG was made in two separate batches, and based on the ICP-AES analysis, the ISG batch used to make the powder was much more deficient in Zr than the batch used to make the fiber.

Table 2.2 also presents density and other physical characteristics of the MoSci ISG and fibers fabricated with it. For this set of density data, multiple samples were tested and repeat measurements were made because of the surprising results obtained in measuring the first set of fibers. Again, though, there is not a significant difference between the density of the as-drawn fiber (2.49 - 2.51 g/cm^3), and the annealed glass powder precursor to the fiber (2.52 g/cm^3). Several fiber anneals were performed, and these yielded a range of density between 2.50 g/cm^3 and 2.54 g/cm^3, again showing a higher density for annealed fiber than for annealed powder. Considering that structural relaxation in borosilicate glasses requires a coordination change in the network, as confirmed above, there could be a surface tension effect acting on the small diameter fibers to enhance densification. Additional study of these effects with NMR is underway.

For the corrosion studies to be performed in this project, it is desirable to eliminate any density effects on leaching and dissolution. The results of these density studies show that the ISG fibers can, in fact, be annealed to a density equivalent to the ISG bulk glass for comparative testing.

Table 2.2: Physical and structural characteristics of fibers.

	Form	Diameter (μm)	BET S.A. (m^2/g)	Density (g/cm^3)	NMR ($B_{[3]}/B_{[3]}+B_{[4]}$)
PSU-ISG	**Fiber**	2.50	0.5656	2.46	0.63
	Annealed Fiber	2.46	0.5577	2.55	0.45
	Slow-Cooled Glass (for powder)	n/a	0.3406	2.46	0.48
	Annealed Glass (for powder)	n/a	n/a	2.49	
MoSci-ISG	**Fiber**	5.16	0.3256	2.49 - 2.51	pending
	Annealed Fiber	4.95	0.307	2.50 - 2.54	pending
	Annealed Glass (for powder)	n/a	pending	2.52	pending
	Re-Annealed Glass (for powder)	n/a	n/a	2.52	

2.3.2 Fiber Dissolution and Crystallization at High pH

The PSU-ISG (un-annealed) fibers were reacted in 1.0 M and 2.0 M NaOH, KOH, LiOH and H_2O and then extracted and investigated with FESEM and XRD. Upon removal from their respective digestion vessels, significant transformation of the fiber shapes and structural integrity was observed. The fibers were congealed and could disintegrate with relative ease, although still retaining the fiber shape and altered structure after oven drying, as shown in Figure 2.1. In comparison to simple water attack, the high pH alteration of the fibers is unique, in most cases resulting in templated hollow core fibers, with some degree of crystallization occuring during the alteration. The high pH condition, whether intrinsic to the glass or created artificially by solution modification (Fortner), is a key characteristic of Stage III. These experiments aimed to characterize the end point of the transition for comparison to long term leaching studies and VHT tests.

The FESEM analyses revealed varying degrees of alteration depending on the starting solution as shown in Figure 2.1. The NaOH and KOH fiber samples show a dissolved hollow core with a particulate shell surrounding the original fiber space. Measurements of these features indicate that the hollow core of the NaOH corroded fiber is 1.85 ± 0.12 μm and the outside diameter of the shell is 3.98 ± 0.19 μm. The KOH corroded fibers have a hollow core diameter of 1.38 ± 0.19 μm and an outer shell diameter of 4.07 ± 0.16 μm. Some of the KOH fibers showed a very faint middle layer ring between the hollow core and the outside of shell. The diameter of this layer was measured to be 2.78 ± 0.17 μm. The LiOH corroded fiber does not exhibit a well-developed core and shell, suggesting that the kinetics of the dissolution and precipitation reactions differ in the presence of Li, and this correlates with the binary glass study reported in Part 1. The control sample that was corroded in R.O. water for 400 h is also shown in Figure 2.1 for comparison, but evidence of reaction is not visible in the SEM. Interestingly, the solution analyses for these samples indicates almost complete leaching of boron from the fibers in hydroxide solution, and about 50% leaching of all the boron in the water reacted samples.

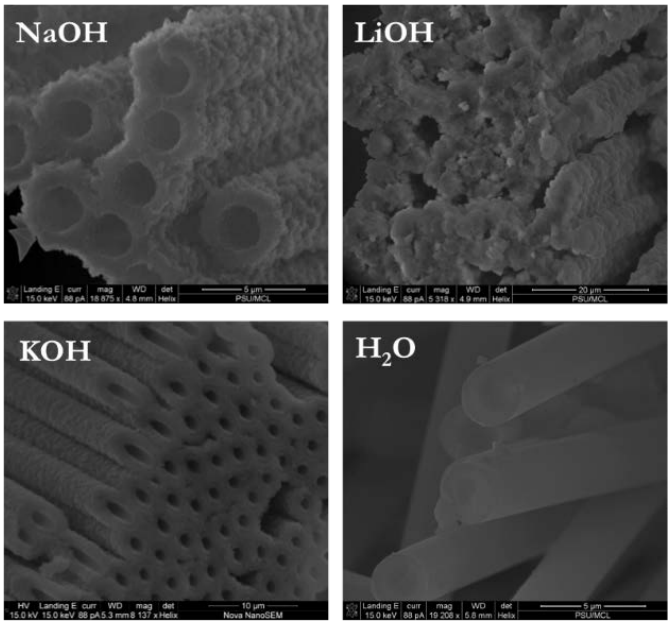

Figure 2.1: Scanning electron micrographs of the ISG fibers corroded in 1.0 M solutions and water for 400 hrs

The evolution of hollow-tube formation and crystallization at high pH was investigated with a second set of samples in 1.0 M solutions of NaOH and KOH. Fibers were reacted in the solutions, and specimens of fiber were removed at periodic intervals, rinsed, dried, and observed via FESEM and XRD. Figure 2.2 is a collage of FE-SEM images for the 1.0 M NaOH samples. The initial observations of mostly symmetrical crystalline-layer formations led to the hypothesis that the crystallized layers were not (gravitationally) precipitating onto the fiber surfaces, but rather were nucleating on the surfaces or within the initial altered layer, and growing by consuming leached material from solution. It seems that the precipitated crystalline phases are locally templated by the original fiber surface as the fiber dissolves radially. This creates a partially crystalline shell whose outside diameter exceeds the original fiber OD. However, other mechanisms may be possible including complete leaching of the soluble boron and sodium, followed by recrystallization of a swollen silica gel altered layer. The highly aggressive nature of the 1.0M hydroxide solutions is a key factor in these initial observations which are being repeated at lower pH (see below). It is also interesting to note that the diameter of the H_2O corroded fibers also increased. The original fiber diameter was 2.50 ± 0.07 µm, and the swelled fiber diameter is 2.85 ± 0.13 µm implying that the amount of swelling in the water sample is 0.35 ± 0.20 µm. This swelled diameter is similar to the diameter of the secondary layer visible in the KOH samples.

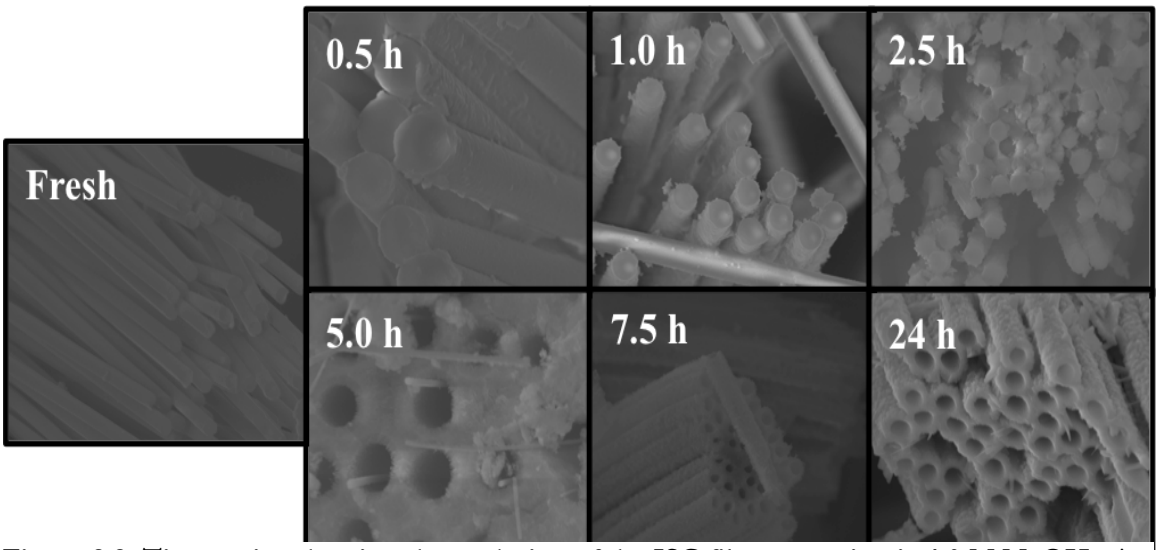

Figure 2.2: Time series showing the evolution of the ISG fiber corrosion in 1.0 M NaOH. At 5.0 h, very small diameter fibers remain inside the hollow shell formations. At 7.5h, all of the original fiber has completely dissolved and only the hollow shell formations remain; however, continued development of crystalline phases is observed by XRD. This suggests that the initial shells are largely amorphous gels, or poorly crystallized metastable phases, which continue to evolve.

XRD was used to characterize any crystalline phases formed during the fiber corrosion reaction and its transition into a tube. These transitions varied with the solution conditions, but otherwise, a process consisting of a dissolving core and crystallizing "shell" was observed for all the samples. X-ray diffraction measurements of these samples showed the appearance of a crystalline phase between 2.5h and 5.0h, as shown in Figure 2.3. The continued development of crystalline phases seems to persist even after complete consumption of the fibers. The experiments conducted in the 1.0 M KOH solutions were similar, although the formation of the crystalline shells occurred more slowly in those samples.

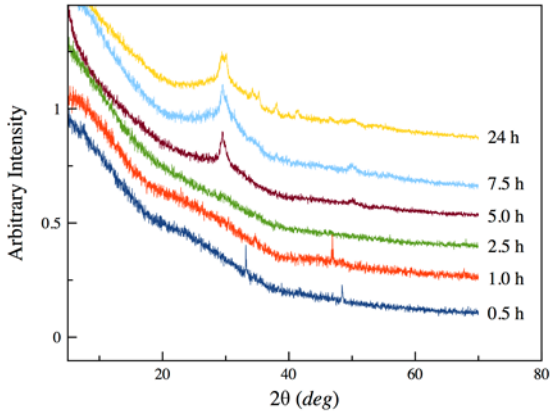

Figure 2.3: Diffraction patterns of the crystalline phase formations on the ISG fibers in 1.0 M NaOH for the various sampling times. (The small peaks in the 0.5 and 1.0 h samples are likely background from the sample holder as a result of not having sufficient sample present during the analysis.)

Fibers were reacted in the high pH 1.0 M hydroxide solutions for hundreds of hours and additional XRD analyses were performed to examine the long-term effects of corrosion in these highly aggressive conditions. The results of these measurements are shown in Figure 2.4. While the crystalline peaks are slightly more developed in the longer term samples, especially the LiOH specimen, a large amorphous background is still observed in the data suggesting the presence of uncorroded glass or a gel like condensate in the samples. The likely phases responsible for the peaks observed in the spectra are also listed in Figure 2.4. It is interesting to note that the LiOH sample, which did not readily form the tubule structures observed in the KOH and NaOH samples, yielded the strongest diffraction signal of all these corroded specimens. This is perhaps a further indication that the tube structures are actually an amorphous, restructured gel template upon which secondary crystalline phases are forming. This hypothesis will be examined via ion beam milling of fiber cross sections and high resolution TEM of the cross sectioned fibers in the near future.

Figure 2.4: X-ray diffraction patterns from ISG fibers corroded in the various 1.0 M hydroxide solutions for extended periods of time along with a control sample corroded in water.

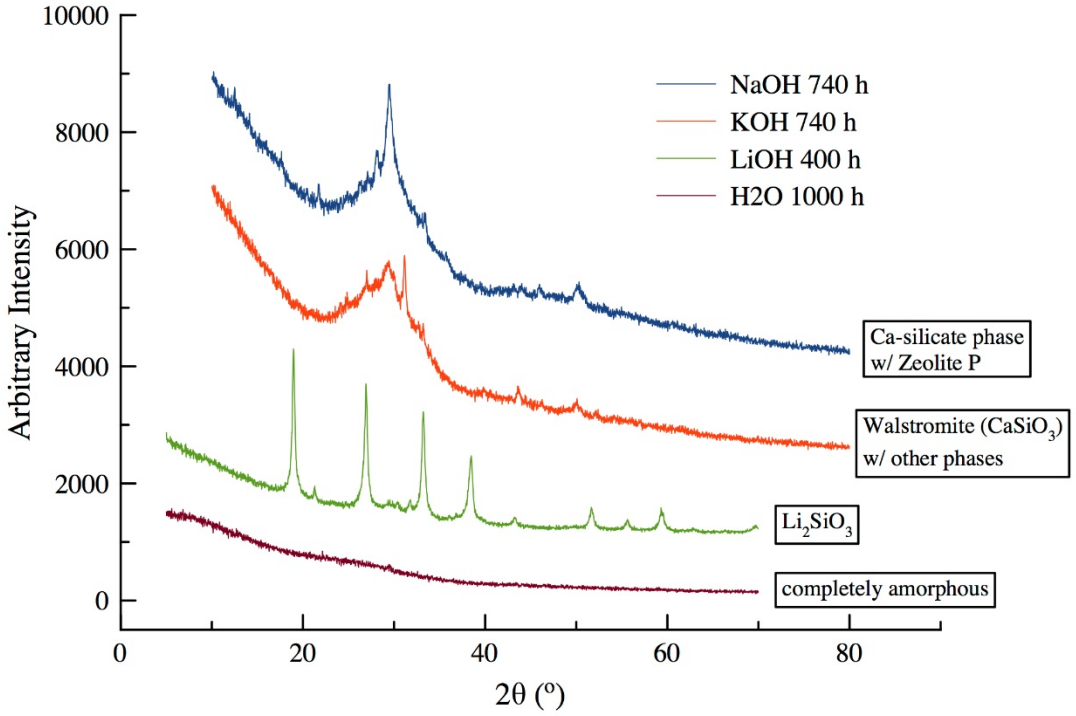

Ca could play a significant role in the Stage II → III transition because of its alkalinity and affinity for silica and alumina. To investigate the effects of Ca with respect to the types of phases that form under alkaline conditions, solutions of $Ca(OH)_2$ were prepared at the solubility limit for calcium hydroxide. This yielded ~pH 12.5 solutions which were subsequently 'spiked' with either 100 mL of 1.0M NaOH or KOH to produce final solutions of pH 13.0 and 13.4, respectively. The spiked solutions were cloudy and were subsequently filtered through 0.2 µm-pore syringe filters to remove any suspended particulates. The resulting solutions were water-clear and aliquots of the solutions were saved for compositional analysis with ICP-AES. The results of these measurements showed that the concentration of Ca in the KOH spiked solution was on the order of a few ppm while the NaOH spiked solution had a Ca concentration of

approximately 40 ppm suggesting that the addition of the 1.0 M KOH to the initial calcium hydroxide solution caused a precipitation reaction to occur and remove Ca from the solution.

These two experiments, $Ca(OH)_2$/NaOH and $Ca(OH)_2$/KOH, were conducted for longer times relative to the initial high pH experiments and not sampled as frequently as the earlier hydroxide experiments. Fiber specimens were collected after approximately 1900 hours of corrosion time, and examined by XRD – the resulting spectra are shown in Figure 2.5.

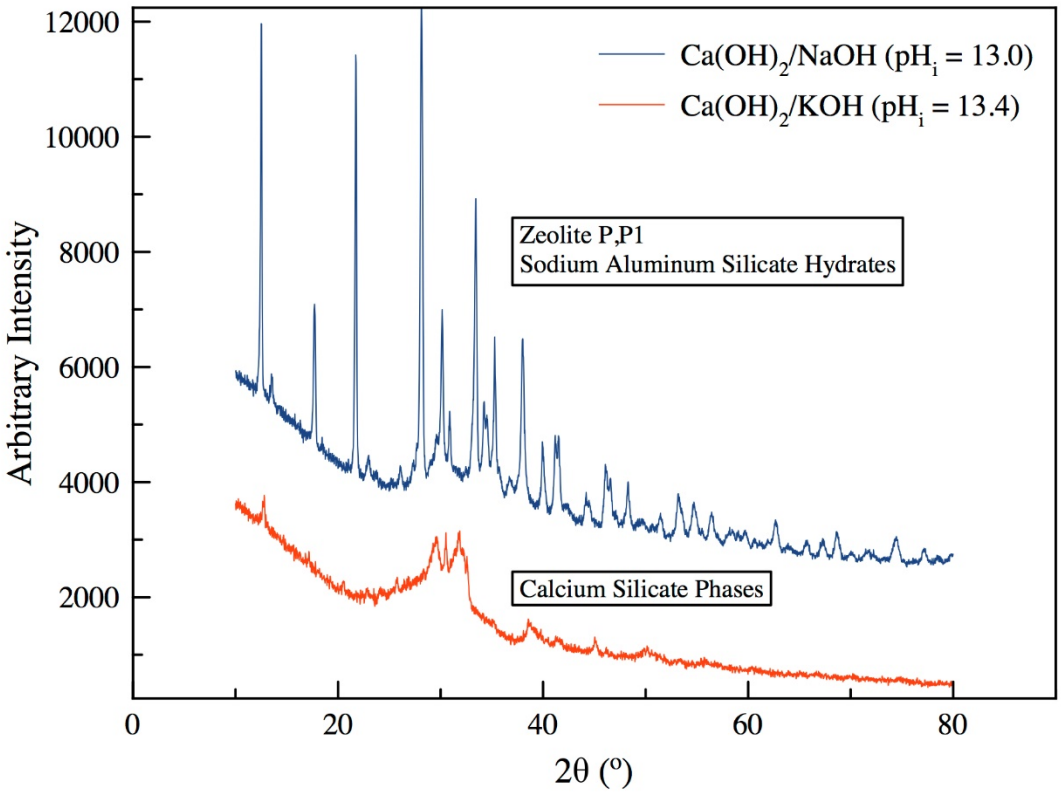

Figure 2.5: X-ray diffraction data for the ISG fibers corroded in pH 13.4 $Ca(OH)_2$/KOH and pH 13.0 $Ca(OH)_2$/NaOH for approximately 1900 hours. The NaOH spiked sample showed a high amount of crystallization with the formation of zeolites from the sodium aluminum silicate hydrate family (zeolite P, P1, and others). The KOH sample seemed to form phases that appear to be calcium silicate-based.

Overall, the results of these high pH experiments confirm that the amount of crystallization and the formation of specific crystalline phases are strongly dependent on the composition of the concentrated solutions in contact with the glass. We have identified several different phases that form under similar pH conditions but with different precursor concentrations. Of particular note is the formation of the Ca silicate phases in the $Ca(OH)_2$/KOH experiment as compared to the formation of the zeolitic phases in the $Ca(OH)_2$/NaOH experiments. These high pH experiments have provided some insight to the reaction and crystallization of the ISG fibers, and are now being followed-up with lower pH, longer-term reactions.

Finally, comparable fiber corrosion experiments using $Ca(OH)_2$ solutions at 90ºC are also underway. The motivation for using these solutions was the early observation of Ca consumption from solution and calcium silicate crystallization in the 1.0 M KOH and NaOH experiments. It is well-known in the glass corrosion and cement chemistry fields that Ca plays a role in the formation of crystalline silicates. The goal here is to watch the evolution of the fiber and solution when it is already saturated with Ca. To that end, we prepared a solution of $Ca(OH)_2$ at the solubility limit of the hydroxide in a neutral water solvent, which yields a pH of ~12.5 solution. The ISG fibers are periodically sampled and examined with FE-SEM; micrographs of the corroded fibers sampled at 168 hours, 697 hours and 868 hours are shown in Figure 2.6.

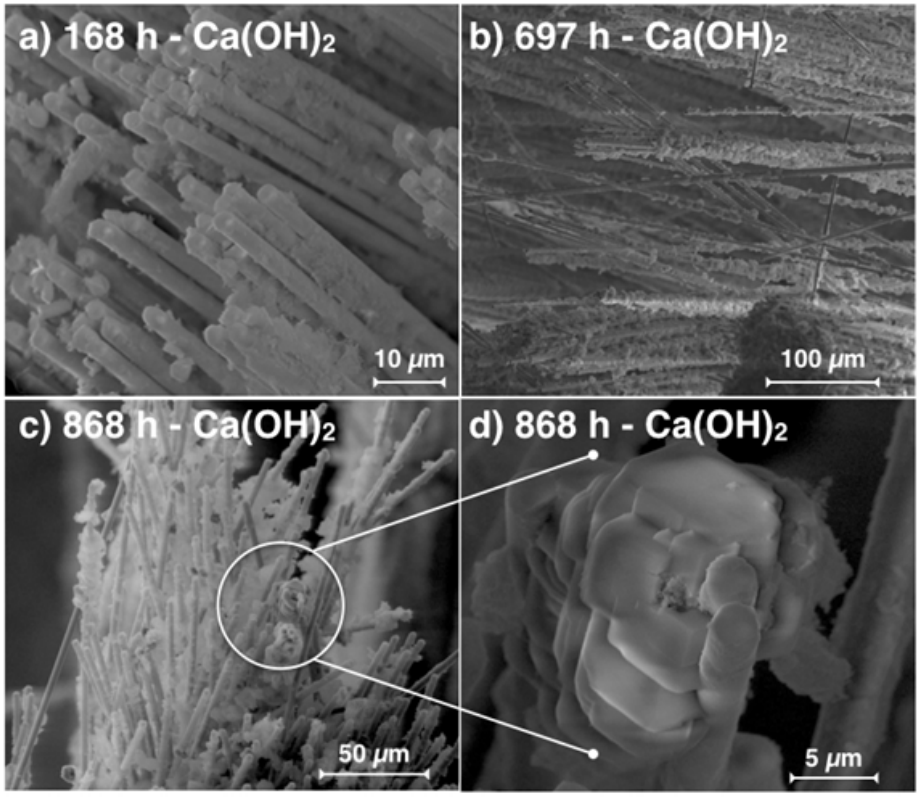

Figure 2.6: FE-SEM images of ISG fibers corroded in 0.02 M $Ca(OH)_2$ solution for varying lengths of time. Even at long times, the formation of the crystalline shell structures was not observed for these samples; rather, precipitation of a crystalline phase.

The corrosion of ISG fibers in saturated Ca-hydroxide at pH 12.5 has created a unique situation compared to the alkali-hydroxide solutions. Even after a relatively long period of time compared to the 1.0M NaOH and KOH experiments, these fibers do not show evidence of dissolution or re-crystallization. Rather, crystalline material has deposited on the fibers and fiber bundles as seen in Figure 2.6. XRD analysis suggests a Ca-carbonate like phase, but the sample and its XRD pattern, are still evolving.

SECTION 2. MINERAL PRECIPITATION IN CONCENTRATED AQUEOUS SOLUTIONS OF NA AND LI SILICATE GLASS

CORY L TRIVELPIECE [a], WILLIAM D BURGOS [b] AND CARLO G PANTANO [a,c]

[a] MATERIALS RESEARCH INSTITUTE
[b] DEPARTMENT OF CIVIL AND ENVIRONMENTAL ENGINEERING
[c] DEPARTMENT OF MATERIALS SCIENCE AND ENGINEERING

THE PENNSYLVANIA STATE UNIVERSITY
UNIVERSITY PARK, PA 16801

ABSTRACT

The dissolution of glass in aqueous solution is thermodynamically driven by the non-equilibrium state of the glass itself. Under conditions of high alkalinity, the solution of glass can be highly concentrated, and near-equilibrium with respect to crystalline mineral phases. For durable glasses, the transformation of a glass into its equilibrium crystalline phases is usually kinetically limited by nucleation effects, surface alteration layers on the glass, and concentration of the solution. But in some cases, the precipitation of secondary phases can occur to drive the continued dissolution of the glass. In this study, the transformation of two simple and soluble alkali silicate glasses, Li-disilicate and Na-disilicate (LDS and NDS), was followed with solution analysis, x-ray diffraction and thermodynamic modeling using Geochemist's Work Bench (GWB). The evolution of the concentrated glass solution, as opposed to the kinetics of dissolution, was the primary focus. It is shown that the LDS system undergoes significant super-saturation followed by precipitation of hydrated Li-disilicate crystals; this was in reasonable agreement with the GWB modeling, although the GWB outputs found the solution saturated with respect to other crystalline phases which were not observed. For the NDS system, precipitation was much less prevalent even though more than 75% of the glass was in solution. In contrast to the LDS system, the NDS system did not precipitate any of the simple binary Na-silicates, but rather formed a gel which persisted for up to 5000 hrs. The saturation indices for zeolitic phases were exceedingly high, and with the trace amounts of Al in these solutions, the crystallization of zeolite Na-P1 was observed by x-ray diffraction after 1000 hrs. These observations are relevant to the long-term stability of complex, multicomponent nuclear waste glasses.

1.0 INTRODUCTION

A series of simple dissolution/precipitation experiments involving binary glass compositions was undertaken in order to characterize the evolution of concentrated glass solutions (CGS) and the conditions under which secondary mineral phases will precipitate out of these solutions. We define a concentrated glass solution to be an aqueous solution containing elemental and hydroxylated cations and their complexes which form under highly alkaline conditions where silicates are soluble. The high alkalinity can be created by the dissolution of the glass itself or the addition of a hydroxide. Of particular interest in this study is the composition and speciation of the solution at the time of the precipitation, which usually occurs under near equilibrium conditions with respect to one or more saturated species.

This study is relevant to the long-term corrosion behavior of nuclear waste as illustrated in Figure 1 below. In general, such glasses show an initial period (Stage I) of high rate dissolution during which the contacting solution becomes saturated with one or more soluble glass species (notably silicic acid) and an altered layer forms on the glass. [1,2,3] This leads to a decrease in the dissolution rate due to reduced thermodynamic driving force and kinetic limitations associated with the transport of water and reaction products through the altered surface layer. During Stage II of the corrosion process, the glass exhibits a low residual dissolution rate, which is a source term for modeling the long term dissolution behavior of the waste-form package. But it has been observed in some systems that the dissolution rate may increase due to resumption of glass alteration; this resumption of alteration defines the Stage II to Stage III transition (see Figure 1). It has been proposed by many that this is caused by a sudden drop in solution concentration of one or more saturated species due to the precipitation/crystallization of secondary mineral phases that consume those species. This increases the thermodynamic driving force for high-rate dissolution of the glass, in some cases nearly as high as the initial forward rate. One goal of this work is to evaluate this concept using simple glass systems with careful attention to the solution chemistry at the onset of precipitation.

In the work reported here, two different simple binary glasses (Li-disilicate and Na-disilicate, LDS and NDS) were studied because they are highly susceptible to dissolution in water. But LDS is known to promote extensive crystallization during dissolution while NDS does not. Considering the reactivity of these two alkali-silicate species in more complex glasses, and the need to build a database for thermodynamic modeling of more complex glasses, another goal of this study was to use the Geochemist's Workbench (GWB) software package to interpret evolution of the solution and its precipitation behavior. It seems likely that speciation in the concentrated solution, e.g., complexes, oligomers and colloids of alkali-silicates and alkali-aluminosilicates, plays a role in triggering the transition [4,5,6]. If so, the concentrated glass solutions can be used in future studies to characterize those species by nuclear magnetic resonance (NMR) or infrared spectroscopy (FTIR).

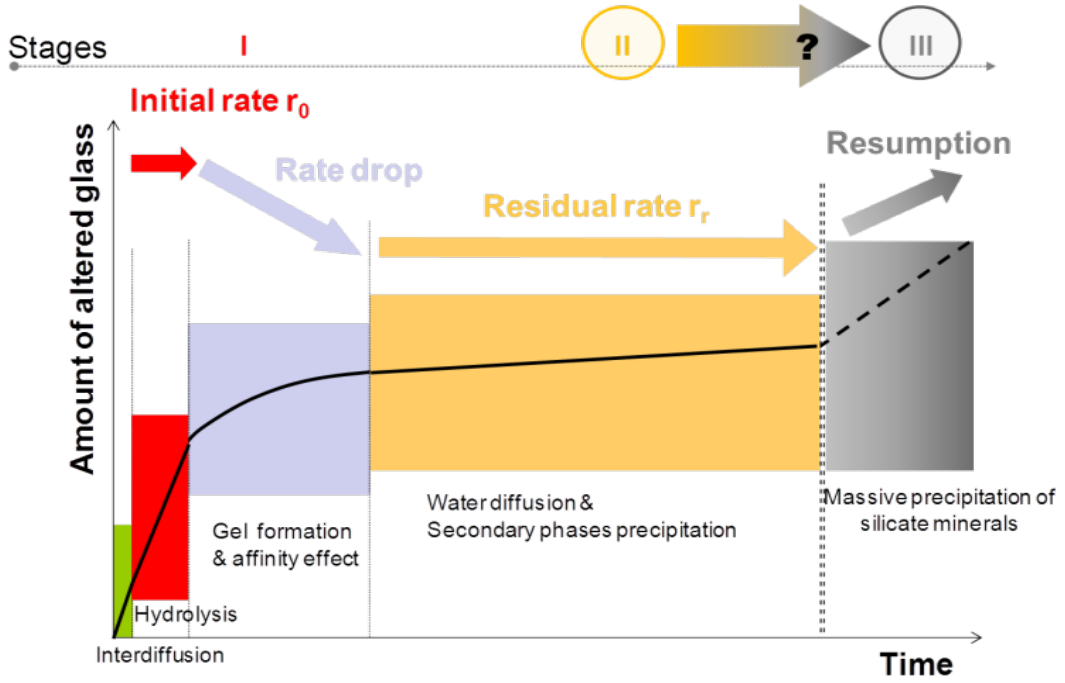

Figure 1: The transition from Stage II > Stage III dissolution is believed to be caused by precipitation of crystals from the contacting solution that lowers the concentration of solution species which are saturated with respect to one or more metastable or equilibrium crystalline phases (notably silica) such that further dissolution of the altered layer or bulk glass may resume under a thermodynamic driving force. [2]

2. METHODS

This work was performed in two stages: (1) dissolution/precipitation experiments were conducted to determine the mass quantity of glass in solution at the onset of precipitation, the evolution of Na, Li and Si solution concentrations during the precipitation, and the identity of the detectable secondary precipitates by x-ray diffraction or electron microscopy; and, (2) the experimental concentration data was input to the modeling software, Geochemist's Workbench, to evaluate it relative to the solubility limits of the detected or expected mineral precipitates.

2.1 Experimental Methods

Approximately 175 grams of lithium disilicate (LDS) and sodium disilicate (NDS) glasses were fabricated from the starting materials Li_2CO_3/SiO_2 and Na_2CO_3/SiO_2, respectively, and mixed in 300 g batches. Each composition was melted at 1275ºC for approximately one hour and then cast onto a stainless steel plate. The resulting glass slab was subsequently crushed and re-melted at the same temperature and time to ensure a homogenous melt. The second melt was poured onto a stainless steel slab containing machined square mold features. These features allow monolithic specimens to be cleaved from the main slab for other experiments without cutting or contamination. This slab was annealed at 500ºC for two hours and then cooled to 300ºC at a rate of 0.5ºC/min followed by cooling to room temperature at a rate not exceeding 2ºC/min. The

annealed glass was crushed using a Retsch ® Vibratory Disc Mill RS 200 into a powder form with a large particle size distribution ranging from hundreds of nanometers to millimeters. The powder was not sieved to a more precise size range, nor was the specific surface area of the powders measured, because these experiments were not concerned with the kinetics of dissolution rates but rather the solution chemistry at the time of secondary phase precipitation.

The glass powders were reacted with ASTM Type I water in 500 mL PFA jars from Savillex® in a VWR Symphony® oven at an oven temperature of 90ºC. Some preliminary experiments were performed to determine the mass of glass powder needed to reach a saturated condition in the two disilicate compositions (LDS and NDS) while still retaining some undissolved glass in the reaction vessels. The mass of glass was controlled and varied in these experiments to provide a measure of the fraction of glass dissolved when secondary precipitation is observed. Table 1 is the experimental matrix of the various mass to volume

Table 1: Matrix of conditions showing the masses of glass and volumes of solution used for each experiment, and their corresponding hypothetical concentrations assuming complete dissolution of the glass. The 150 g/L NDS and LDS experiments marked by a * were "spiked" with $Al(OH)_3$ to test the inclusion of Al in the solution. The measured maximum and average pH values of the collected solution aliquots are also included here. The table entries in gray were not modeled in GWB.

Glass	Initial Glass Mass (g)	Solution Volume (mL)	Hypothetical Concentrations for 100% CGS				Max. pH	Average pH
			Glass Total (g/L)	Li (µg/mL)	Na (µg/mL)	Si (µg/mL)		
LDS	2.5	500	5	465	x	1875	11.93	11.53
LDS	3.5	500	7	651	x	2625	11.96	11.69
LDS	5.0	500	10	930	x	3750	11.8	11.54
LDS	5.5	500	11	1023	x	4125	11.89	11.68
LDS	7.5	500	15	1395	x	5625	11.97	11.57
LDS	12.5	500	25	2325	x	9375	11.98	11.54
LDS	15	500	30	2790	x	11250	11.85	11.52
LDS	75	500	150	13950	x	56250	12.18	12.06
LDS*	150	1000	150*	13950	x	56250	12.25	12.13
NDS	75	500	150	x	37800	46200	12.68	12.28
NDS*	150	1000	150*	x	37800	46200	12.77	12.47
NDS	125	250	500	x	126000	154000	12.69	12.45

ratios used for each experiment, also presented as the hypothetical concentrations of a CGS where all of the glass is in solution, along with the measured pH over the course of the experiment. Table 1 includes some conditions for LDS that were not modeled, but are included in the data plots to show overall consistency. In one experiment conducted with the two glasses, the solution was "spiked" with $Al(OH)_3$ to yield an Al concentration of 100 µg/mL in the starting solution, while keeping the glass solution concentration at 150 g/L.

Approximately 20 mL aliquots of each solution were collected at regular intervals to measure pH and concentrations of dissolved elements. pH was measured using a Thermo Electron Corporation

Orion 3 Star electrode and dissolved elements were measured by inductively coupled plasma – atomic emission spectroscopy (ICP-AES, Perkin Elmer Optima 5300). In order to maintain a constant volume of solution in the reaction vessel, an amount of ASTM Type I water, equivalent to the volume of the aliquot extracted, was added back into the reaction vessels after each solution sample collected. Samples of the undissolved glass and any secondary precipitates were also periodically collected for examination with field emission scanning electron microscopy (FE-SEM, FEI NanoSEM 630) and X-ray diffraction (XRD, Panalytical XPert PRO MPD).

At the termination of these experiments, the solutions were decanted from the remaining material and refrigerated for additional measurements and experiments. The undissolved glass and secondary precipitates were oven-dried in the reaction vessels and then removed for further analysis using XRD and FE-SEM.

2.2 Thermodynamic Modeling

The Geochemist's Workbench® [7,8] software program (Aqueous Solutions LLC, Champaign, IL) was used to model the equilibrium solubility of a suite of minerals which could be expected to precipitate during and after the initial rapid dissolution of the LDS and NDS samples. Calculations were performed using the measured values of pH and dissolved elemental concentrations (Al, Li, Na, and Si) at 90ºC and the LLNL thermodynamic dataset [9] (referred to as thermo.com.V8.R6+ within GWB). In these calculations, all mineral phases were suppressed except amorphous silica (SiO_2), analcime ($NaAlSi_2O_6{:}H_2O$), gibbsite ($Al(OH)_3$), di-lithium silicate (Li_2SiO_3), lithium silicate ($Li_2Si_2O_5$), di-sodium silicate (Na_2SiO_3), natrosilite ($Na_2Si_2O_5$), petalite ($LiAlSi_4O_{10}$), spodumene ($LiAlSi_2O_6$), and synthetic zeolite Na-P1 ($Na_6Al_6Si_{10}O_{32}{:}12H_2O$). Mineral dissolution reactions are presented in Table 2. These minerals were included because they have been identified as important glass corrosion products [4,10] and/or were identified in the current experiments by XRD.

Equilibrium constants for the various mineral dissolution reactions (referred to as log K values and reported at specific temperatures used in GWB) were calculated using the best available thermodynamic measurements or estimation techniques. The log K matrices for all minerals modeled in the current study are included in Table 3. Log K values at 25ºC were calculated from the Gibbs free energy of reaction at standard state (ΔG^0_r) for the overall dissolution reaction. ΔG^0_r values depend on the Gibbs free energy of formation at standard state (ΔG^0_f) of the mineral and, of course, all other products and reactants. ΔG^0_f values for all soluble products and reactants were obtained from the LLNL thermodynamic dataset [9]. ΔG^0_f and ΔH^0_f values for all minerals were obtained from the same thermodynamic dataset, measured values reported in the literature, proposed values used in another study, or via an estimation technique. Measured values for ΔG^0_f and ΔH^0_f for Li_2SiO_3 and $Li_2Si_2O_5$ were obtained from the US Bureau of Mines [11]. A measured value for ΔG^0_f for analcime was obtained from Wilkins and Barnes [12]. An estimated value for ΔH^0_f for analcime was obtained following a technique developed by Chermak and Rimstidt [13]. Estimated values for ΔG^0_f and ΔH^0_f for synthetic zeolite Na-P1 were obtained following a

technique developed by Chermak and Rimstidt [13]. Log K values were adjusted to 0, 60 and 100°C using the van't Hoff equation. For higher temperatures included in the log K matrices, all other values for all minerals were set to 500, an entry equivalent to an unknown value in GWB. The results of these calculations are presented as the ratio of Q/K where Q is the ion activity product based on the experimental data.

Table 2: Mineral dissolution reactions considered in the thermodynamic modeling.

Phase	Balanced reaction
Amorphous silica, SiO_2	$SiO_2(am) \rightarrow SiO_2(aq)$
Analcime, $NaAlSi_2O_6{:}H_2O$	$NaAlSi_2O_6{:}H_2O(s) + 4H^+ \rightarrow Na^+ + Al^{+++} + 2SiO_2(aq) + 3H_2O$
Gibbsite, $Al(OH)_3$	$Al(OH)_3(s) + 3H^+ \rightarrow Al^{+++} + 3H_2O$
Di-lithium silicate, Li_2SiO_3	$Li_2SiO_3(s) + 2H^+ \rightarrow 2Li^+ + SiO_2(aq) + H_2O$
Lithium silicate, $Li_2Si_2O_5$	$Li_2Si_2O_5(s) + 2H^+ \rightarrow 2Li^+ + 2SiO_2(aq) + H_2O$
Di-sodium silicate, Na_2SiO_3	$Na_2SiO_3(s) + 2H^+ \dashrightarrow 2Na^+ + SiO_2(aq) + H_2O$
Natrosilite, $Na_2Si_2O_5$	$Na_2Si_2O_5(s) + 2H^+ \rightarrow 2Na^+ + 2SiO_2(aq) + H_2O$
Petalite, $LiAlSi_4O_{10}$	$LiAlSi_4O_{10}(s) + 4H^+ \rightarrow Li^+ + Al^{+++} + 4SiO_2(aq) + 2H_2O$
Spodumene, $LiAlSi_2O_6$	$LiAlSi_2O_6(s) + 4H^+ \rightarrow Li^+ + Al^{+++} + 2SiO_2(aq) + 2H_2O$
Synthetic zeolite Na-P1, $Na_6Al_6Si_{10}O_{32}{:}12H_2O$	$Na_6Al_6Si_{10}O_{32}{:}12H_2O(s) + 24H^+ \dashrightarrow 6Na^+ + 6Al^{+++} + 10SiO_2(aq) + 24H_2O$

Table 3: The log K values used in this study, as well as those from the LLNL data base [9] and those proposed by Strachan and Neeway [10]. Entries in gray were not used in the current study but are included for comparison.

Phase	0°C	25°C	60°C	100°C	Reference
Amorphous silica, SiO_2	-3.0353	-2.7137	-2.3446	-2.0076	This study
Amorphous silica, SiO_2	-3.1240	-2.7136	-2.4067	-2.1843	Wolery, 1992
Amorphous silica, SiO_2	-3.1240	-3.7140	-3.4070	-3.1840	Strachan and Neeway, 2014
Analcime, $NaAlSi_2O_6{:}H_2O$	8.0201	6.7744	5.3446	4.0389	This study
Analcime, $NaAlSi_2O_6{:}H_2O$	8.6163	7.2800	5.6735	4.2314	GWB 9.0
Analcime, $NaAlSi_2O_6{:}H_2O$	6.3160	5.3160	3.7610	2.1880	Strachan and Neeway. 2014
Gibbsite, $Al(OH)_3$	9.3787	7.7560	5.8286	3.9979	Wolery, 1992
Di-lithium silicate, Li_2SiO_3	13.6884	13.07314	12.3669	11.7219	This study
Lithium silicate, $Li_2Si_2O_5$	18.4993	17.3321	15.9924	14.7691	This study
Di-sodium silicate, Na_2SiO_3	23.4776	22.2418	20.6673	19.2091	Wolery, 1992
Natrosilite, $Na_2Si_2O_5$	18.7698	18.1337	17.0473	15.9487	Wolery, 1992
Petalite, $LiAlSi_4O_{10}$	-4.0216	-3.8153	-4.3777	-5.2193	Wolery, 1992
Spodumene, $LiAlSi_2O_6$	8.2165	6.9972	5.1977	3.3955	Wolery, 1992
Synthetic zeolite Na-P1, $Na_6Al_6Si_{10}O_{32}{:}12H_2O$	41.8304	33.9177	24.8350	16.5412	This study

3. RESULTS AND DISCUSSION

Several dissolution experiments were carried out at various ratios of glass mass (M) to solution volume (V) in order to generate a range of concentrated glass solutions for mineral precipitation and solution modeling. Accordingly, the concentrated solutions were created at various states of under- or over-saturation with respect to the minerals of interest. Since these experiments were intended to create near-equilibrium solutions, and not to obtain dissolution rate data, the glass powder particle size and surface-area-to-volume ratios (i.e., SA/V) were not controlled, although all the experiments used comparable sized glass fragments. The measured element concentrations (by ICP-AES) and calculated mass balanced fractional release values (FR_i^*, see Equation 1 below) were used to determine the onset of precipitation and a steady-state solution concentration. The pH of the solutions was also measured throughout the experiment (Table 1). While the pH values did not vary much over the course of the experiments, a clear maximum value of approximately 12-13 was observed within a few hours of the start of all the experiments, and then it slowly decreased throughout the duration of the experiment. The average pH values for the various LDS systems decreased to roughly the same steady-state value whereas there was a measurable difference in the pH values amongst the NDS systems.

Trace amounts of Al contamination were detected in both the LDS and NDS systems, and although Al was not an intentional constituent of these glasses, its concentration is also reported here due to its potential role in the formation of secondary phases.

The mass balanced fractional release is given by equation 1:

$$FR_i^* = {C_{i,n}V_n}\Big/{f_i\left[m_g^0 - \left[C_{i,n}V_n^* + \sum\left(C_{i,n-1}V_{n-1}^*\right)\right]/f_i\right]} \qquad (1)$$

where FR_i^* is the corrected fractional release, V is the solution volume (mL), C_i is the measured concentration of element *i* (µg/mL) in the n^{th} aliquot (experimental time series), m^0_g is the original mass of glass in the experiment (g), f_i is the mass fraction of element *i* in the composition, and V^* is the aliquot volume. The mass-balanced fractional release is a value that accounts for the amount of the original starting mass that is removed from the system during a given aliquot sampling. In slowly dissolving systems or systems where the concentrations of certain elements are small compared to the total mass of glass in the experiment, this correctional term may not be necessary. However, in systems where a majority of the original glass was dissolved - e.g. glass solutions made with very soluble glasses as in this study - the FR^* value gives the amount of glass dissolved such that a value of unity indicates complete dissolution of a specific element.

3.1 LDS Solution Analysis

Figures 2 and 3 show the evolution of the solution concentrations and fractional masses dissolved for Li and Si in the LDS system. It is clearly evident in the concentration data that the solutions with starting mass-to-volume ratio > 2.5 g/L reached a super-saturated state followed by a rapid decrease in the solution concentration of both the lithium and silicon (Figure 2). In this case of LDS, this decrease in concentration was accompanied by the formation of highly crystalline material on or near what remained of the original glass powder. The nearly equivalent values of the solution concentrations after the precipitation event provides an equilibrium concentration for Li and Si with respect to the precipitated mineral phase (Li-disilicate, see below).

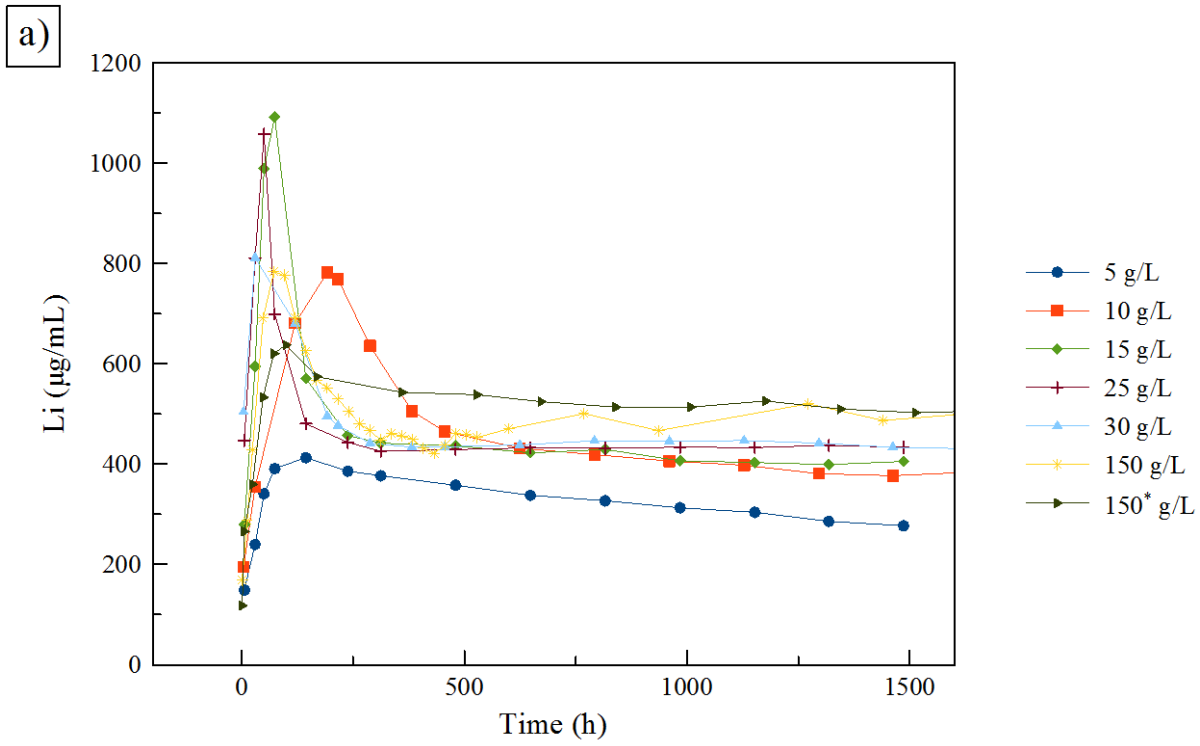

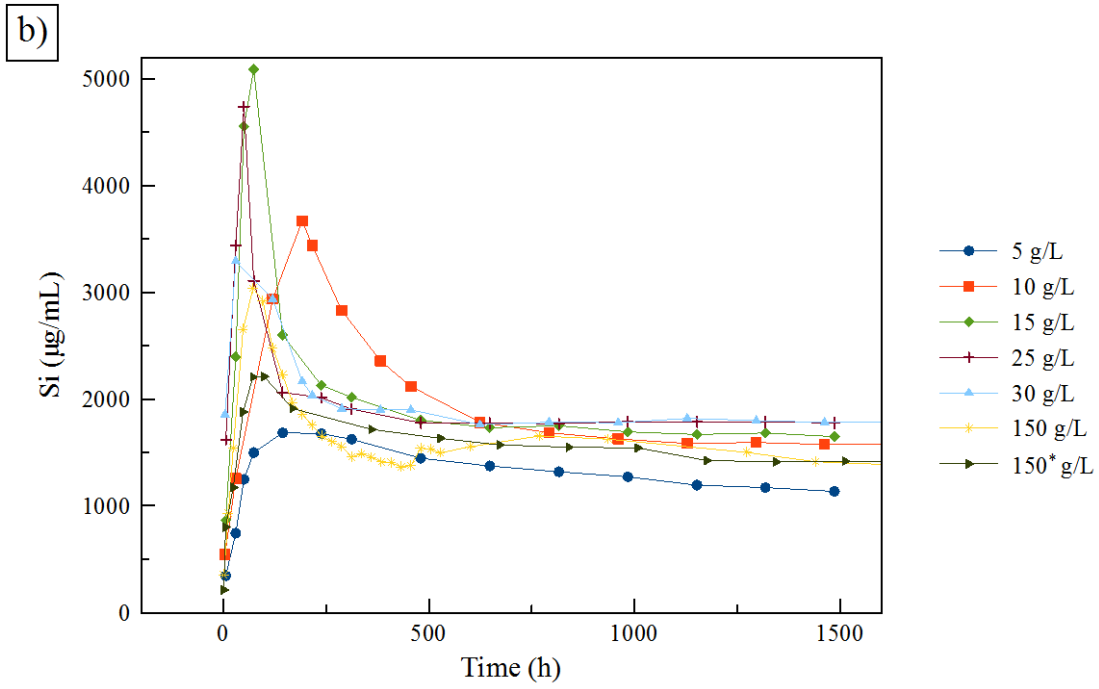

Figure 2a,b: Measured concentration of Li and Si in the LDS experiments. The 5, 15, and 25 g/L solutions, along with their trace Al contamination, were used to model the phase precipitation in the LDS systems.

The fractional release data in Figure 3 indicates that for small M/V (5 g/L), all of the glass dissolves initially (FR^* for Si and Li is equal to 1), and maintains it solubility for the duration of this experiment (1500 hrs.) with no visible evidence of mineral precipitation. For M/V values of 10 g/L and 15 g/L, the mass-balanced fractional release reach a value of unity for Si, and ~0.9 for Li, which indicates that most of the original glass powder has dissolved. But unlike the 5 g/L system, the concentration of dissolved Li and Si species in the 10 and 15 g/L experiments was sufficient to drive the formation of secondary mineral phases, again Li-disilicate. The mass-balanced fractional release for 25 g/L and higher masses systems did not reach FR^* values of 1 before the concentrations of Li and Si dropped due to the precipitation of Li-disilicate. Examination of Figure 2 suggests that concentrations of the order 800 µg/mL for Li and 3500 µg/mL for Si, are required to observe precipitation under these conditions. It is also interesting that the fractional release data for all the experiments indicates the residual amount of dissolved glass in solution to be ~6 grams for all experiments. It remains to be shown whether the remaining mass of glass (for the experiments where a fractional release of unity is not observed before the onset of precipitation) continued to dissolve while the secondary precipitates continued to form under the otherwise pseudo-equilibrium solution conditions. Table 4 presents a summary of the observed Li, Na and Si concentrations observed at the onset of precipitation (c^{max}) and the subsequent pseudo-equilibrium value (c^{avg}) thereafter. These can be compared to the hypothetical concentrated glass solution concentrations in Table 3.

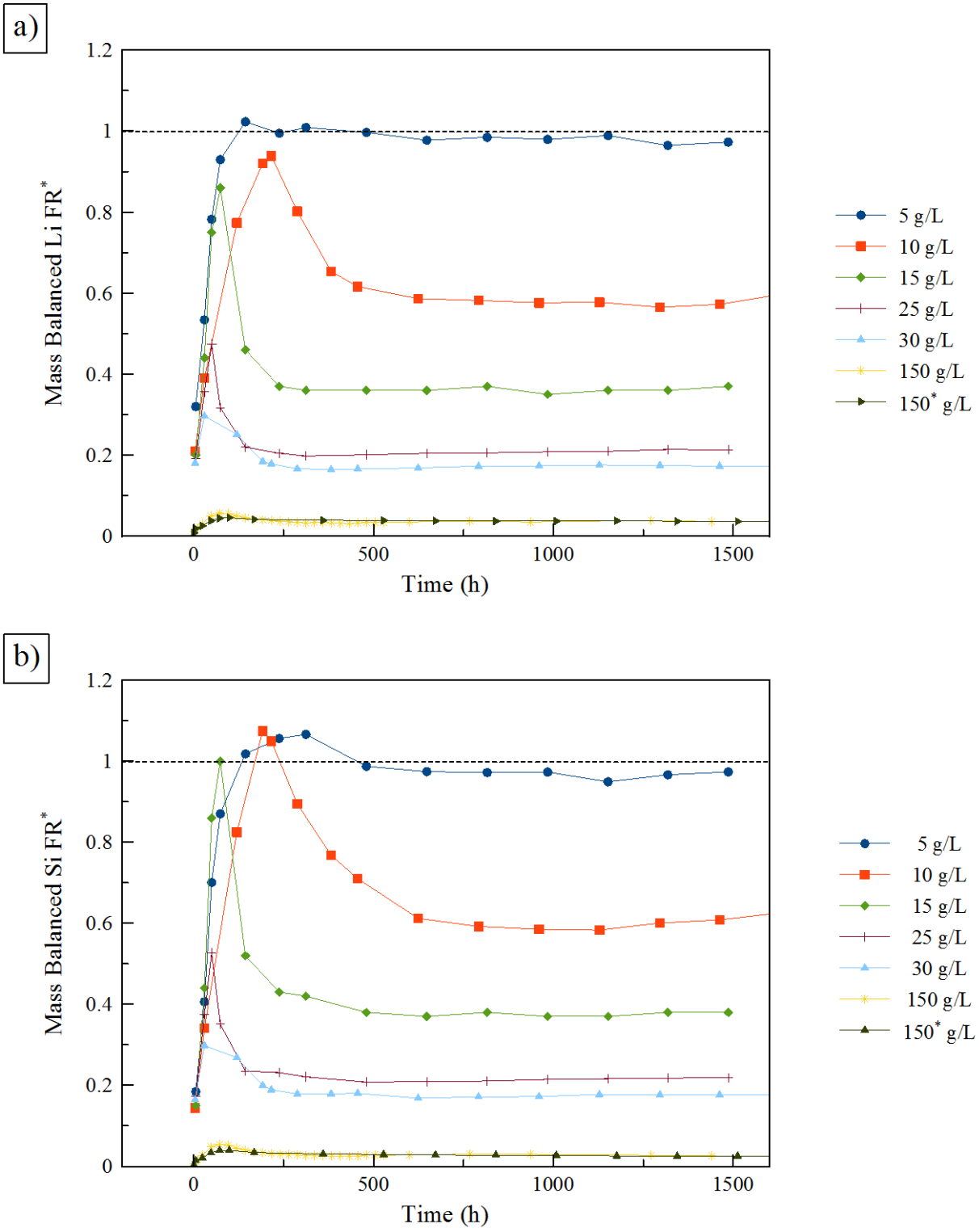

Figure 3a, b: Fractional release of Li and Si in the LDS experiments.

Table 4: The maximum and average values of the experimental concentrations measured via ICP-AES for the modeled systems along with the maximum $log_{10}(Q/K)$ values calculated by GWB for the minerals of interest in the various experiments.

					Maximum $log_{10}(Q/K)$		
Glass	Mass-to-Volume Ratio (g/L)	$C_{Li}^{max}/C_{Li}^{avg}$ (µg/mL)	$C_{Na}^{max}/C_{Na}^{avg}$ (µg/mL)	$C_{Si}^{max}/C_{Si}^{avg}$ (µg/mL)	Analcime	$Li_2Si_2O_5$	Zeolite Na-P1
LDS	5	413/315	x	1686/1274	6.52E-02	1.28E+01	x
LDS	15	1092/420	x	5095/1731	2.12E-02	6.63E+02	x
LDS	25	1058/434	x	4744/1784	1.17E-02	5.30E+02	x
NDS	150	x	23743/10596	31688/14328	8.51E+01	x	2.60E+26
NDS	150*	x	27143/23278	37922/25579	1.05E+02	x	1.13E+27
NDS	500	x	59138/24413	76269/31888	5.72E+02	x	1.61E+31

3.2 NDS Solution Analysis

The evolution of changes in solution chemistry for the NDS system was very different than in the LDS system. In general, the NDS dissolutions occurred much slower than observed in the LDS system, as revealed by the time scales in Figures 4 and 5. It is also evident there is not a well-defined super-saturation, nor steady-state solution concentration value, after precipitation of Na or Si. Correspondingly, the fractional release data for NDS in Figure 5 does not exhibit a defined drop in Na or Si concentration or a steady-state solubility for this glass as was observed in the LDS system. More evident in the fractional release data is the almost complete dissolution of the glass followed by a slow decrease in concentration of Na and Si dissolved species. The most common visual observations for the NDS experiments was creation of a transparent gel over the first few days while the solution concentrations continued to increase, with visible evidence of secondary precipitates observed only after much longer times (>1000 hours).

After a dissolution period of approximately 1000 hours, a secondary precipitate started to appear in the 500 g/L sample in the presence of the gel. A similar material was visually observed in the 150 g/mL and 150* g/L sample at approximately1000 hours; however, it appeared in much less quantity than in the 500 g/L sample. The formation of this precipitate material likely corresponds to the slow and steady decreases observed in the measured concentrations of Na and Si in Figure 4. The amount of precipitate material observed in all of the NDS digestion jars was much less than the amount of starting glass powder, whereas the LDS solutions showed significant quantities of secondary mineral precipitates. The silica solution concentrations in the NDS experiments reached much higher values than in the LDS experiments, and this was consistent with the observation of much less silicate crystal phase precipitation in NDS than LDS (e.g., compare the 150 g/L LDS and NDS samples).

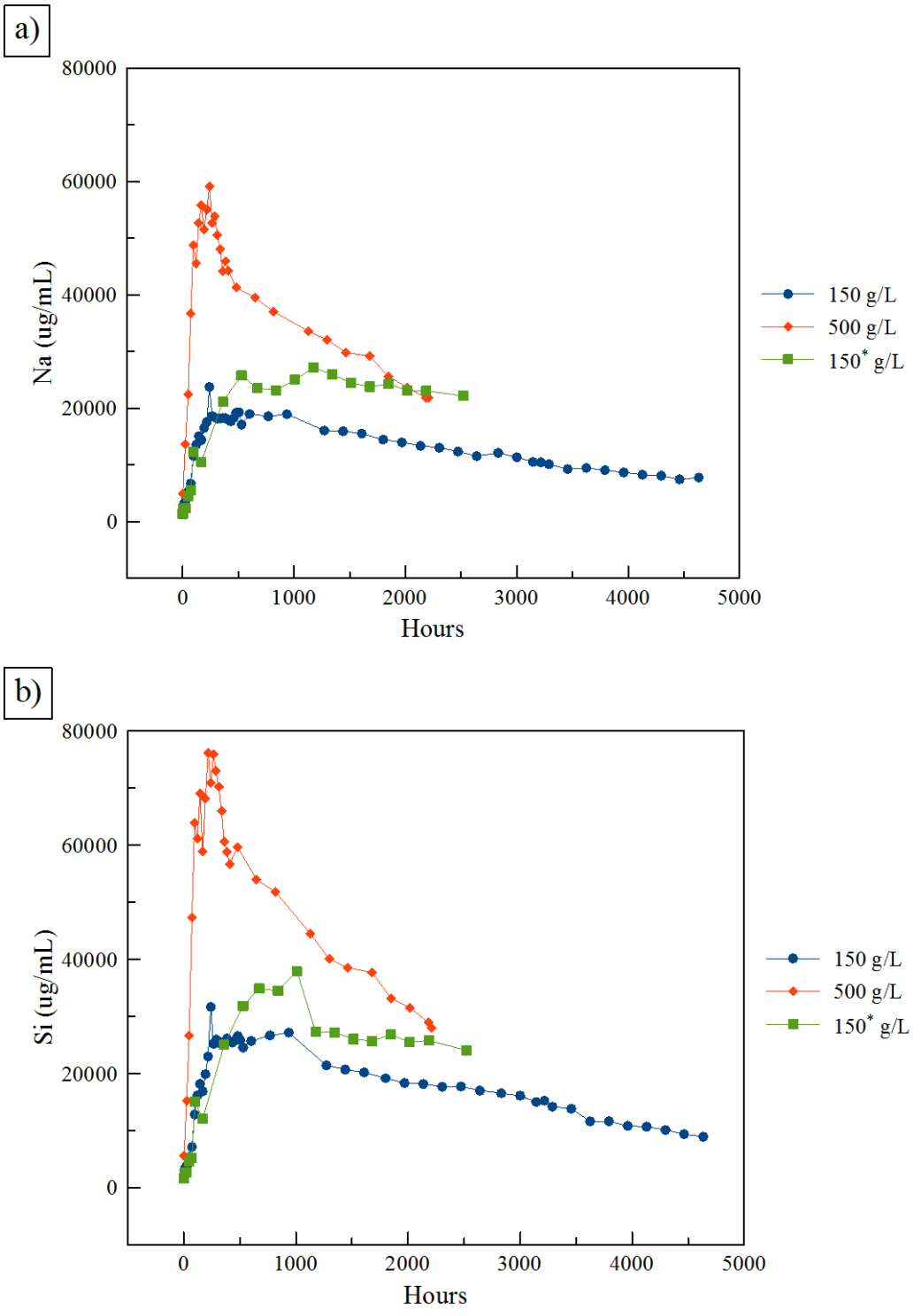

Figure 4a,b: The measured concentration of Na and Si in the NDS experiments. These data, along with the Al contaminant concentration, were used to model the phase precipitation in the NDS systems.

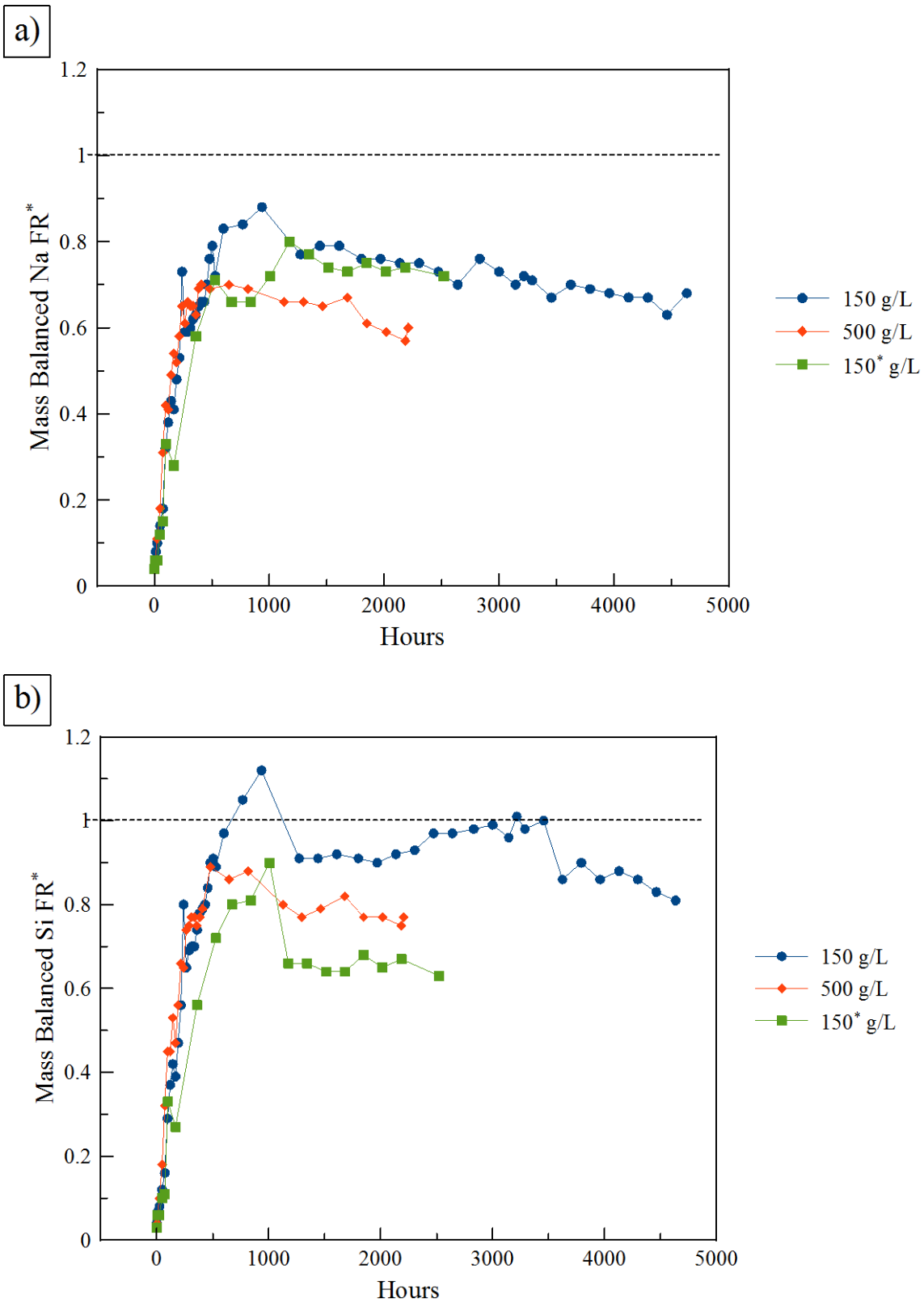

Figure 5a,b: Fractional release values of Na and Si for the modeled NDS systems.

It should also be noted that these laboratory glasses contained detectable amounts of aluminum due to its impurity level in the silica batch material, or in the case of the 150* g/L experiment due to its intentional addition to the solution at 100 µg Al/mL. The data in Figure 6 show that the Al levels reached much higher levels in NDS than in LDS before it was removed from solution. It is especially noteworthy that all of the Al was consumed by the end of these experiments, presumably by the precipitation reaction, or in the case of NDS, by adsorption and reaction with the gel. Unfortunately, the relative amounts of gel and secondary precipitate were impossible to monitor in these experiments.

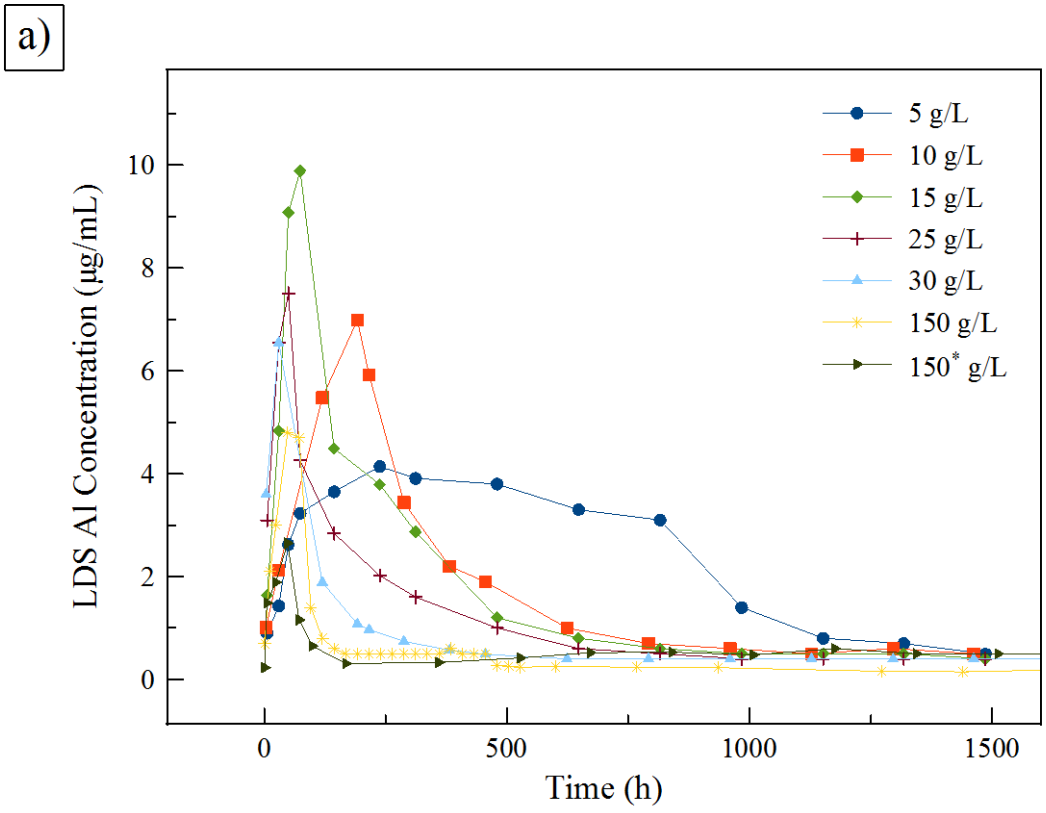

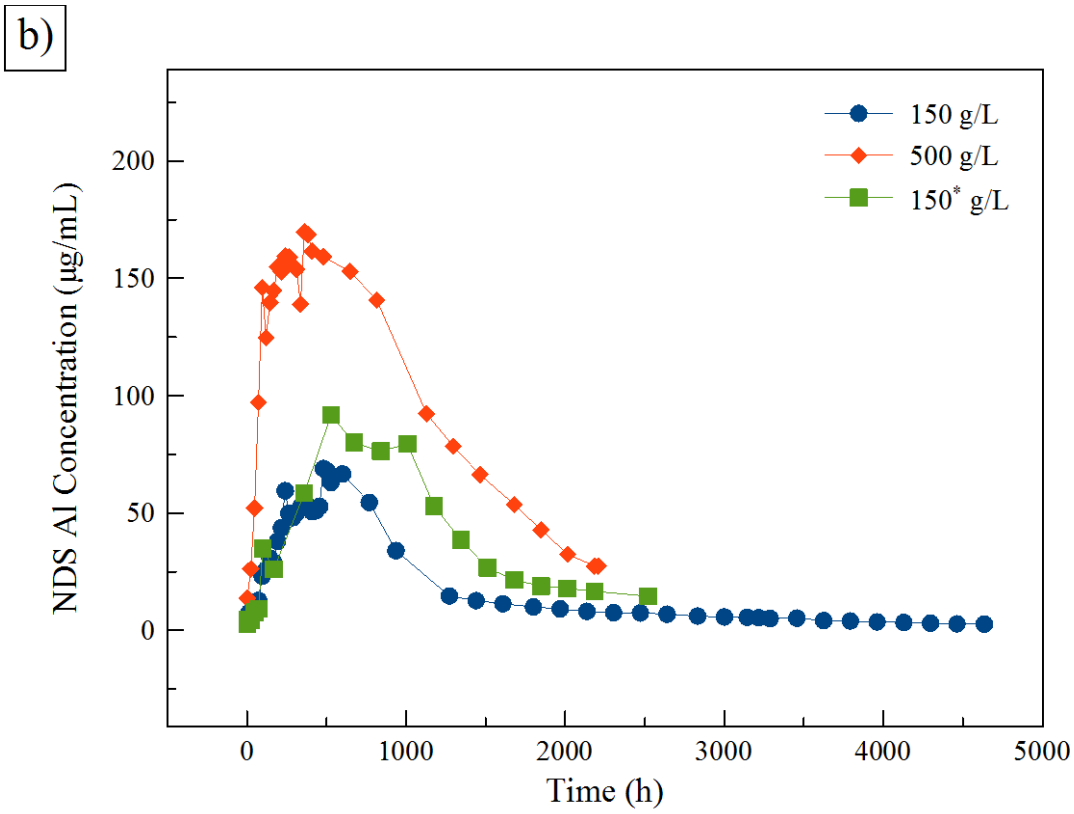

Figure 6a,b: The concentration of the Al contamination measured in the LDS (a) and NDS (b) systems.

3.3 FE-SEM and XRD Analyses of Precipitated Phases

Small amounts of precipitated materials were removed from the digestion vessels during the experiments for further analyses, as well as after the digestion experiments were concluded. The collected samples were typically oven dried for both the FE-SEM and XRD analyses.

The secondary precipitates formed in the LDS experiments were also examined by FE-SEM and XRD. Figure 7a shows electron micrographs of the LDS precipitate that was found to form after the sudden drop in solution concentration of Li and Si. Figure 7b is a diffraction pattern collected from a sample of the LDS secondary precipitate. The primary crystalline phase appearing in this diffraction spectrum was lithium di-silicate hydrate ($Li_2Si_2O_5 \cdot 2H_2O$). A strong peak at approximately $2\theta = 30°$ remains unidentified.

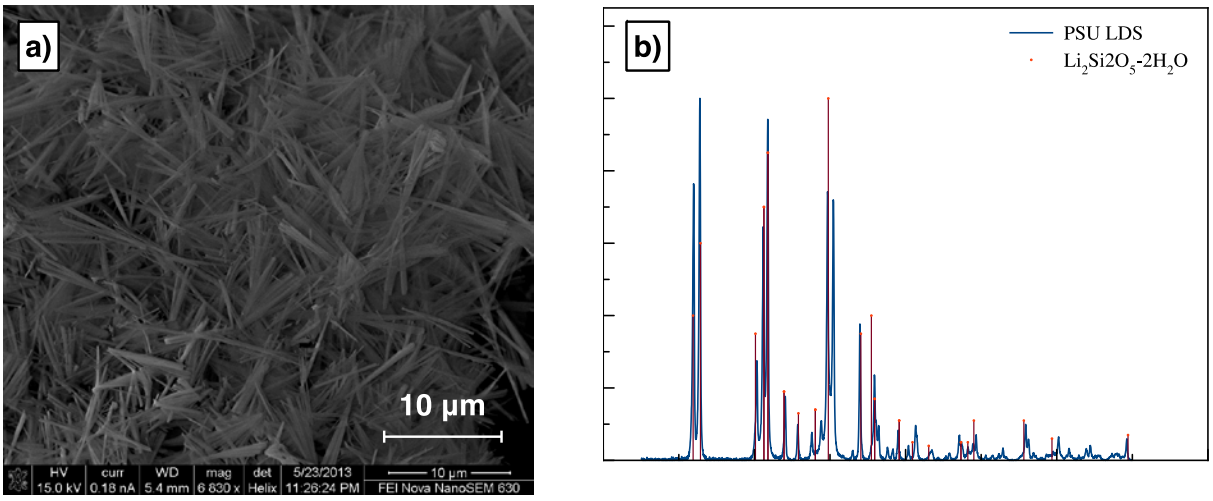

Figure 7a,b: FE-SEM image showing the crystalline precipitate that forms in the LDS systems after the super-saturation event as well as the diffraction pattern identifying that lithium silicate hydrate is the predominate phase that formed in this system.

The FE-SEM images of the solid residuals in the NDS solution, shown in Figure 8a reveal secondary precipitates that appear to be growing on the surface of larger amorphous structures. These amorphous structures are believed to be the transparent gel that formed rapidly during the initial stages of dissolution. Energy-dispersive x-ray analysis in the FESEM revealed that they contain Si and Na, but not Al. X-ray diffraction analysis of this sample (Figure 8b) indicates that synthetic zeolites (sodium aluminum silicate hydrates, Na-P family) are the predominant secondary precipitates that formed, although there are a few as yet unidentified minor-phase peaks at approximate 2θ angles of 6°, 13°, and 32° which do not correspond to any of the minerals expected and modeled in this study. The phase matching was performed using IDDC databases.

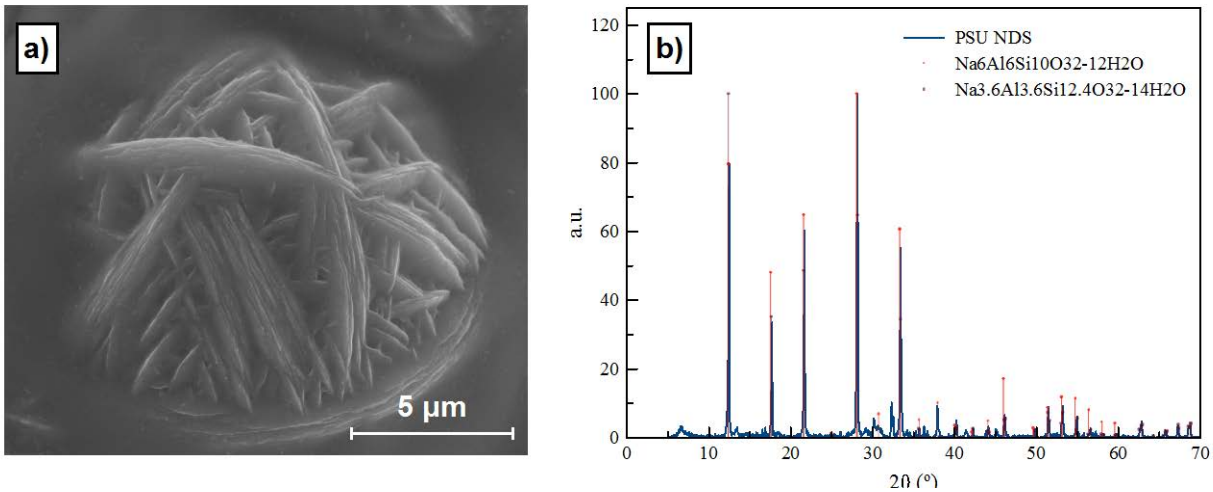

Figure 8a,b: FE-SEM images of the crystalline phase formations observed in the NDS precipitate and the corresponding diffraction pattern identifying the sodium aluminum silicate zeolitic phases.

3.4 Modeling

Geochemist's Workbench 9.0 was used to calculate the saturation indices (Q/K) of selected minerals over the course of the dissolution/precipitation experiments. A mineral with a saturation index greater than one is super-saturated and would be thermodynamically favored to precipitate from solution.

For the LDS experiments (Figure 9), the Q/K values indicate that all the glass solutions became super-saturated with respect to lithium metasilicate**,** lithium disilicate, and petalite. No other mineral phases became relevant, even as the potential concentration of the LDS glass solution increased from 5 g/L to 25 g/L. The XRD patterns (Figure 7b) of the precipitates from these experiments was best matched to lithium disilicate hydrate. Thermodynamic data for hydrated-Li disilicate phase is not available and so it could not be modeled in GWB. However, thermodynamic data was available for Li disilicate and this mineral was included in GWB calculations. The XRD match to the hydrated-Li disilicate phase left one strong peak unidentified in the spectra, and so there is still some uncertainty here based on the lack of equilibrium constants and a more accurate fit for the XRD spectrum. Although the GWB calculations show the 5 g/L solution to be super-saturated with respect to Li disilicate, this solution was found to be precipitate free. In contrast to the other solutions with more glass mass available (Figures 2 and 9), the 5 g/L solution did not produce the peak in saturation index at the beginning of the dissolution. It seems likely that at 5 g/L, there is insufficient driving force for crystal nucleation even though the Q/K value at longer times is comparable to the other glass solutions. This could be a surface-area-to-volume ratio effect that creates an extremely super-saturated condition at the beginning of the dissolution process.

For the NDS experiments (Figure 10), the solutions became extremely super-saturated with respect to synthetic zeolite Na-P1 (e.g., log Q/K > 10^{25}). The solutions were also super-saturated with respect to analcime, but to a much lesser degree (e.g., log Q/K > 10^{2}). The addition of dissolved Al to this system (i.e., 15 g/L vs. 15* g/L) had little effect on the degree of super-saturation of synthetic zeolite Na-P1 or analcime. XRD patterns of the precipitates from these experiments were only well matched by synthetic zeolites of the Na-P family. Therefore, even though analcime could have formed from a thermodynamic perspective, no evidence of this mineral was found under these solution conditions. Interestingly, the Q/K values for the NDS solutions suggest equilibrium with respect to Na_2O-SiO_2. Although there were no Na-silicate crystals detected in the solutions this may reflect the metastable state of the amorphous gel phase observed in all of the NDS solutions, presumably containing adsorbed Na ions as suggested by the steady loss of Na in solution over time.

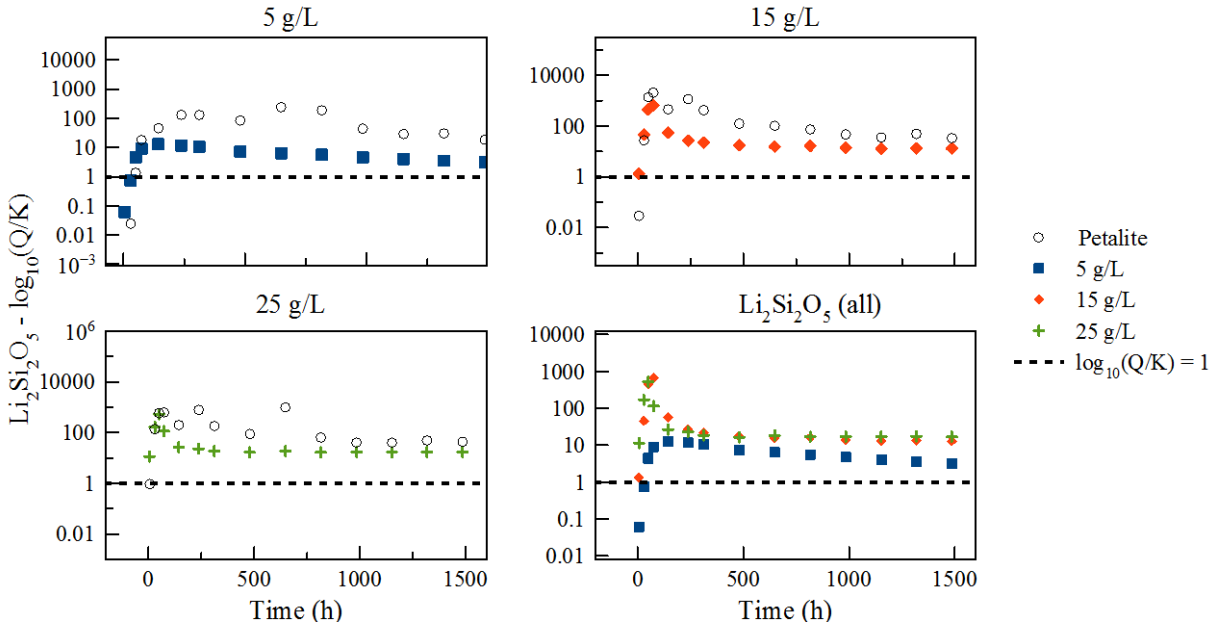

Figure 9: Geochemist's Workbench output for the LDS experiments plotting Q/K for the minerals Li-disilicate and petalite.

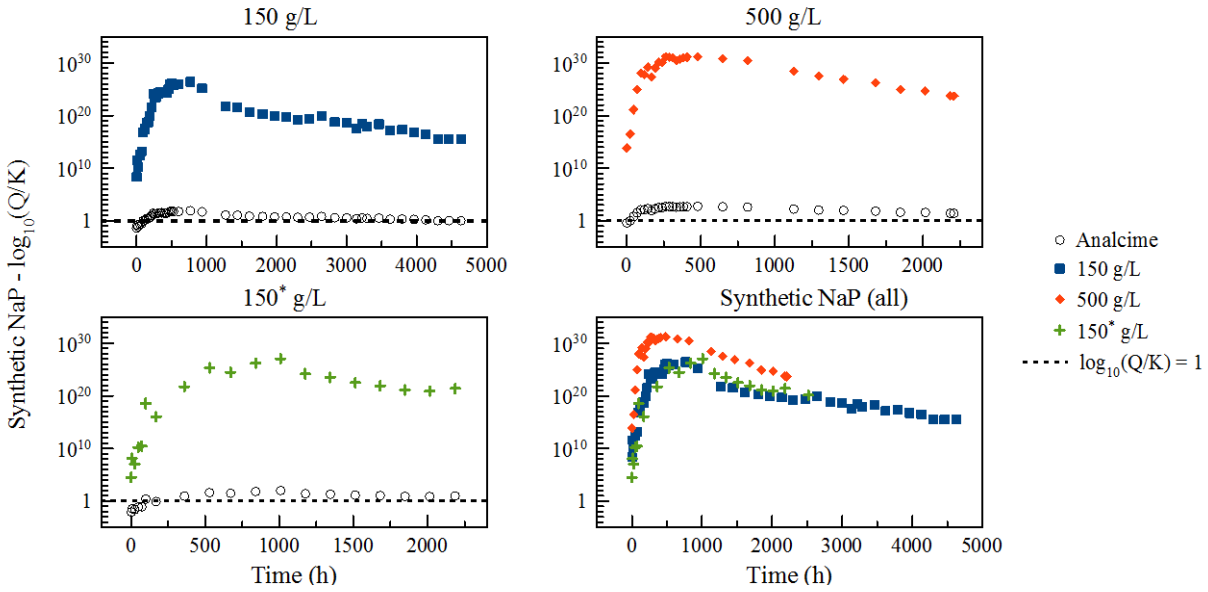

Figure 10: Geochemist's Workbench output for the NDS experiments plotting Q/K for the minerals zeolite NaP1 and analcime.

4. SUMMARY

The results of these experiments indicate that the concentrated glass solutions created with the NDS and LDS glasses exhibit very different behaviors during dissolution with respect to the formation of secondary precipitates. The LDS glass powder dissolved more quickly than the NDS powder; however, the rapid dissolution to the super-saturated state was accompanied by a similarly rapid drop in the concentrations of all three soluble species (Li, Si, Al) to a second set of steady-state concentrations. This rapid concentration drop was associated with the formation of a large amount of secondary precipitates (compared to the amount of secondary precipitates observed in the NDS systems). Of the mass fractions that were examined, the fractional release data for the 10 and 15 g/L LDS experiments indicated that most of the original glass powder had dissolved before the onset of mineral precipitation; however, in the 5 g/L, where a similar complete dissolution of the glass was indicated by the fractional release data, little if any secondary phases were detected over the duration of the experiment. The limited crystallization in the 5 g/L sample could be due to the lack of sufficient driving force (super-saturation was minimal in this case) or insufficient ionic strength to maintain the solution composition. Based on the higher M/V solutions which contained more glass mass and surface area, and their observed congruent fractional release, it seems likely that dissolution and precipitation occurred at a fixed solution composition which must be greater than 5g/L LDS. Qualitatively, the results of the GWB modeling support this interpretation, although the modeling predicted $Li_2Si_2O_5$, while the XRD showed the hydrated disilicate crystalline phase $Li_2Si_2O_5 \cdot 2H_2O$.

In the NDS experiments, the fractional release values were high (and close to unity for 15 g/L) throughout most of the experiment. All three glass solutions revealed the presence of a transparent

gel that first appeared shortly after the experiments were initiated. And for all three glass solutions, secondary precipitates (synthetic zeolite Na-P1, a sodium aluminum silicate hydrate) were observed to form after approximately 1000 h of dissolution/precipitation. The results of the GWB modeling for all three NDS systems confirmed that they were super-saturated with respect to zeolite Na-P1, with a Q/K value much greater in magnitude than for analcime (10^{25} vs 10^{2}).

The outcome of these simple experiments could have been improved with a quantitative measurement of the mass fraction of crystals (in the case of LDS) and gel (in the case of NDS), but such measurements were not possible with the experimental procedures used here. This will be necessary to show a quantitative dissolution of glass and precipitation of mineral at near equilibrium solution conditions. The role of the silica gel phase, and lack of precise thermodynamic data for silica gel, is a fundamental issue that also needs to be addressed in future work. In the context of complex multi-component systems, it is certain that modeling approaches will be required to assess the equilibrium state of the solution, but availability of the necessary thermodynamic data will be a limitation.

5. Acknowledgements

This work funded by the Nuclear Energy University Program (NEUP) DE-NE0000738.

6. References

1. Van Iseghem, et al., GLAMOR, February 2007.
2. Gin, S., et al., Materials Today, Volume 16, Number 6, June 2013.
3. Vienna, J.D., et al., IJAGS, Volume 4, Number 4, pp 283-294, December 2013.
4. Fournier, M., et al., J of Nuc. Mat., Volume 448, Issues 1–3, pp. 348-363, May 2014.
5. Jantzen, C., et al., IJAGS, Volume 1, Issue 1, pp. 38-62, March 2010.
6. Jantzen, C.M., et al., J. of Nuc. Mat., Volume 378, Issue 3, pp. 244-256, 1 Sept 2008.
7. Bethke, C. “The Geochemist's Workbench: A users guide to Rxn, Act2, Tact, React, and Gtplot”. C. Bethke, 1992.
8. Bethke, Craig, and Sharon Yeakel. “Geochemist's Workbench: Release 8.0 Reference Manual.” 2009.
9. Wolery, T., et al. “EQ6, a computer program for reaction path modeling of aqueous geochemical systems: theoretical manual, user's guide and related documentation (Version 7.0).” Lawrence Livermore Laboratory, University of California, 1992.
10. Strachan, D., Neeway, J., App. Geo., Volume 45, pp. 144-157, 2014.
11. Bennington, K., et. al., U.S. Bureau of Mines Report, Volume 8187. US Dept. of the Interior, Bureau of Mines, 1976.
12. Wilkin R, et al., Amer. Mineral., Volume 83, pp. 746 61, 1998.
13. Chermak, J., et al., Amer. Mineral. Volume 74, Issue 9-10, pp. 1023-1031, 1989.

SECTION 3. CORROSION OF ISG FIBERS IN ALKALINE SOLUTIONS (DOI: 10.1111/JACE. 14950)

Received: 11 November 2016 | Accepted: 19 April 2017
DOI: 10.1111/jace.14950

ORIGINAL ARTICLE

Journal of the American Ceramic Society

Corrosion of ISG fibers in alkaline solutions

Cory L. Trivelpiece[1] | Jarrett A. Rice[2] | Nicholas L. Clark[2] | Bernd Kabius[2] | Carol M. Jantzen[1] | Carlo G. Pantano[2]

[1]Savannah River National Laboratory, Aiken, South Carolina
[2]Pennsylvania State University, University Park, Pennsylvania

Correspondence
Cory L. Trivelpiece, Savannah River National Laboratory, Aiken, SC.
Email: cory.trivelpiece@srnl.doe.gov

Abstract

The corrosion behavior of glass fibers synthesized from the International Simple Glass (ISG) reference ingot, an international High-Level Waste (HLW) borosilicate glass standard, is reported. Bundles of glass fibers were submerged in 120 mL of four different solutions of initial pH values (pH_i) of 9.5, 10.5, 11.5, and 12.5 for static corrosion testing. While all the experiments reached a residual corrosion rate after ~50 days, which remained approximately constant for the duration of the pH_i 9.5-11.5 experiments, the pH_i 12.5 experiment underwent a Stage II→III dissolution transition after 57 days. This transition was preceded by a decrease in the Al concentration in solution followed by an increase in B and Si concentration in the leachate. Zeolite NaP2 was observed to form on these fibers via scanning electron microscopy and X-ray diffraction—the crystallinity of the fibers was estimated to be ~40%-45% (relative to amorphous component) after the Stage II→III transition. Transmission electron microscopy cross-sectional imaging of sampled fibers revealed several porous layers on the pH_i 9.5-11.5 samples, and a more aggressive alteration mechanism in the pH_i 12.5 fibers. Potential markers that indicate a transition from Stage II→Stage III corrosion are shown to occur based on experimental observations.

KEYWORDS
borosilicate glass, chemical durability, corrosion/corrosion resistance, fibers, nuclear waste

1 | INTRODUCTION

The long-term storage of high-level nuclear waste (HLW) is a material, geological, and sociological issue that has been studied for the past several decades. Borosilicate glass has been identified as the most well-suited medium for the internment of HLW due to the ease of fabrication and flexible structure of borosilicate glasses to accommodate the species in HLW streams. Borosilicate glasses also have well demonstrated and documented chemical durability [1-10 and references therein]. The prediction of the corrosion behavior of HLW glass compositions is of critical importance to evaluating the radionuclide release from a given waste disposal package over geological time scales, i.e., centuries and millennia.

The release rate of elemental components from glass via corrosion is divided into three distinct stages[11-14]: Stage I) the initial rate—a rapid release of glass components into solution; Stage II) the residual rate—characterized by a pseudo-equilibrium between the alteration layers that form on a corroding glass surface and the contacting leachate solution in which the release of glass constituents occurs orders of magnitude slower than the initial rate; and Stage III) a resumption of alteration—the sudden resumption of glass corrosion at a rate that is orders of magnitude more rapid than the residual rate, but generally not as rapid as the initial rate.[15] The mechanisms of Stage I are very well understood. The specific mechanism(s) governing the pseudo-equilibrium marking Stage II corrosion is still debated[16-18]; however, there is good agreement regarding

the rate drop and the magnitude of the corrosion rate in Stage II—consequently, Stage II corrosion can be described fairly accurately in repository performance assessment models.[19,20] Although much research into the resumption of alteration of HLW glass has been reported, the triggers, mechanisms, and consequences of Stage III corrosion remain elusive[15] (M. Fournier and coauthors, as well as the references contained therein, offer an extensive review of the history of HLW glass corrosion research and the current state of the art).

For certain glasses, the Stage III transition is marked by a dramatic and unpredictable increase in the glass dissolution rate from its otherwise low residual value. The Stage II to Stage III transition is believed to be triggered by some, as of yet unidentified, characteristic of the altered glass surface layer and the contacting aqueous solution, both of which evolve with a strong dependence on glass composition.[15] This transition is enhanced by high pH,[21,22] and is accompanied by the crystallization of secondary mineral phases. During resumption, the crystallization probably creates a thermodynamic driving force for the continued dissolution of the glass, but it is not yet known whether supersaturation and nucleation in solution, crystallization of the amorphous surface layer, or a chemical reaction between the altered surface layer and the solution is the primary mechanism. In general, information about the chemical structure of the altered layer, speciation of soluble and colloidal species in solution, and thermodynamic properties of metastable and equilibrium hydrated phases is lacking.

This study was intended to develop new insights into the Stage II→Stage III transition by utilizing a relatively novel glass form for HLW glass corrosion research: fibers. We focused on fibers of the International Simple Glass (ISG) composition,[23] which contains only six oxide components compared to the 30+ components that are typical of HLW glass compositions. A unique feature of our approach is the use of glass fibers for leaching and corrosion testing. The fibers provide a reproducible and uniform geometry with smooth, defect-free surfaces. The uniform fiber cross sections are ideally suited to cross-sectional scanning electron and transmission electron microscopy (SEM, TEM) analysis of the altered layer and its interface with the bulk glass because it provides a global view of the gel-layer/interdiffusion layer/pristine glass interfaces, and their physical transformation during the Stage II→Stage III transition.

2 | EXPERIMENTAL PROCEDURE

2.1 | Fiber synthesis

ISG fibers were synthesized from pieces of a 500 g block of ISG glass fabricated by MoSci Corp. The crushed pieces of ISG glass were loaded into a platinum single-tip bushing in a laboratory-scale fiber drawing system. The glass in the loaded bushing was conditioned at 1300°C for approximately 1 hour prior to the drawing process. The fibers were drawn at 1125°C and spooled at a constant rate (~320 rpm) by a rotating drum, affixed to a translating table located approximately 1.5 m below the bushing. The density of the as-spooled fiber was measured by He-pycnometry as 2.50±0.2 g/cm^3. The physical surface area was measured via the Brunauer-Emmett-Teller (BET) method at 0.3256 m^2/g, and the diameter of the fiber was measured from electron micrographs analyzed with ImageJ software at 5.00±0.2 μm. There was little discrepancy between the BET surface area and the geometric surface area of the fibers used for these experiments. The geometric-specific surface area of a fiber is described by Equation 1:

$$S_\rho = \frac{4}{\rho d} \quad (1)$$

where ρ is the measured density of the fibers and d is the fiber diameter. Using Equation 1, the geometric-specific surface area was determined to be 0.3200 m^2/g, which is within 2% of the measured BET surface area. There are two reasons why there was little difference between the two values for fibers (a difference that can be quite significant when using powder waste form specimens):

1. The diameters of the fibers are small compared to the typical glass powder size used in corrosion experiments (d_{fiber}=5 μm, d_{powder}=112.5 μm for PCT[24]). The accuracy of BET is particle size dependent with smaller diameter specimens producing results that are closer to geometric value.
2. The uniform and smooth surfaces of fibers do not introduce additional errors associated with irregular shapes and cracks that are akin to larger diameter powder specimens.

The nominal and measured compositions are compared in Table 1; the Zr was approximately one weight percent

TABLE 1 Nominal and measured (ICP-AES) composition of the ISG fiber synthesized for this work

Oxide	Mol%	Wt%	Measured fiber oxide wt%
SiO_2	60.1	56.2	56.6
B_2O_3	16.0	17.3	16.6
Na_2O	12.6	12.2	12.3
CaO	5.7	5.0	4.9
Al_2O_3	3.8	6.1	6.3
ZrO_2	1.7	3.3	2.3

lower than the reference ingot's nominal value. The freshly drawn fiber was analyzed by SEM and X-ray diffraction (XRD) to ensure amorphousness and homogeneity.

Given the extremely fast quench rate associated with the fiber draw process (~10^6 K/s), the fictive temperature of the as-drawn fibers was likely higher than the as-poured, annealed reference ingot. Consequently, it was expected that the $B^{(3)}/B^{(4)}$ ratio was higher in the fiber than in the as-received, original ISG block, and this difference would probably affect the reaction kinetics between the two glass forms. However, as this work was primarily concerned with evaluating fibers as a new waste form for studying HLW glass corrosion and investigating the structural changes in the glass during corrosion at different starting pH values, we determined that the effects of the higher $B^{(3)}/B^{(4)}$ ratio could be neglected for the purposes of this study.

The fiber spool was cut into sections weighing between 0.05 and 0.2 g with an average mass of 0.1 g. These small sections of fiber were then tied into bundles using approximately 30 cm of polytetrafluoroethylene (PTFE) thread, and the entire mass of the fiber bundle was measured. This careful tracking of the total mass allowed for weight loss determinations of the individual fiber bundles throughout the experiment. The fiber bundles were then separated into four groups of eight bundles per group. The PTFE thread not only held specific masses of fiber together, but also facilitated the removal of fiber bundles from solution throughout the experiment.

2.2 | Experimental setup

Four alkaline solutions were prepared by titrating 1.0 mol/L NaOH into ASTM Type I water to yield pH values of 9.5, 10.5, 11.5, and 12.5 (measured at room temperature). Using these solutions, four corrosion experiments were initiated—one at each pH value—by placing a group of eight bundles into a 120 mL perfluoroalkyl (PFA) digestion vessel (Savillex®) and filling the vessel with one of the four solutions. A portion of the PTFE thread from each bundle remained outside of the digestion vessel throughout the experiments and was used to periodically remove bundles from the vessels during the course of the experiments for characterization analysis. Aliquots (5 mL) of the solution were also removed periodically during the course of the experiments for solution and pH analyses. To keep a constant volume of solution in the vessels during the experiments, the solution volume removed per aliquot was replaced with fresh ASTM Type I water; therefore, these experiments were not entirely static but rather maintained in a "quasi-static" state with an extremely low flow rate ($q/S \approx 10^{-10}$ m/s). The tests were conducted 90°C in a forced convection oven (VWR Symphony®). Table 2 gives the experimental parameters for the four initial tests—Figure 1 is a photograph of a test vessel prior to being filled with solution and placed in the oven.

TABLE 2 Experimental parameters for the four static corrosion tests

Experiment	Initial pH (pH_i)	Initial SA/V (m^{-1})	Initial fiber mass (g)
1	9.5	2610	0.9615
2	10.5	2220	0.8171
3	11.5	1650	0.6066
4	12.5	1640	0.6044

2.3 | Analysis methods

Aliquots of leachate solutions were periodically removed from each of the sample vessels. The 5 mL aliquots were separated into two vials: (i) a 3 mL sample that was immediately refrigerated and kept cold until concentration analyses via ICP-AES, and (ii) a 2 mL sample that was used for pH analysis. The detection limits for the analytes of interest in this study are given in Table 3.

The periodic removal of solutions, and subsequent replacement with fresh water, complicates the determination of normalized loss and fractional release from the fibers. However, a method was developed to correct for any apparent drop in solution concentrations caused by the sampling. This was achieved by correcting the

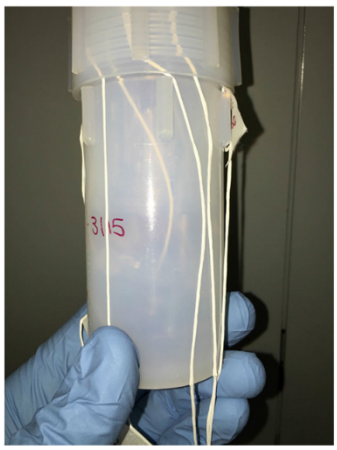

FIGURE 1 An example of the experimental vessel with ISG fiber bundles placed inside similar to the vessels in the pH_i 9.5-12.5 experiments

TABLE 3 Detection limits of the elements analyzed by ICP-AES as reported by the Emission Spectroscopy Laboratory at Penn State University

Element	Detection limit (mg/L)
Al	0.01
B	0.45
Ca	0.001
Na	0.08
Si	0.001
Zr	0.001

concentration values used in the normalized loss and fractional release calculations by Equation 2.

$$C^*_{i,j} = C_{i,j} + \frac{V^a}{V^s}\sum_{j}^{N} C_{i,j\text{-}1};\ C_{i,0} = 0 \tag{2}$$

where $C^*_{i,j}$ is corrected concentration of element "i" at time "j"; $C_{i,j}$ is measured concentration of element "i" at time "j"; V^a is volume of a sample aliquot; V^s is volume of solution in digestion vessel; $C_{i,j\text{-}1}$ is measured concentration of element "i" at time "j-1"; and $C_{i,0}$ is initial concentration of element "i" in experiment.

This summation allowed for more precise tracking of elements released from the fibers during the experiment. It should be noted that the actual measured solution concentrations were used for all other calculations (e.g., strong base, weak acid, and mineral saturation index calculations). As the pH values of the initial solutions were adjusted with NaOH, a background concentration of Na corresponding to this initial adjustment was subtracted from the measured Na concentrations at each sampling interval such that only Na released from the fibers was considered in the calculations of normalized loss and fractional release.

Normalized loss (NL) and fractional release (FR) values were calculated using the corrected concentrations (see Equation 2) according to Equations 3 and 4 below:

$$\mathrm{NL} = \frac{C^*_i}{\left(\frac{\mathrm{SA}}{V}\right)f_i} = \frac{C^*_i}{\left(\frac{S_p m_g}{V}\right)f_i} \tag{3}$$

where NL is normalized loss (g/m^2); FR is fractional release (dimensionless); C^*_i is corrected concentration (g/L); SA is surface area (m^2); S_p is specific surface area (m^2/g); m_g is mass of glass fiber (g); V is volume of solution (L); f_i is mass fraction of element i.

$$\mathrm{FR} = \frac{C^*_i V}{m_g f_i} \tag{4}$$

The surface area term in Equation 3 was adjusted according to the reaction progress of the respective experiment to account for the decreasing surface area of the pristine glass fiber throughout the course of the experiment. The correction was based on the equivalent thickness of boron leached from each experiment at the various sampling intervals. It should be noted that this is not an overall surface area correction, but rather a correction to the "active" surface area of the pristine glass from which bulk glass constituents could dissolve.

The pH values of the solutions were measured with every aliquot collection. The 2 mL aliquots of solution for pH measurements were cooled down from 90°C by forced air convection to room temperature within 5 minutes of sampling, and the pH values were immediately measured after the cooling. The pH meter (Thermo Scientific Orion Star™) was calibrated prior to any measurements described in this study using standard buffer solutions at pH 4, 7, and 10.

The measured concentration data were also used to calculate the excess strong base or weak acid in the solution according to a model proposed by Jantzen, et al.[25-27] In this context, strong bases are composed of elements that produce one mole of hydroxide per mole of dissolved element; for ISG, the only glass components that are capable of undergoing this reaction are Na_2O and CaO. A weak acid is composed of elements that produce less than one mole of free hydrogen per mole of dissolved glass species; in ISG, SiO_2, B_2O_3, and Al_2O_3 are all capable of forming weak acids in solution. The excess strong base or weak acid is calculated by Equation 5.

$$[\mathrm{SB}]-[\mathrm{WA}] = \left(\frac{C_{\mathrm{Na}}}{m_{\mathrm{Na}}} + \frac{C_{\mathrm{Ca}}}{m_{\mathrm{Ca}}}\right) - \left(\frac{C_{\mathrm{Si}}}{m_{\mathrm{Si}}} + \frac{C_{\mathrm{B}}}{m_{\mathrm{B}}} + \frac{C_{\mathrm{Al}}}{m_{\mathrm{Al}}}\right)\frac{\mathrm{mmol}}{L} \tag{5}$$

In Equation 5, [SB] and [WA] are the molar concentrations of strong base and weak acid, respectively. C_x is the concentration of element "x" in the solution, and m_x is the molar mass of element "x" in solution.

2.4 | Fiber characterization

Periodically, fiber bundles were removed from the digestion vessels for examination with various characterization methods. After removal, each bundle was rinsed for approximately 30 seconds with deionized water before being placed in a plastic petri dish and loaded into a convection oven held at 75°C to dry for at least 24 hours. The dried bundles were then weighed and stored before being analyzed further. Snippets of fiber were removed from the bundles for analysis with X-ray diffraction (XRD), scanning electron microscopy (SEM), X-ray photoelectron spectroscopy (XPS), and focused ion beam milling (FIB) for transmission electron microscopy (TEM).

The fiber snippets that were examined with XRD were crushed into powder and loaded into a single-crystal Si, zero-background holder for the diffraction measurement. The snippets were crushed to ensure a representative sampling of the fiber bundle. Mineral phases were identified using the diffraction analysis software Jade™ (Materials Data Incorporated), and a modified Rietveld analysis was used to determine the crystallinity (%crystalline/%amorphous) of the crushed glass powder. The fiber snippets that were analyzed with XPS were UV-ozone cleaned immediately prior to being loaded into the XPS vacuum chamber to minimize any adventitious carbon buildup. Samples that were studied with SEM or FIB/TEM were coated with Au or Ir to reduce sample charging during the analysis.

3 | RESULTS

3.1 | Solution analysis

The results of the pH measurements at the various sampling intervals for the four experiments are given in Figure 2. The measured pH values for the original experiments indicate that both the pH_i 9.5 and 10.5 experiments quickly buffered to a value of ~9.6 and remained constant for the duration of the experiment. The pH_i 11.5 experiment also initially buffered to a lower value (pH 9.7); of course, the change in the OH^- activity associated with this drop in pH is higher than for the pH_i 10.5 experiments. The pH_i 12.5 experiment underwent a similar initial drop and remained nearly constant at pH 12.3 until the onset of a Stage II to Stage III corrosion transition at 55 days. After this transition, the pH value of this solution started to decrease, and continued to drop for the duration of this experiment.

The results of the normalized loss calculations for the four experiments are given in Figure 3. The pH_i 9.5-11.5

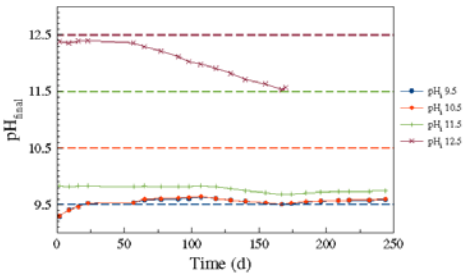

FIGURE 2 The measured pH values for the four original experiments (pH_i 9.5-12.5). The horizontal dashed lines represent the initial pH values of the original experiments

experiments showed similar corrosion trends: an increase in the initial concentration of the major glass components, B and Si, and then a decrease in the corrosion rate as the reaction transitioned to the Stage II residual rate. The pH_i 12.5 system followed this same trend initially (the background concentration of Na was significantly higher in this system); however, at 55 days the rate of B and Si release suddenly increased indicating a transition from Stage II to Stage III corrosion, which was accompanied by a rapid decrease in the Al concentration to just above the detection limit. After a period of approximately 40-50 days at this accelerated corrosion rate, the concentrations of B and Si then leveled off to a new residual rate which was nearly constant for the remainder of the experiment. (Note: The pH_i 12.5 experiment was terminated at an earlier date than the other three experiments, and the material from this experiment was used to initiate new experiments, which will be reported in the future.)

Figure 4 presents this same normalized loss data sorted by element where the similarities in the corrosion behavior of the pH_i 9.5-11.5 experiments are clearly evident while the unique Stage III behavior of the pH_i 12.5 experiment stands out. One observation made here that has not yet been reported relevant to Stage III behavior is the initial decrease in the Ca concentration followed by the resumption in Ca release as the system transitions to Stage III.

The fractional releases of elements from the fibers in the various experiments, not surprisingly, follow the same trends as the normalized losses and are not presented here for brevity. However, we will note that, according to the B release, the fibers in the pH_i 9.5-11.5 experiments were approximately 60% reacted at the termination of the experiment (i.e., FR ~0.6), and after the Stage II→III transition, the fibers in the pH_i 12.5 experiment were approximately 90% reacted. Before the pH_i 12.5 sample transitions to Stage III, the extent of reaction for its network formers, Al and Si, was approximately 20% and exceeded the network former fractional release for the three other experiments. After the transition to Stage III, nearly all of the B and 50% of the Si were leached from the pH_i 12.5 fibers. It is also noteworthy that the fractional release for B, Al, and Ca is nearly identical for the pH_i 9.5, 10.5, and 11.5 experiments, but there was a measurable difference in the case of Si for the pH_i 11.5 sample.

3.2 | Fiber characterization

Fiber bundles from the various experiments were periodically examined with XRD to detect and identify any secondary mineral phases provided they were present in sufficient quantities to obtain a diffraction pattern. All of the fiber bundles examined from the pH_i 9.5-11.5 experiments were XRD amorphous; although, the SEM images

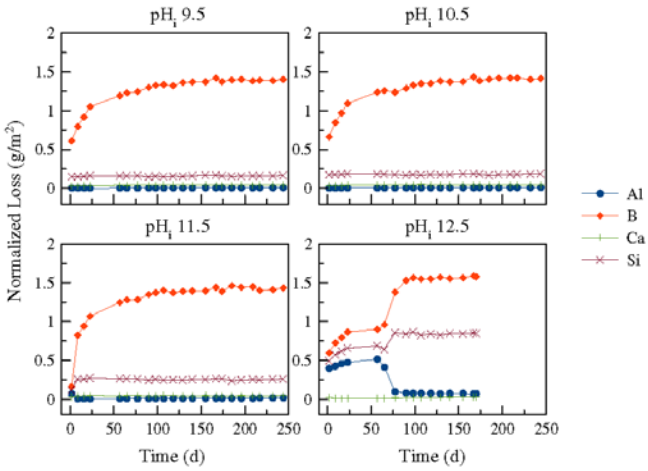

FIGURE 3 The normalized loss values for the four original experiments, pH$_i$ 9.5-12.5. The transition from Stage II to Stage III corrosion in the pH$_i$ 12.5 experiment was marked by the sudden increase in the B and Si concentration at 55 days

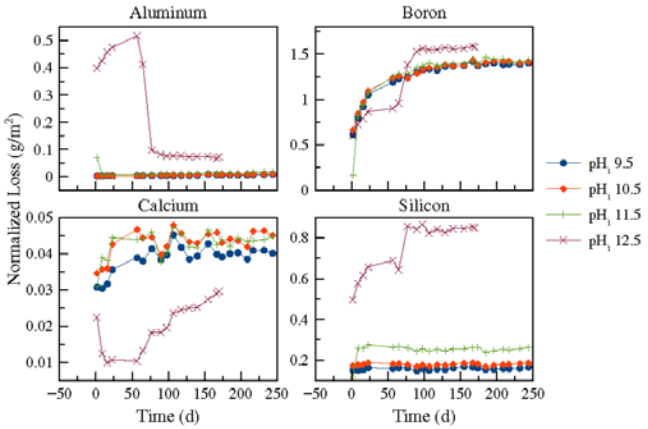

FIGURE 4 The normalized loss values by element for the four original experiments, pH$_i$ 9.5-12.5

presented later show crystal formation on the fiber surfaces, primarily the appearance of Ca-silicate hydrate (CSH) and possibly some zeolitic minerals.

A strong diffraction pattern was observed from the pH$_i$ 12.5 fiber bundles that were collected during and after the Stage II to Stage III transition. The mineral phase was identified as zeolite NaP2. The XRD data are presented in Figure 5 for four fiber bundles extracted from the pH$_i$ 12.5 experiment before and after the transition. In addition to identifying the zeolite NaP2 mineral, a modified Rietveld refinement technique was employed to determine the percent crystallinity of the fibers for the pH$_i$ 12.5 sample. The technique, called whole pattern fitting (WPF), indicated that after the Stage II to Stage III transition, approximately 40%-45% of the pH$_i$ 12.5 sample was crystalline. The WPF estimates are given in Figure 5 for the 77 and 98 days samples.

Both scanning and transmission electron microscopy were employed to inspect the sampled fiber bundles throughout the corrosion experiments. The surfaces of fibers and in some cases cross-sections were observed by SEM, while focused ion beam milling (FIB) was employed to prepare samples for cross-sectional analysis at high resolution with TEM. SEM imaging was most useful for showing the presence of crystals even under conditions where their concentration was below the detection limit of XRD. Secondary mineral phases were observed to form on the leached fiber surfaces throughout the experiments. Some

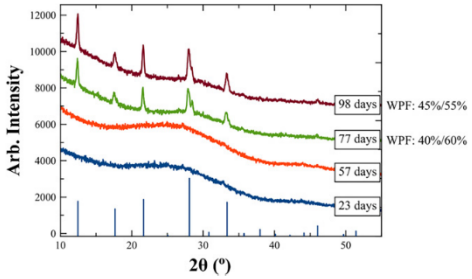

FIGURE 5 Diffraction patterns obtained from pH_i 12.5 fiber bundles before and after the Stage II to Stage III transition. The vertical blue lines normal to the *x*-axis demarcate the major peaks in the diffraction pattern for zeolite NaP2. Also given are the WPF estimates of the percent crystalline/percent amorphous material amounts for the respective samples

selected images of these formations are presented in Figure 6. Large concentrations of secondary mineral phases were only observed in the pH_i 12.5 experiment (detectable with XRD); however, more sparsely distributed secondary phases, with crystalline facets, were also observed in the other experiments with SEM.

The TEM was utilized to provide global images of the alteration layers on these 5 μm fibers, especially their composition by energy-dispersive X-ray analysis (EDX) and electron energy loss spectroscopy (EELS), as well as especially high-resolution analysis of potential secondary-phase nucleation sites in the gel layer. Figure 7 shows the existence of at least two well-defined and uniform alteration layers on the pH_i 9.5 and 10.5 experiments at 77 days and likely the presence of more complex stratification in the outer layer. The outer alteration layer was observed to be more porous compared to the inner 'ion-exchange' layer. The EDX mapping of the elemental distribution in these layers indicated that the outer layer has a lower concentration of Si and O than the inner layer, but uniform Al and Zr concentrations, which provided further evidence of the porosity difference between the layers. Sodium has been completely depleted from the entire reaction zone (all alteration layers) in both sets of fibers. It is also noteworthy that the layers on the two different fibers (9.5 vs 10.5) appear to be nearly identical in terms of relative layer thickness and changing porosity from the inner core to the outer layers. This is perhaps not surprising given that the ICP solution analyses and the pH measurements of the solutions for these two systems were nearly identical throughout the course of the experiments. The layers thicknesses were measured using ImageJ® (NIH) and found to agree with the equivalent thicknesses determined from the normalized loss values of boron (i.e., NL_B/ρ). For example, at 77 days the equivalent thickness of the leached layer on the pH_i 9.5 and 10.5 specimens is 0.67 μm. The measured layer thickness at 77 days on each fiber specimen was approximately 0.75 μm. Although not easily seen in these printed images,

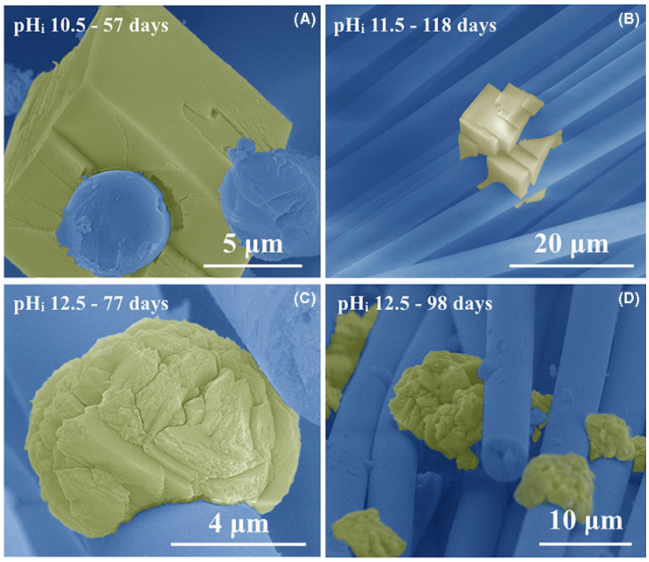

FIGURE 6 SEM images of secondary mineral formations (crystalline) on the fibers collected at various times throughout the corrosion experiments. Crystals were observed on fibers from the pH_i 10.5 and 11.5 experiments (A and B). A large amount of secondary phase, relative to that observed on the lower pH experiments, was observed on the pH_i 12.5 fiber snippets after the Stage II to Stage III corrosion transition in agreement with the XRD data in Figure 5 (C and D)

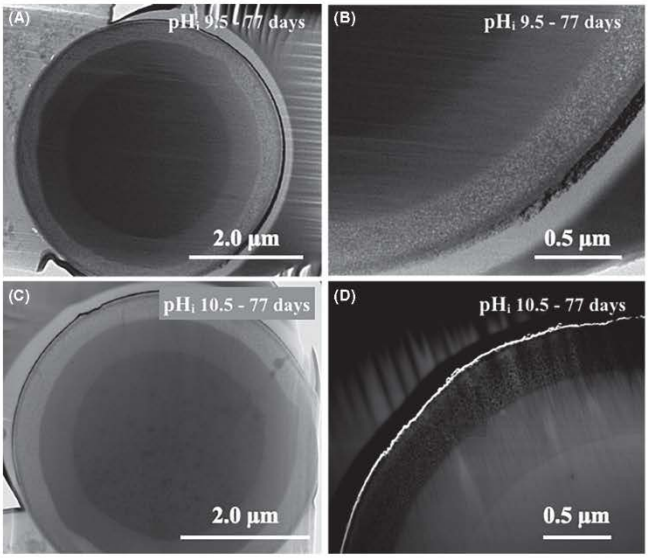

FIGURE 7 TEM bright-field (A,B,C) and STEM high-angle dark-field (HAADF) images (D) of the alteration layers formed during the corrosion process in the pH$_i$ 9.5 and 10.5 experiments after 77 days of leach time. EDX analysis showed that the ratio of Si and O is similar for the core and the two layers. The contrast difference in the HAADF image (D) can be explained by increasing porosity for darker areas

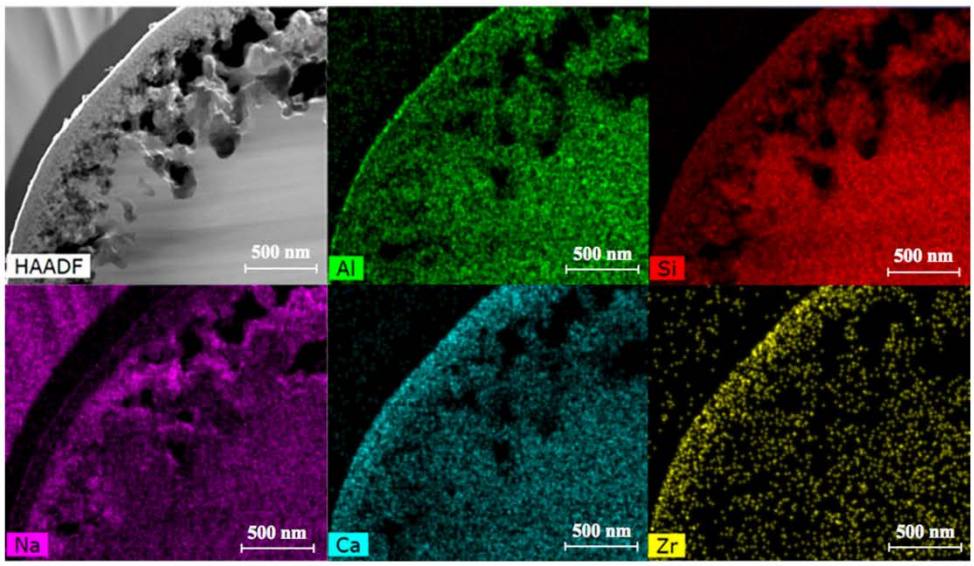

FIGURE 8 STEM dark-field image and corresponding EDS maps of the elemental composition for the pH$_i$ 12.5 sample after 57 days. This is just prior to the Stage III transition as detected by the solution analysis and XRD data

there is sometimes a third, very thin but distinct layer, observed outside the porous gel layer, (perhaps part of the stratification alluded to earlier). This layer tended to be denser than the porous 'gel layer' (which can be seen clearly in Figure 7), and according to EDX and EELS, it was enriched in Al.

Figure 8 shows the TEM cross section with associated EDX maps for the pH_i 12.5 at 57 days, obtained just prior to the Stage III transition and the formation of XRD detectable secondary phases. It was evident from these images, as well as several others not presented here, that the high rate dissolution of the fiber during the Stage II to Stage III transition was not a uniform attack at the glass fiber surface. Rather, there appeared to be dissolution and disintegration of the fiber from within the inner-altered layers leaving a thin, but dense Ca-Zr enriched outer surface layer, which was apparently resistant to the disintegration mechanism that affected the inner alteration layers. This Ca-Zr outer region has been observed in prior studies on ISG monoliths.[21] In many cases, disintegration seemed to initiate within the altered layer at the interface with pristine glass, as shown by the very large pores in Figure 8.

The composition of the outermost layer of the altered glass surface was measured using XPS (outer 10 nm). Table 4 gives the atomic percent compositions for all the fiber samples over the period up to 217 days. The continued presence of some Na, and the preferential surface sorption of Ca and Mg (a 0.033% impurity in the glass), which could subsequently serve to nucleate secondary crystalline phases, are clearly evident. Using these data, the outer gel-layer compositions are plotted on the ternary diagram in Figure 9 in terms of the network formers, Si and Al, and the sum of modifiers. It can be seen that the layer composition for the pH_i 12.5 experiment evolves in a unique way when compared to the lower pH_i experiments. The effect of this on the gel-layer structure is discussed later.

TABLE 4 Fiber surface layer compositions determined by XPS (in atom percent)

	Time	O	Si	Al	B	Ca	Na	Zr	Mg
Control	–	60.2	17.8	2.2	9.6	1.6	8.7	0.4	—
pH_i 9.5	23	66.8	23.3	2.9	—	5.3	1.8	0.9	—
	57	67.1	23.6	2.7	—	4.2	1.7	2.4	0.7
	77	65.9	24.3	3.5	—	3.3	2.1	1.4	0.8
	118	65.9	23.8	3.3	—	4.4	1.8	1.4	0.9
	155	65.6	22.9	4.6	—	4.0	2.0	1.7	0.8
	217	62.3	25.2	3.9	—	5.6	1.8	1.4	1.3
pH_i 10.5	23	66.2	24.6	3.8	—	3.5	1.9	1.5	—
	57	63.7	25.7	3.4	—	5.0	2.2	1.9	—
	77	65.2	24.6	3.7	—	4.2	1.6	2.4	0.7
	118	66.5	24.2	3.9	—	3.5	1.9	1.2	—
	155	65.2	24.3	4.4	—	4.1	1.9	2.0	0.2
	217	64.0	25.7	4.8	—	2.6	1.7	1.3	1.3
pH_i 11.5	23	66.1	22.4	3.4	—	5.5	1.5	3.0	1.2
	57	64.9	23.4	3.1	—	5.5	1.5	2.9	1.6
	77	65.4	22.8	4.4	—	4.2	2.2	1.5	1.1
	118	63.7	22.1	3.6	—	5.9	1.7	2.7	3.0
	155	63.9	23.6	4.1	—	5.0	1.6	1.7	1.8
	217	66.4	24.3	2.6	—	2.9	1.3	3.5	2.6
pH_i 12.5	23	64.6	17.8	3.6	—	9.1	3.6	3.5	1.2
	57	65.6	18.3	3.6	—	7.9	3.0	3.2	1.5
	77	65.0	19.0	3.0	—	6.9	3.2	2.6	2.9
	98	64.9	20.4	2.7	—	6.4	2.5	2.5	3.1
	118	65.7	19.8	2.4	—	6.3	2.5	2.3	3.4
	155	64.8	20.2	2.1	—	7.0	2.4	2.4	3.5

4 | DISCUSSION

The data presented in this study confirm the strong solution chemistry dependence of the Stage II to Stage III transition for the ISG composition, which is a simplified version of SON68. Long-term PCT experiments have suggested that SON68 is not especially prone to resumption of alteration; however, experiments conducted far from neutral pH (pH>11.5) have shown that the mineral phases we observed in this work with ISG are similar to those that have been observed in studies of SON68.[28-31] On the other hand, another widely studied glass, AFCI, has been shown to be susceptible to Stage III corrosion via long-term PCT where these mineral phases have also been observed.[27] Identifying potential triggering mechanisms for this resumption based on the identity of observed crystalline precipitates has been the focus of many recent studies.

In this study, we conducted four separate experiments with the initial pH values of the leachate solutions at 9.5, 10.5, 11.5, and 12.5 using 1.0 mol/L NaOH. Of these four

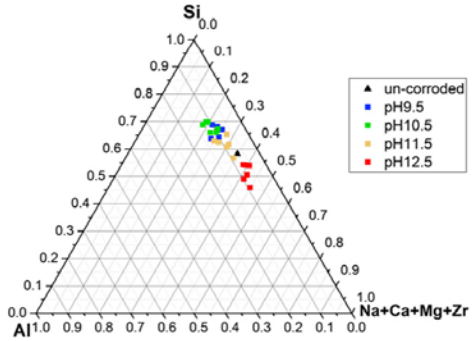

FIGURE 9 This ternary diagram summarizes the evolution of the outermost gel-layer composition (in atom percent) in terms of Si, Al, and the sum of modifiers obtained by XPS. The plotted points for each experiment represent corrosion times up to 217 days

experiments, the three lowest initial pH values buffered within 2 days to values between approximately 9.3-9.7 due to the release of acidic B and Si species from the glass as well as CO_2 gas interaction with the leachate solution. In the case of the pH_i 12.5 experiment, there was a similar buffering observed, but based on the observed pH change (12.5-12.3), seemingly to a much lesser extent. In fact, the change in OH^- concentration associated with a pH decrease from 12.5 to 12.3 is significantly greater than any of the other self-buffering mechanisms that were observed; however, this measured change could be within the instrumental error of the pH meter at this high pH value.

A series of simulations were conducted using the software package, Geochemist's Workbench® 11 (GWB) (Aqueous Solutions), to elucidate potential mechanisms of the measured pH drop in the various experiments that occurred from the time the experiments were initiated (t=0) until the first aliquots were sampled and analyzed (t=1.83 days). The starting conditions of each solution were mimicked in four separate initial systems—Na+ was added to the experimental volume of water to achieve the desired pH values at room temperature. The simulations then proceeded at 90°C under three different reaction scenarios:

1. The solution was allowed to equilibrate with atmospheric CO_2(g) only.
2. Only effects of the glass constituents were considered by dissolving amounts of glass species into the solution based on the concentrations that were measured via ICP-AES at t=1.83. In this scenario, any interaction with atmospheric CO_2(g) was excluded from the system.
3. A combination of scenarios 1 and 2 in which the glass constituents were dissolved and the simulated leachate solutions were allowed to equilibrate with atmospheric CO_2(g).

The final step in each of the 12 simulations (four initial pH values * three scenarios) mimicked the rapid cooling of the aliquots to room temperature for pH measurement. The outcomes of the various simulations are illustrated in Figure 10. The results of the simulations indicated that both glass dissolution and CO_2(g) ingress were responsible for the rapid drop in pH for the pH_i 9.5-11.5 systems from t=0 to 1.83 days, especially in the pH_i 11.5 experiment. The variation between glass-only and the combination scenarios was small for the pH_i 9.5 and 10.5 experiments relative to the pH_i 11.5 system, but was nonetheless apparent in the results. In the pH_i 11.5 experiment that considered only glass dissolution, the final predicted pH was significantly higher than what was measured. Interestingly, in this same system, the results of the GWB simulation indicated that the pH value is predominantly controlled by CO_2(g) equilibrium rather than the glass dissolution. The pH_i 12.5 system showed a marked difference from the other systems in terms of the simulation—the simulation results indicate that the pH is almost independent of CO_2 ingress.

Despite the small but apparent [OH^-] decrease in the pH_i 12.5 experiment, the leachate pH remained sufficiently high to drive a more complete dissolution of the glass network. This is evident in the solution analysis data of Figure 3 where the release of Al is nearly an order of magnitude higher than the lower pH_i experiments in the first 50 days (up until the Stage III transition occurs). The higher NL values in the pH_i 12.5 experiment were due to both kinetic and thermodynamic effects; the higher OH^- activity increased the rate of Si-O bond rupture and also raised the silica solubility in solution. One important impact of this pH effect was that the composition and structure of the alteration layer was very different at pH_i 12.5, most notably with respect to Al. This is discussed further below.

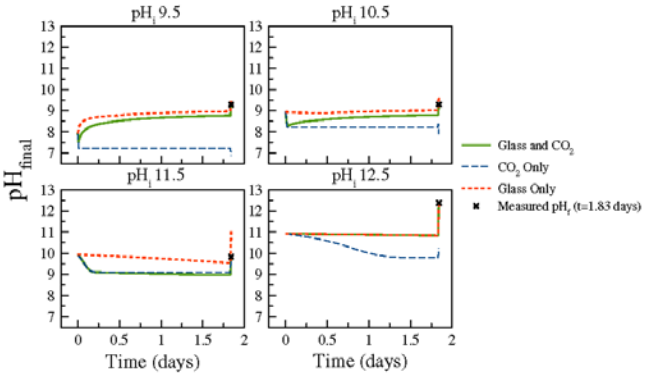

FIGURE 10 The results of the GWB simulations indicated that for the pH_i 9.5-11.5 experiments the initial pH drop was caused by glass dissolution as well as the equilibration of the solution with atmospheric CO_2. However, the apparent measured drop in the pH_i 12.5 experiment was likely caused only by glass dissolution

According to a conceptual model proposed by Jantzen, et al.,[25-27] the OH^- concentration and the factors that control it are of primary relevance to the occurrence of the Stage II→Stage III transition. This conceptual model correlates the presence of excess strong base in the solution (SB_{ex}) to the likelihood of resumption of alteration in that more SB_{ex} indicates a higher propensity for a given corroding glass system to resume alteration. Correspondingly, an excess of weak acid (WA_{ex}) or an equilibrium between SB and WA ([SB]-[WA]=0) is indicative of a corroding system that is not likely to undergo resumption of alteration. Strong bases in solution are represented by hydrolyzed alkali and alkaline earth metal oxides such as Na_2O and CaO, whereas weak acids are represented by the hydrolyzed glass components such as SiO_2 and B_2O_3. The measured concentrations of Al, B, Ca, Na, and Si were used in Equation 5 to determine the difference between SB and WA for the four experiments reported here, and the results of these calculations are shown in Figure 11. Only the pH_i 12.5 experiment generated SB_{ex} during the experiment, and this excess strong base was not solely caused by dissolution of the fiber, but rather the high starting OH^- concentration associated with pH 12.5. Nonetheless, the pH_i 12.5 experiment was also the only system to undergo a Stage II→Stage III transition. After the transition, the system began to produce excess weak acid (resumption of B and Si release to an accelerated rate) while no significant amounts of strong base were added to the system, which caused the SB-WA to decrease toward the equilibrium value of SB-WA=0. The lower pH_i experiments (i.e., 9.5-11.5) produced excess weak acid in the form of B and Si aqueous species throughout the duration of the experiments. None of these lower pH experiments showed a resumption of alteration lending more evidence to the pH/OH^- dependence of resumption.

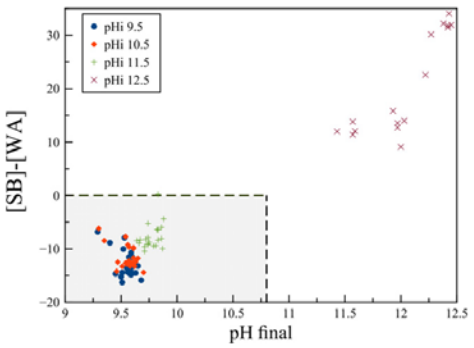

FIGURE 11 Strong base/weak acid calculations for the four original experiments and two amended experiments. The presence of (SB)ex in the pH_i 12.5 experiment further demonstrates that the system likely underwent a transition from Stage II to Stage III corrosion. The vertical line at pH 10.8 indicates the critical pH value for resumption of alteration established by Ribet, et al. [30]

The model described above proposes that the excess strong base in the contacting solution can react with the gel layer on the altered glass surface to nucleate zeolite and related crystals. These crystalline phases consume the silicon and aluminum that comprise the gel layer. This eliminates the passivation provided by the altered surface layer and exposes the unreacted/pristine glass to high-rate dissolution by the strong base in the contacting solution. In this instance, there are now two thermodynamic sinks for bulk glass components: (i) increased affinity between the solution and the bulk glass as a result of the loss of passivating properties of the alteration layer, and (ii) secondary mineral phases with a low free energy consuming glass components such as Al, Na, Si (for sodium-based zeolites in particular). It is possible that the release of B from the pristine glass can arrest the resumption of alteration by creating excess weak acid in the contacting solution thereby reducing the mineralizing potential of excess hydroxide.[32]

To further characterize features of the corroded glass which are relevant to this model, the gel-layer compositions were measured directly by XPS (see Table 4 and Figure 9). Although it is also possible to calculate the average layer composition based on the incongruency of the solution composition, that calculation requires an assumption that there are no solid or colloidal species in the system; whereas XPS measures the surface layer composition directly. Figure 9 showed the unique behavior of the gel surface layer composition for the pH_i 12.5 system that exhibited Stage III behavior. The pH_i 12.5 gel surface layer composition tends toward lower silica content with time, whereas the lower pH_i samples exhibit surface layers, which trend toward higher silica content. One effect of this diminishing Si concentration in the gel is an increase in the Al/Si ratio. This Al/Si ratio discrepancy suggests a possible structural difference in the gel surface between the resumption and nonresumption fibers. As XPS provides a measure of the oxygen content, in addition to the cations (but unfortunately, not hydrogen), it is possible to estimate the connectivity and structural units that comprise the hydrated surface layer. Figure 12 plots the oxygen-to-network forming cation ratio, calculated from the XPS compositions for the gel layers. Those ratios can be associated with specific structural units for silicates.[33,34] Although only an estimate of the network structure associated with the gel surface layer, we observed that the low pH systems trended toward stable 3D networks, while the high pH condition, notably pHi 12.5, had a fragmented network. The fragmented network implies the presence of more modifier species and

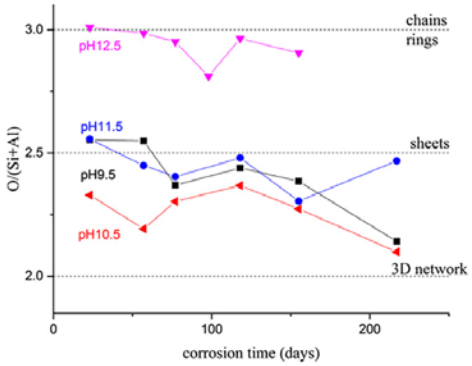

FIGURE 12 The oxygen to network-forming cation ratios based on the XPS compositional analysis of the gel layers show a dependence on pH. This ratio provides insight to the connectivity and structural units that comprise the gel layer

enhanced water mobility, both of which could facilitate atomic rearrangements, precipitation, and crystallization of secondary phases.[35]

During the transition from Stage II→Stage III corrosion, we observed the formation of a significant volume of crystals forming in the pH_i 12.5 experiment. The primary phase that was identified was Zeolite NaP2. Secondary crystalline phases were also observed to form on the lower pH experiments with microscopy, but the bulk material from these experiments was XRD amorphous throughout the experimental duration. It is interesting to note the cubic nature of the crystals that formed on the fibers in the lower pH experiments compared to the crystals that formed during the pH_i 12.5 experiment. It has been shown that the morphology of zeolite NaP family minerals is directly related to the SiO_2/Al_2O_3 ratio in the precursor gel (alteration layer).[36-40] This differing morphology is likely a further indication of the variations in the stoichiometry of the alteration layers in the various experiments and their effect on the type of secondary mineral phases that form during alteration. The fact that crystals form in the lower pH experiments is evidence that while the alteration layer/solution chemistry is conducive to localized crystalline precipitation in these experiments, another factor was controlling the transition to Stage III corrosion in the pH_i 12.5 experiment.

Given these insights from the characterization of the solutions and fibers, GWB was also utilized to further elucidate similarities and differences between the four experiments that may be responsible for the consistent behavior for pH_i 9.5-11.5 systems and the markedly different behavior of the pH_i 12.5 experiment. The measured concentration data were input into various GWB software modules to determine activities of several anionic species and the saturation indexes of secondary mineral phases, which were surmised to be influencing the behavior of the corroding fibers. The GWB calculations indicated that all four experimental systems were supersaturated with respect to several minerals, most predominantly with Zeolite NaP2, which was consistent with SEM and XRD data collected from the fibers. The most prevalent aqueous Al and Na species in all the systems were the $Al(OH)_4^-$ and the Na^+ ions, respectively. Figure 13A shows the logarithm of the $Al(OH)_4^-$ activity as well as the logarithm of the saturation indexes vs time for the four experiments. The most notable feature in these data was the drop in the saturation index of the pH_i 12.5 experiment after the transition from Stage II to Stage III corrosion to a value that was less than the saturation indexes in the other three experiments. Also, the $Al(OH)_4^-$ concentration was significantly higher in the pH_i 12.5 system than the other three systems prior to the corrosion regime transition, but then dropped to the approximate value of the pH_i 9.5-11.5 experiments during Stage III. Figure 13B shows the activity diagram in terms of logarithm of the $Al(OH)_4^-$ activity against the logarithm of the OH^- activity with speciation data from selected experimental times overlain. The activity diagram was generated with the major species (i.e., *x* and *y* axes), $Al(OH)_4^-$ and OH^-, in the presence of Si and Na ($\log_{10}[SiO_2(aq)]=-2.5$; $\log_{10}[Na^+]=-2.1$—these activities are approximately the measured average activity of Si and Na in the pH_i 12.5 system.) The mononuclear, tetrahedral aluminate ion, $Al(OH)_4^-$, was swapped for the basis aluminum species, Al^{+++}, as it is widely accepted that $Al(OH)_4^-$ is the predominate Al species in alkaline aluminate solutions,[41,42] and the speciation calculations indicated the high concentration of that ion in the leachate solutions. The most notable distinction in Figure 13B (i.e., between the low pH experiments and the pH_i 12.5 system which underwent the Stage III transition) is the speciation of Si under the given solution conditions. The overlaid data for the pH_i 12.5 experiment fell into the $HSiO_3^-$ species field, whereas the rest of the experiments were in the $SiO_2(aq)$ (i.e., orthosilicic acid) field. Although it is likely that the actual pH_i 12.5 solution was populated with oligomers and more complex aluminosilicate molecules,[39,43,44] GWB calculations are limited in analytical scope to the species included in the reference thermodynamic database. However, in terms of the GWB models, there was a clear thermodynamic difference between the two experiments which was apparent from the generation of the activity diagrams. Unfortunately, the much needed information about the solution speciation of Si and Al is plagued by complex overlaps in their nuclear magnetic resonance (NMR) spectra and limited sensitivity in the case of Raman spectroscopy.

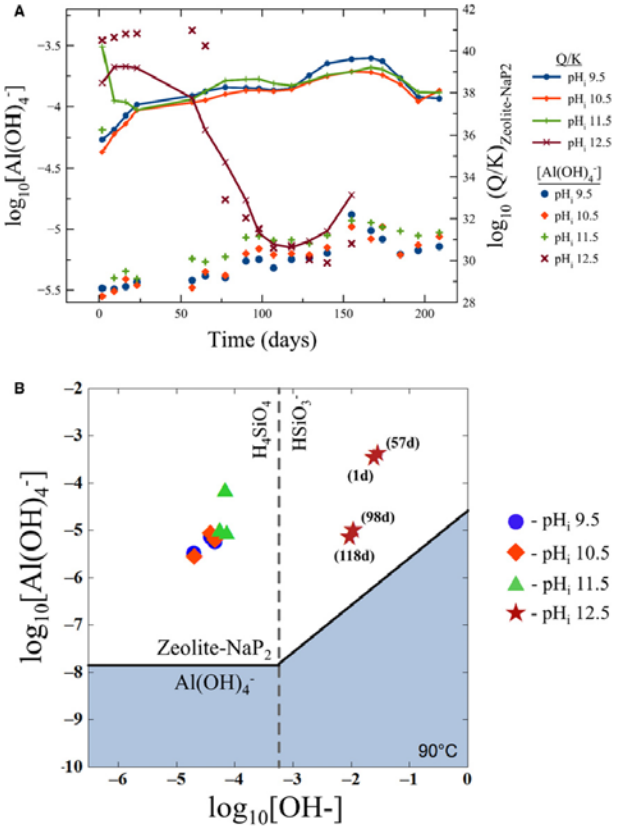

FIGURE 13 (A) The speciation of $Al(OH)^{4-}$ for each starting pH along with the respective $\log_{10}(Q/K)$ values for zeolite NaP2. The single markers represent the activities and the lines represent the calculated SI (the SI values were smoothed on a moving average of 4 to improve the visual quality—the qualitative nature of the trends was not affected by the smoothing process.). (B) An activity diagram showing the speciation of Al vs OH^- concentration with selected experimental times overlaid. A noticeable difference in the Si speciation was observed between the pH_i 12.5 and the pH_i 9.5-11.5 experiments

5 | CONCLUSIONS

It has been shown that the structure of the gel layer that forms during the leaching of ISG glass fibers is a function of pH/[OH^-]. The layers formed at pH 9.5 and 10.5 tend to enrich in Si, and show a nearly fully polymerized structure. The layer formed at pH 12.5 tends to deplete in Si, and this yields a layer structure that is fragmented into chains and rings, presumably bound together by hydrogen bonding of the terminal hydroxyls associated with those chains and rings. The pH 11.5 layer exhibits intermediate behavior tending toward the characteristics of the lower pH experiments. It seems likely that enhanced ionic and water mobility in the fragmented surface layer will facilitate rearrangement of the structure and nucleation of secondary crystalline phases such as zeolite. Similarly, the nucleation of zeolite would be enhanced at the surfaces, both internal to the gel and as observed at the fiber surface, perhaps triggered by the adsorption of Ca and Mg.

These differences in gel-layer structure also correlate qualitatively with the predictions of the model proposed by Jantzen, et al. We observed that just prior to the transition, the pH_i 12.5 system was in a state of $(SB)_{ex}$ and that the resumption of B and Si began immediately after nearly all of the aqueous Al (likely, $Al(OH)_4^-$) was consumed from solution. During the transition, the amount of crystalline phases (principally, Zeolite NaP2) in the system increased to account for at least 40% of the solid volume. We believe that this massive consumption of Al from solution is a unique marker corresponding to the production of large amounts of zeolitic crystalline phases and indicates that a corroding glass system is transitioning from Stage II corrosion to Stage III corrosion. Although the exact mechanism that causes certain corroding glasses to resume alteration has yet to be discerned, this work adds to the growing body of evidence that suggests several of the key factors involved are the pH/[OH^-] of the corroding system in conjunction with the Al/Si ratio in the solution and its

corresponding effect on the composition of the alteration layer. With respect to performance in repository environments, this study demonstrated that the overall corrosion behavior of the glass depends on not just on its bulk composition but also the contacting solution chemistry it generates in response to the local environment.

REFERENCES

1. Wicks G. Nuclear Waste Glasses. In: Tomozawa M, Doremus RH, eds. *Treatise on Materials Science and Technology: Glass IV*. Vol 26 Orlando, FL: Academic Press, Inc.; 1985:57-118.
2. Lutze W, Ewing RC. *Radioactive Waste Forms for the Future*. New York, NY: Elsevier Science Publishing Company, Inc.; 1988.
3. Plodinec MJ. Borosilicate glasses for nuclear waste imobilisation. *Glass Tech*. 2000;41:186-192.
4. Malow G, Lutze W, Ewing RC. Alteration effects and leach rates of basaltic glasses: implications for the long-term stability of nuclear waste form borosilicate glasses. *J Non-Cryst Solids*. 1984;67:305-321.
5. Cunnane JC, Bates JK, Ebert WL, Feng X. High-level nuclear waste borosilicate glass: a compendium of characteristics. *MRS Proc*. 1992;294:225-232.
6. Grambow B. Nuclear waste glasses: how durable? *Elements*. 2006;2:357-364.
7. Jantzen CM, Brown KG, Pickett JB. Durable glass for thousands of years. *Int J Appl Glass Sci*. 2010;1:38-62.
8. Werme L, Bjorner IK, Gerhard B, et al. Chemical corrosion of highly radioactive borosilicate nuclear waste glass under repository conditions. *J Mater Res*. 1990;5:1130-1146.
9. Vernaz EY, Dussossoy JL. Current state of knowledge of nuclear waste glass corrosion mechanisms: the case of R7T7 glass. *Appl Geochem*. 1992;7:13-22.
10. Cailleteau C, Angeli F, Devreux F, et al. Insight into silicate-glass corrosion mechanisms. *Nat Mater*. 2008;7:978-983.
11. Hench LL, Clark DE, Yen-Bower L. Corrosion of glasses and glass-ceramics. *Nucl Waste Chem Management*. 1980;1:59-75.
12. Clark DE, Pantano CG, Hench LL. *Corrosion of Glass*. New York, NY: Magazine for Industry; 1979.
13. Grambow B. Nuclear waste glass dissolution: mechanism, model and application. Report to JSS Project. 1987.
14. Van Isegham P, Aertsens M, Lemmens K, et al. GLAMOR: A critical evaluation of the dissolution mechanisms of high-level waste glasses in conditions of relevance for geological disposal. INIS-FR—3271. 2004. Accessed online: http://www.iaea.org/inis/collection/NCLCollectionStore/_Public/36/038/36038601.pdf?r=1.
15. Fournier M, Gin S, Frugier P. Resumption of nuclear glass alteration: state of the art. *J Nucl Mater*. 2014;448:348-363.
16. Hellman R, Cotte S, Cadel E, et al. Nanometre-scale evidence for interfacial dissolution-reprecipitation control of silicate glass corrosion. *Nat Mater*. 2015;14:307-311.
17. Parruzot B, Jollivet P, Rebiscoul D, Gin S. Long-term alteration of basaltic glass: mechanisms and rates. *Geochim Cosmchim Acta*. 2015;154:28-48.
18. Gin S, Jollivet P, Fournier M, Angeli F, Frugier P, Charpentier T. Origin and consequences of silicate glass passivation by surface layers. *Nat Commun*. 2015;6:1-8.
19. Vienna J, Ryan J, Gin S. Current understanding and remaining challenges in modeling long-term degradation of borosilicate nuclear waste glasses. *Int J Appl Glass Sci*. 2013;4:283-294.
20. Bourcier W. 1998. Affinity functions for modeling glass dissolution rates. Workshop paper. Accessed online: https://e-reports-ext.llnl.gov/pdf/233988.pdf.
21. Gin S. Protective Effect of the Alteration Gel: A Key Mechanism in the Long-Term Behavior of Nuclear Waste Glass. In: *MRS Online Proceedings*. 663. Cambridge University Press; 2000:1-8.
22. Gin S, Jollivet P, Fournier M, et al. The fate of silicon during glass corrosion under alkaline conditions: a mechanistic and kinetic study with the international simple glass. *Geochim Cosmchim Acta*. 2015;151:68-85.
23. Solange R, Gin S. Role of neoformed phases on the mechanisms controlling the resumption of SON68 glass alteration in alkaline media. *J Nucl Mater*. 2004;324:152-164.
24. Gin S, Abdelouas A, Criscenti LJ, et al. An international initiative on long-term behavior of high-level nuclear waste glass. *Mater Today*. 2013;16:243-248.
25. ASTM Standard C1285-14. Standard Test Methods for Determining Chemical Durability of Nuclear, Hazardous, and Mixed waste Glasses and Multiphase Glass Ceramics: The Product Consistency Test (PCT). West Conshohocken, PA: ASTM International; 2014. www.astm.org. Accessed May 16, 2017.
26. Jantzen CM, Pickett JB, Brown KG, Edwards TB, Beam DC. Process/product models for the defense waste processing facility (DWPF): Part I. Predicting glass durability from composition using thermodynamic hydration energy reaction model (THERMO). US Department of Energy Report. 1995. WSRC-TR-93-672.
27. Jantzen CM, Trivelpiece CL, Crawford CL, Pareizs JM, Pickett JB. Accelerated leach testing of glass (ALTGLASS): I. Informatics approach to high level waste glass gel formation and aging.. *Int J Appl Glass Sci* 2017;8:69-83.
28. Jantzen CM, Trivelpiece CL, Crawford CL, Pareizs JM, Pickett JB. Accelerated leach testing of glass (ALTGLASS): II. Mineralization of hydrogels by leachate strong bases. *Int. J. App. Glass Sci*. 2017;8:84-96.
29. Fournier M, Frugier P, Gin S. Resumption of alteration at high temperature and pH: rates measurements and comparison with initial rates. *Proc Mater Sci*. 2014;7:202-208.
30. Ribet S, Gin S. Role of neoformed phases on the mechanisms controlling the resumption of SON68 glass alteration in alkaline media. *J Nucl Mater*. 2004;324:152-164.
31. Frugier P, Gin S, Lartigue JE, Deloule E. SON68 Glass Dissolution Kinetics at High Reaction Progress: Mechanisms Accounting For The Residual Alteration Rate. In: *MRS Online Proceedings*. Vol 932. Cambridge University Press. 2006;94.1-94.8.
32. Ryan JV, Ebert WL, Icenhower JP, Schreiber DK, Strachan DM, Vienna JD. *Joint EM-NE Study of Glass Behavior Over Geologic Time Scales*. Pacific Northwest National Laboratory (PNNL): Richland, WA; 2012. PNNL-SA-84912.
33. Jansen JC. The Preparation of Molecular Sieves. In: Bekkum H, Flanigen EM, Jansen JC, eds. *Introduction to Zeolite Science and Practice*. Amsterdam: Elsevier; 1991:77-136.
34. Kingery WD, Bowen HK, Uhlmann DR. *Introduction to ceramics*. New York: Jhon Willey & Sons; 1976.

35. Condradt R. Chemical structure, medium range order and crystalline reference state of multicomponent oxide liquids and glasses. *J Non-Cryst Solids*. 2004;345:16-23.
36. Cundy CS, Cox PA. The hydrothermal synthesis of zeolites: precursors, intermediates and reaction mechanism. *Microporous Mesoporous Mater*. 2005;82:1-78.
37. Huo Z, Xu X, Lu Z, et al. Synthesis of zeolite NaP with controllable morphologies. *Microporous Mesoporous Mater*. 2012;158:137-140.
38. Hansen S, Hakansson U, Landa-Canovas AR, Falth L. On the crystal chemistry of NaP zeolites. *Zeolites*. 1993;13:276-280.
39. Albert BR, Cheetham AK, Stuart JA, Adams CJ. Investigations on P zeolites: synthesis, characterization, and structure of highly crystalline low silica NaP. *Microporous Mesoporous Mater*. 1998;21:133-142.
40. Lechert H. Possibilities and limitations of the prediction of the Si/Al ratios of zeolites from the batch composition. *Microporous Mesoporous Mater*. 2000;40:181-196.
41. Yu J. Synthesis of Zeolites. In: Cejka J, Bekkum H, Corma F, Schueth F, eds. *Introduction to Zeolite Molecular Sieves*. Amsterdam: Elsevier; 2007:39-103.
42. Sipos P. The structure of Al(III) in strongly alkaline aluminate solution—a review. *J Mol Liq*. 2009;146:1-14.
43. Swaddle TW. Silicate complexes of aluminum (III) in aqueous systems. *Coord Chem Rev*. 2001;219:665-686.
44. Kinrade SD, Swaddle TW. Silicon-29 NMR studies of aqueous silicate solutions. 1. Chemical shifts and equilibria. *Inorg Chem*. 1988;27:4253-4259.
45. Sjoberg S. Silica in aqueous environments. *J Non-Cryst Solids*. 1996;196:51-57.

How to cite this article: Trivelpiece CL, Rice JA, Clark NL, Kabius B, Jantzen CM, Pantano CG. Corrosion of ISG fibers in alkaline solutions. *J Am Ceram Soc*. 2017;00:1–15. https://doi.org/10.1111/jace.14950

SECTION 4. CORROSION BEHAVIOR OF SON68-AFCI BLENDS: COMPOSITION EFFECTS ON STAGE III DISSOLUTION

JARRET A RICE, CORY L TRIVELPIECE, AND CARLO G PANTANO

1.0 Introduction

Using a series of glass compositions synthesized by blending and re-melting SON68 and AFCI (100%SON, 75%SON/25%AFCI, 50%SON/50%AFCI, 25%SON/75%AFCI, AFCI), this study describes experimental procedures and results intended to improve our understanding of glass composition effects in the Stage II to Stage III transition. To help explain when and what drives the glass corrosion transition to Stage III, solution data is modeled for evaluation against accelerated leach testing (ALTGLASS) database.

The ALTGLASS database focuses attention on the evolution of solution pH and its excess acidity or basicity (expressed as a molar concentration of weak acid (WA) or strong base (SB)). It proposes that the resumption of dissolution (Stage III) is expected for glasses whose residual/equilibrium pH exceeds 10.7, along with excess strong base.

The solution results obtained in this study show a non-linear effect of the two unblended end-point compositions (AFCI and SON68) on the behavior of the blends. Compared to pure SON68 solution analysis, the normalized losses for boron, sodium and silicon drop significantly with the addition of 25% AFCI in SON68. Although the normalized losses for aluminum are low for all compositions (consistent with the behavior of aluminum, in general, for AFCI and SON68), the time dependence is quite different. The aluminum release for SON68 initially decreases with time, while the release of aluminum remains constant for the 75%SON/25%AFCI blend. The remaining three glasses all show a comparable increase in aluminum release with time. This data suggests that amongst these five systematically varied glass compositions, the aluminum behavior changes dramatically in mixtures of SON68 and AFCI.

Based on the initial data, it was hypothesized that there may be a critical constituent in AFCI that promotes Stage III through its effect on pH, or its creation of solution or gel complexes that promote nucleation of crystals. After ~two years, however, none of the five nominal glass-composition samples tested at SA/V=2,000 m^{-1} have transitioned to Stage III on their own. For this reason, the pH of a set of these samples was artificially increased to pH 11.5 with the intent of prompting a Stage III event. In this environment, the resistance to or accelerated evolution of a Stage III event could be tracked and the resulting secondary phases studied. In two additional sample sets, using compositions with ~2.5 ^{w}/o excess Al_2O_3, the three blended samples tested at an SA/V of 25,000 m^{-1}, were the only samples which exhibited the transition to Stage III within the three-year period of this study. Moreover, the solution concentration of Al at the onset of the transition, when the Al concentration reaches a maximum, was between 50 and 60 ppm for all three compositions. Unfortunately, the identification of a critical constituent or reaction product that triggers the transition could not be identified amongst the 20 common and 16 different oxides which constitute SON68 and AFCI.

Based on the Master's Thesis of Jarret A. Rice, Penn State University, 2016.

2.0 Experimental Procedures

2.1. Glass Processing:

Pure SON68 and AFCI glass, the end point compositions, were processed as dry chemical oxides and melted in a 90% platinum-10% rhodium (Pt-Rh) crucible. The appropriate mass of each dry chemical was calculated from the composition listed in Appendix A to produce 400 grams of both glasses. Each weighed chemical for the two glasses was added to separate 1-gallon bags and hand mixed for ~5 minutes before being mixed in an agate mill for 3 minutes.

After mixing, the glasses were separately melted in a Pt-Rh crucible with a Pt-Rh lid placed over the top of the crucible to limit the escape of volatile elements. AFCI was melted at 1350°C for 1 hour before the glass was poured and cooled. The glass was then crushed, mixed, and melted a second time at 1350°C. After the second melting, the AFCI glass was poured into preheated graphite molds and transferred to an annealing oven at 520°C (temperatures determined from DSC, see Appendix B). The AFCI glass bars were held at 520°C for 2.5 hours before cooling to room temperature at 1°C min^{-1}.

Before the SON68 glass batch was melted, the crucible and lid were cleaned in a hydrofluoric acid bath. The same melt procedure was performed for SON68 but at a slightly lower melting temperature of 1320°C. Likewise, after the second melt, SON68 was poured into the graphite molds and transferred to an annealing oven at 532°C to soak for 1 hour before cooling to room temperature at 1°C min^{-1}.

From the pure SON68 and AFCI glass, the three blended glass compositions were made by combining SON68 and AFCI glass in the appropriate mass ratios; as follows: 75% SON68 to 25% AFCI, 50% SON68 to 50% AFCI, and 25% SON68 to 75% AFCI (see Appendix A for the expected composition). For simplicity, the labels of the glass blends are referred to as S_100, for pure SON68, S_75, S_50, S_25, and A_100 for pure AFCI.

Each blend was melted twice in a Pt-Rh crucible with a pour, crush, and re-mix step before the second melt. After the second melting, each glass was annealed for 2 hours and cooled to room temperature at 1°C min^{-1}. The S_75 blend was melted at 1305°C, poured and annealed at 525°C; the S_50 blend was melted at 1315°C and annealed at 525°C; and S_25 was melted at 1320°C and annealed at 528°C. The compositions of these glasses correspond to the *calculated* compositions in Appendix A.

2.2. Product Consistency Test

The glass compositions described above were subjected to a modified PCT Test Method B [1, 2] corrosion test. A list of requirements for the ASTM standard PCT Test Method B and the changes that were made for this PCT type test performed can be found in Table 1.

Glass powder was used and processed according to the standard. Each glass composition was separately crushed in a tungsten carbide mill and sieved to the specified -100+200 mesh (149-75 µm) particle size. Glass powders were rinsed in an ultrasonic bath with ASTM Type 1 water until the decanted solution was no longer cloudy and glass fines had been removed. A final rinse with ethanol was done before the powders were dried in a 90°C oven for 24 hours.

Table 1. List of standard PCT-B requirements and the modified test method used in this experiment.

	PCT Test Method B	Modified Test Method
Type of waste form	Radioactive Mixed Simulated	Simulated radioactive waste glass
Usage	Scoping tests, Crystallization Studies, comparative waste form evaluation	Scoping tests, Crystallization Studies, comparative waste form evaluation
Test Vessel	Unsensitized Type 304L stainless steel or PFA TFE-fluorocarbon vessels	PFA-fluorocarbon digestion vessels
Leachant	ASTM Type 1 water or other solutions	ASTM Type 1 water
Test Duration	7 days ±2% or varying times	Varying times
Minimum Sample Mass	≥1 gram	≥1 gram
Particle Size	US Standard ASTM - 100 to + 200 mesh (0.149 to 0.074 mm)	US Standard ASTM - 100 to + 200 mesh (0.149 to 0.074 mm)
Temperature	90°C ± 2°C or other temperatures, provided that any observed changes in reaction mechanism are noted	90°C ± 2°C
Atmosphere	Air or CO_2 free air	Air
Type of System	Open to transport in PFA TFE-florocarbon; Closed to transport in stainless steel	Open to transport in PFA-fluorocarbon digestion vessels

The mass of each glass powder added to the test vessels was determined by setting a fixed total surface area of glass to solution volume (S/V) at 2000 m^{-1}. With a known volume from the 120 mL perfluoroalkyl (PFA) digestion vessels (Savillex®), the geometric surface areas of the sieved glass powders were calculated for each glass using Equation 1, where the diameter (D) is the average diameter of the particles, and density (ρ) that was measured with a helium pycnometer (Micrometrics AccuPyc II 1340).

$$SA_{geom} = \frac{6}{\rho \cdot D} \ [m^2/g] \qquad \text{Equation 1}$$

With a fixed solution volume of 120 mL, geometric surface area of ~196-203 cm^2/g, and S/V ratio of 2000 m^{-1}, the mass of glass required for each composition could be calculated as presented in Table 2.

Table 2. The measured density and required mass of glass powder to achieve an S/V ratio of 2000 m^{-1} for the nominal series of blends

Glass	Density [g/cm3]	Geom. SA [cm2/g]	Solution Vol. [cm3]	Mass Glass [g]
SON-68	2.736	195.8	120	12.26
S75:A25	2.718	197.1	120	12.18
S50:A50	2.693	199.0	120	12.06
S25:A75	2.662	201.2	120	11.93
AFCI	2.635	203.3	120	11.80

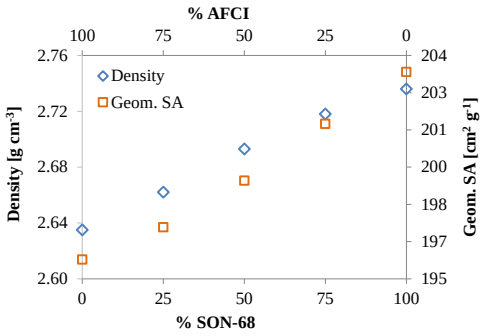

The appropriate mass of powder for each glass was transferred to a 120 mL PFA-reaction vessel and 120 mL of ASTM Type 1 water, measured with a graduated cylinder, was added to each vessel. With lids tightly secured, all vessels were placed in a forced convection oven at constant 90°C.

At the same time, identical duplicates of each experiment were made and placed in the oven with the PCT-original vessels. Referred to as PCT-ghost samples, these duplicates were used to replenish solution that was removed from the PCT-original vessels for solution analysis.

It is not uncommon to remove solution for analysis and replenish with fresh solution. In some cases, the entire volume of solution is replaced multiple times throughout the duration of an experiment. Tests like the International Organization for Standardization (ISO), the American Nuclear Society test ANS 16.1, Dynamic Leach Test (DLT) and the Accelerated Leach Test (ALT), both variations of the ANS 16.1 test, require the total solution volume of leachate to be exchanged daily, weekly, or yearly [3, 4, 5].
If too much solution is removed and replaced too often, reaction products will not accumulate in solution, and the solution speciation and its effect on corrosion can be influenced. However, if only a small amount of solution is removed infrequently, the solution will be able to reach saturation. The rates may slow with each removal of solution, but they approach saturation again shortly thereafter.

At every sampling interval, 5 mL were removed; 2 mL of the 5 mL was used for pH measurement and the remaining 3 mL for inductively coupled plasma-atomic emission spectroscopy (ICP-AES) analysis. To minimize the effects of each solution extraction, the 5 mL removed was replenished with 5 mL from the PCT-ghost samples.

At the beginning of the test, the ghost sample solution was monitored to ensure the PCT vessels were not being spiked with higher concentrated solution. For this reason, an additional 2 mL solution was removed from the ghost samples for ICP analysis. The total 7 mL removed from ghost-PCT samples was replenished with 7 mL of ASTM Type 1 water. A schematic detailing the steps taken for each solution withdrawal is shown in Figure 1.

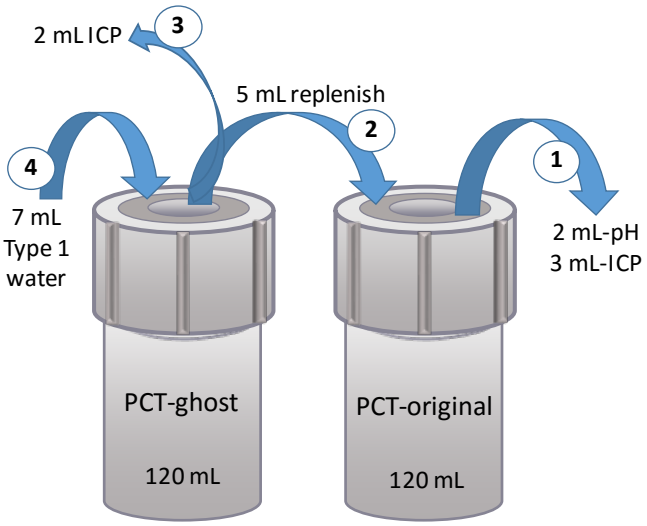

Figure 2.The schematic shows the steps and amounts of solution withdrawn from the PCT experiments for sampling.

2.2.1. Product Consistency Test-Duplicate pH Spike

After 253 days of using the PCT-ghost samples for solution replenishment of PCT-original samples, the pH of each PCT-ghost sample was increased to pH 11.5 by adding small amounts of 10 mol L^{-1} KOH solution. It was intended that higher pH conditions would facilitate the rapid dissolution of glass, thereby providing enough species in solution to drive a Stage III transition and precipitation of amorphous and crystalline phases [6].

The 10 mol L^{-1} KOH spiking solution was prepared by adding 56.1064 g of KOH (J.T. Baker Lot#X44911) to 100 mL ASTM Type 1 water in a beaker and continually stirred with a magnetic stir bar. Small amounts were added to raise the pH incrementally. After every amount of concentrated KOH solution was added to a vessel, a Nalgene rod was used to mix solution in the reaction vessel before pH was measured.

Once the pH of each vessel had been brought to pH ~11.5 they were returned to the 90°C oven. After spiking, the PCT-ghost samples were not used to replenish PCT-original solution; instead, solution that was removed for analysis from both PCT-original and PCT-ghost was replenished with ASTM Type 1 water.

In this same manner, 124 days post $pH_{90°C}$ 11.5 spiking when 377 days had elapsed, the solution pH was increased again up to $pH_{90°C}$ 12.0 with 10 mol L^{-1} KOH solution

2.3. Analysis Methods

Both sets of PCT samples were sampled periodically for solution analysis. Solutions for ICP analysis were stored in snap cap vials (Bel-Art Products; 7-dram) in a refrigerator before analysis. Solution pH was measured after the solutions had cooled to room temperature.

The results from ICP analysis were compared between all glass compositions as normalized elemental mass loss in g m^{-2} (NL); the relevant calculation is shown in Equation 2, where c_i is the concentration reported by the ICP-analysis, (S/V) is the ratio of geometric surface-area-to-solution-volume, and f_i is the fractional amount of each element, calculated from the composition.

$$NL(i) = \frac{c_i(sample)}{f_i \cdot (SA/V)} \left\{\frac{g}{m^2}\right\} \qquad \text{Equation 2}$$

According to the ALTGLASS approach proposed by Jantzen et al. [6], the pH of the leachate solution is influenced by the presence and interaction of strong bases and weak acids. From the measured concentration data, the excess strong base [SB] and weak acid [WA] in solution were calculated according to the expression shown in Equation 3. The strong base is calculated from the concentration of sodium, lithium, and calcium, and the weak acid formation in solution is taken from the concentration values of aluminum, silicon, and boron.

$$[SB] - [WA] = \left(\frac{C_{Na}}{m_{Na}} + \frac{C_{Ca}}{m_{Ca}} + \frac{C_{Li}}{m_{Li}}\right) - \left(\frac{C_{Si}}{m_{Si}} + \frac{C_B}{m_B} + \frac{C_{Al}}{m_{Al}}\right) \left\{\frac{mmol}{L}\right\} \qquad \text{Equation 3}$$

In the equation, C_i is the concentration of element "i" in solution as ppm, and m_i is the molar mass of element "i" in solution.

3.0 Results

3.1. Product Consistency Test Solution Analysis

At each sampling interval, the ~2 mL of solution for pH measurement was cooled from 90°C to room temperature by forced air convection. The measured pH for all five experiments is shown in Figure *2*. This data indicates a linear dependence of pH on composition, where pure AFCI has the highest solution pH and decreases with increasing SON68 content.

Starting with SON68, the percent increase in solution pH for each glass is nearly identical to the percentage of AFCI that was added to the respective glass. For S_75, the blend with 25%AFCI, the pH increases 21% from S_100, 53% increase for S_50, and 78% for S_25 with a 75% addition of AFCI.

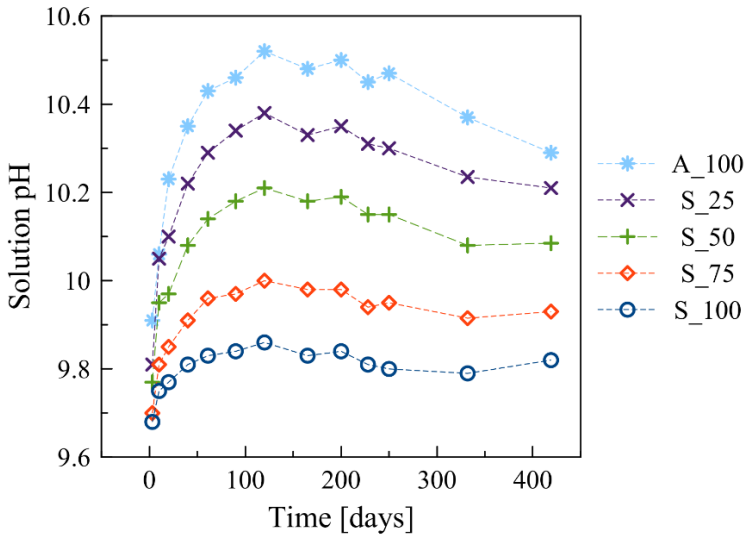

Figure 3. Time dependent room temperature solution pH for SON68, AFCI, and their three blends.

The trends in the normalized loss data in Figure 3 significantly differ from the solution pH trends. In contrast to the pH data, the normalized losses are non-linear with respect to the composition changes. Pure SON68 exhibits the highest losses for silicon, sodium, and boron in solution. However, it should be noted that the substitution of only 25% AFCI in SON68 (S_75) changes the losses by significant amounts (i.e. increasing or decreasing by 40-60%). The substitution of 50% and more so for 75% substitution of AFCI to SON68, brings the behavior of sodium and silicon in those blends to be almost coincident with pure AFCI. The slight dip in boron for all glass compositions between 100-200 days can be attributed to imprecise ICP-AES calibration and is not a momentous event.

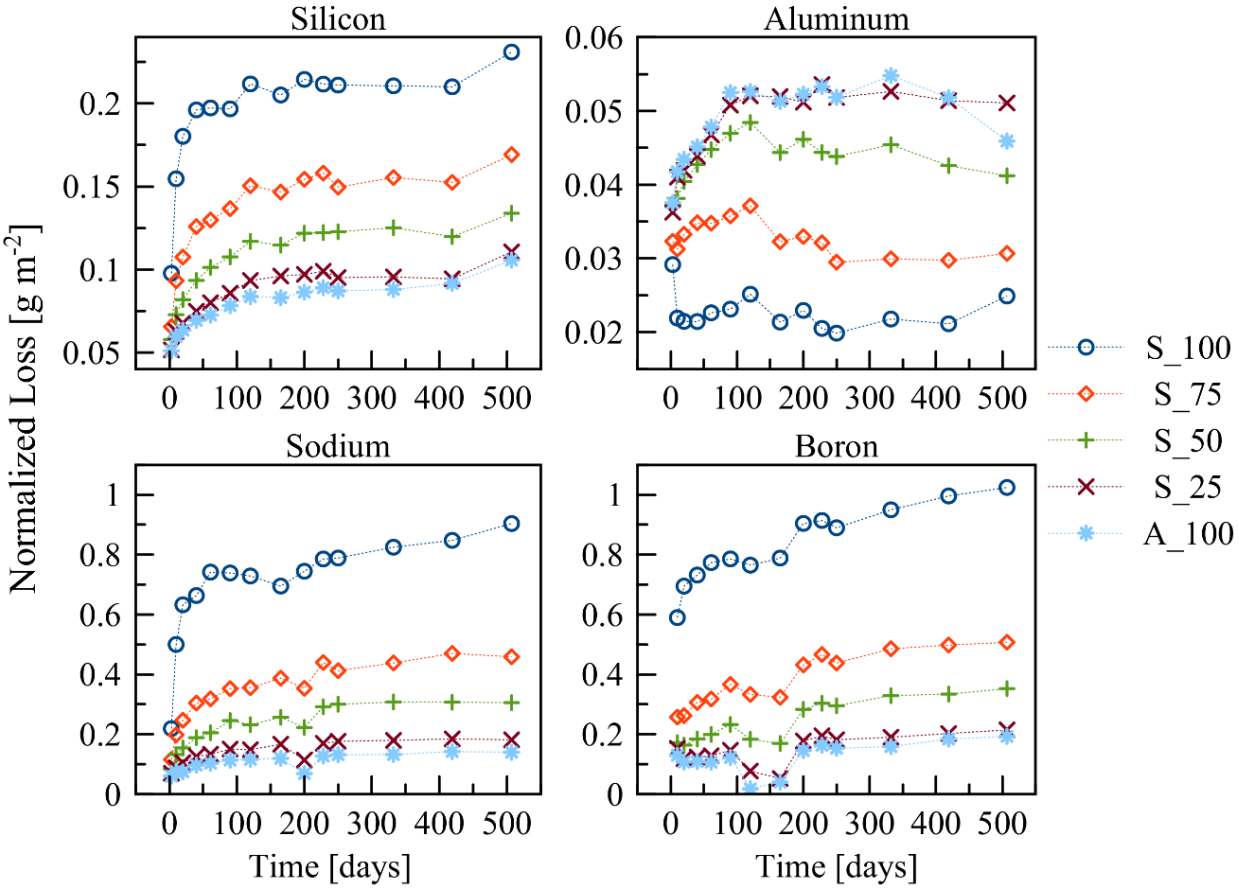

Figure 4. Normalized loss of elements Si, Al, Na and B after 500 days for the PCT-original solution data.

This non-uniform distribution is interesting considering that each blend is a direct percent combination of pure SON68 and AFCI; ie, the resulting solution data could be expected to behave more like the pH, with uniform distribution with equal increases/decreases dependent on the percentage of the glasses combined. From an inductively coupled plasma lithium-metaborate fusion analysis of all five glasses used in the PCT experiment, the composition progression from one endpoint (SON68/AFCI) to the next follows in accordance with the calculated results in Table 3. While Al_2O_3, Na_2O, and SiO_2 are all present in SON68 and AFCI in relatively high amounts, Fe_2O_3 is a component specific to SON68 and shows just how well the blends are scaled according to the percentage of SON68 and AFCI added.

Table 3. The weight percentages for selected components in the blended glasses measured with ICP-AES.

Glasses used for Product Consistency Tests						
Glass		S_100	S_75	S_50	S_25	A_100
Al_2O_3 wt%	Calculated	5.00	6.10	7.19	8.29	9.39
	Meassured	5.28	6.50	7.58	8.67	9.48
*Fe_2O_3 wt%	Calculated	3.03	2.27	1.52	0.76	0.00
	Meassured	3.03	2.29	1.51	0.74	0.00
Na_2O wt%	Calculated	10.2	9.4	8.6	7.8	7.0
	Meassured	10.1	9.2	8.5	7.8	6.9
SiO_2 wt%	Calculated	45.9	47.8	49.8	51.8	53.7
	Meassured	46.3	48.7	50.4	52.1	53.2

Along with the distribution differences based on the amount of AFCI in composition, the correlation between aluminum in solution and its effect on other elements is significant. For compositions A_100 and S_25 with the highest NL(Al), all other elements are at a minimum and less than all other compositions. Conversely, S_100 with the lowest NL(Al) experiences the highest NL for all other elements.

Based on the amount of excess strong base versus weak acid in solution, Jantzen et al. developed a more analytical approach for analyzing solution data and the likelihood of a Stage III transition [7]. The pH of the leachate solution is influenced by the presence and interaction of strong bases and weak acids. From solution analysis, the strong base [SB] is calculated from the concentration of sodium, lithium, and calcium; and weak acid [WA] formation in solution is taken from the concentration values of aluminum, silicon, and boron (Equation 3).

Plotting the calculated [SB]-[WA] versus solution pH for each of the compositions in this PCT-experiment, Figure 4 displays a clear trend. Each composition shows tightly grouped values throughout the duration of the experiment, from day 1 to day 332. Pure AFCI and S_25 are both predominantly in the excess strong base region, S_50 fluctuates between strong base and weak acid, and S_75 and pure SON68 remain well within the excess weak acid region.

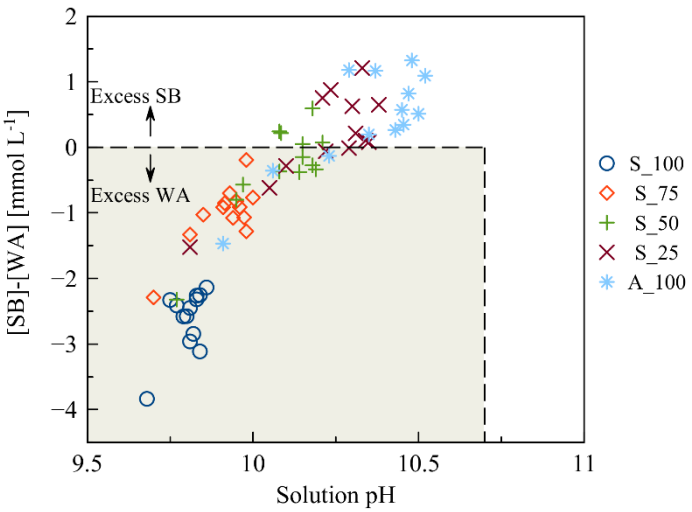

Figure 5. A trend exists for all five glasses based on the [SB]-[WA] plot. S_100 maintains the lowest pH and highest amount of excess weak acid. A_100 yields highest pH and excess strong base.

The basis of the [SB]-[WA] plots is the understanding that glasses in the excess strong base region (> 0) and higher pH > 10.7, have the necessary pH conditions and excess quantities of silicon and aluminum necessary for zeolite formation to occur, thus prompting a Stage III transition. However, none of the glasses are beyond the predicted pH 10.7 [8] required for a Stage III transition. And based on the normalized loss data of silicon, aluminum, boron, and sodium, there has been no momentous increase or decrease of glass species in solution to suggest a resumption of alteration.

1.1. Concentrated Glass Solution Analysis

Although the ASTM standard Product Consistency Tests have not revealed a tipping point or transition into Stage III to date, a comparable set of blended glasses revealed more clearly the effects of AFCI, Al and SA/V when tested as Concentrated Glass Solutions (CGS).

Much like the ASTM-PCT standard test, the CGS experiment was performed with glass powder that was reacted in PFA digestion vessels with ASTM-Type 1 water at 90°C while solution was removed and replenished at various sampling intervals. Unlike the PCT-original samples, the glass powders for CGS samples was not sieved to a specific particle size and ranged from fines of <5 µm to large particles of ~500 µm in diameter. The PFA digestion vessels used were 500 mL instead of the PCT 120 mL, and SA/V was set at 25,000 m^{-1} for CGS, not the 2,000 m^{-1} used for PCT. Recall that for the PCT Test Method B, the surface area to volume is a parameter that can be varied.
The CGS solution pH for each sample collected was measured at room temperature shortly after collection, the data for which is shown in Figure 5. The same pH probe used for the PCT-original and ghost solutions was used for the CGS solutions.

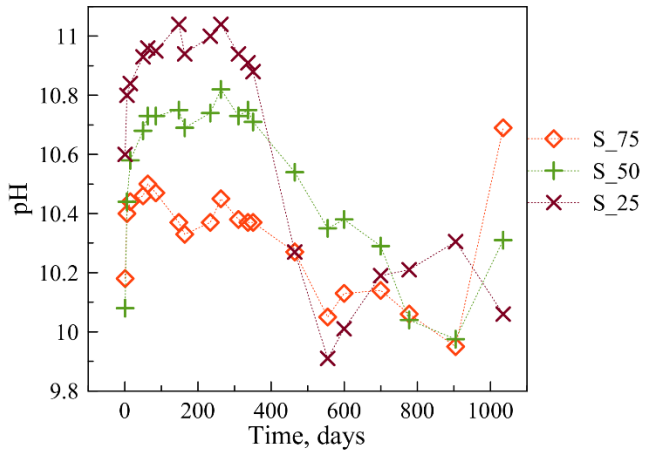

Figure 6. Room temperature solution pH for each blends glass from the Concentrated Glass Solution samples

For the three SON68/AFCI blends, the solution pH is more scattered than the PCT solution pH results. The quasi-equilibrium pH during the first couple hundred days is also about one-half pH unit higher than the quasi-equilibrium PCT pH's (Figure 2). The effect of surface area to volume on pH has been observed by others, and in general, higher S/V ratios produces higher solution pH [9, 2, 10]. With SA/V 12.5x greater for CGS than PCT, this is certainly an explanation for the observed pH difference between the two experiments. For all three blends and pure AFCI (not shown), the solution pH drops semi-gradually around 400 days. The most significant of these is S_25, which drops approximately one whole pH unit over the course of ~100 days. The decline in pH for S_50 begins very near the same time as S_25, but lasts for nearly 400 days and drops pH ~0.7 unit. The decrease in pH for S_75 is much more irregular and not quite as dramatic as the other two glasses, but nonetheless apparent.

Although the solution pH data in Figure 5 is scattered and irregular compared to that of the PCT solution pH data, the time at which events occur for each glass are mimicked by events observed with the normalized loss solution data in Figure 6. In the case of S_25, the dramatic drop in pH just before 400 days occurs when aluminum has reached a maximum. After this peak in release of aluminum from the S_25 glass, the aluminum in solution plummets. At ~650 days, aluminum reaches a minimum, the same time the pH hits a minimum, and a rapid resumption of silicon, sodium, and boron occurs.

For S_50, the increase in aluminum concentration begins to occur just before 500 days elapsed time. Similar to S_25, the S_50 aluminum climbs to a maximum and then plummets quickly thereafter. The drop in aluminum concentration occurs around 775 days, the same time the pH of S_50 reaches the minimum. Subsequently the concentration of the other elements begins to increase.

Just after 600 days elapsed time, the aluminum concentration for S_75 glass increases. The time of this event is offset from the initial time that S_75 pH begins to decrease. The solution pH hits a minimum at 905 days elapsed time, identical to the peak in aluminum concentration.

The specific days, respective solution pH, and maximum aluminum concentration, in ppm, just before aluminum in solution plummeted, is displayed in Table 4. Note that the **maximum aluminum concentration during the transition for each glass during the transition is between 50 and 57 ppm**.

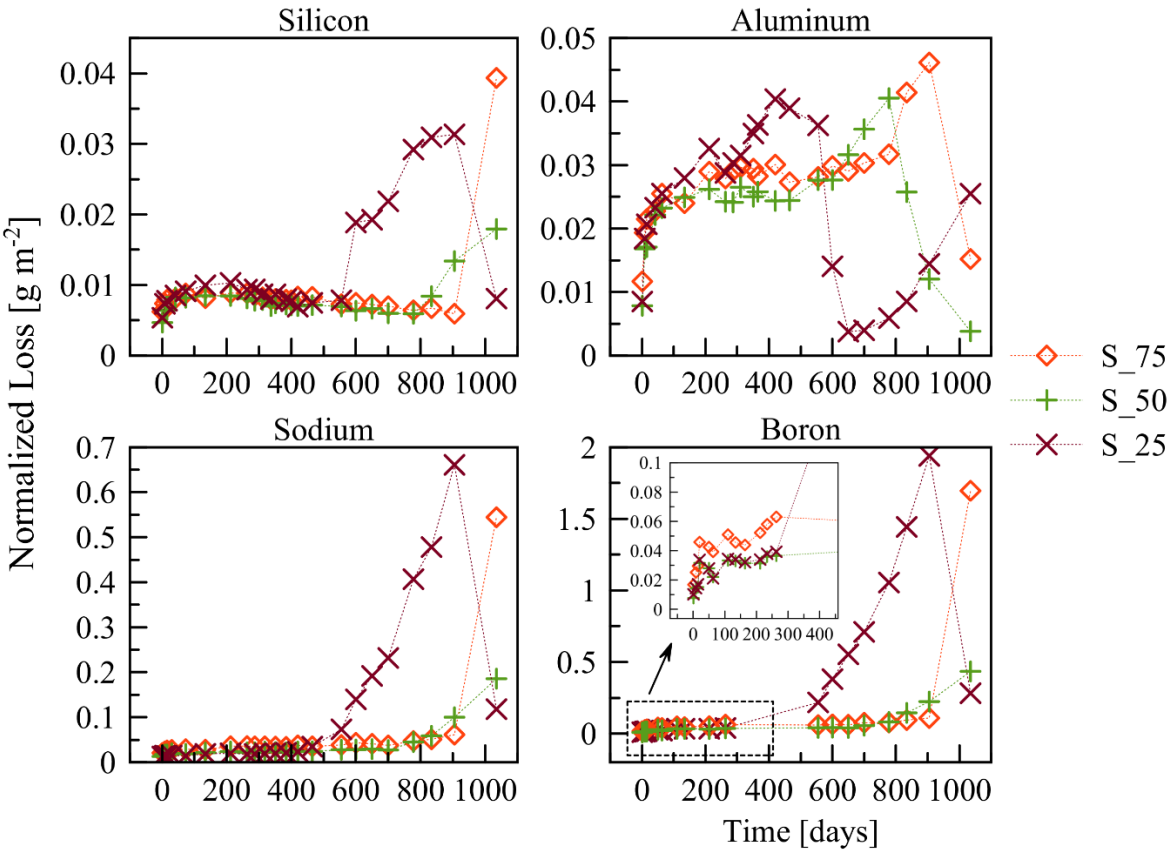

Figure 7. The normalized loss data for the three CGS blended glasses which transition to Stage III.

It is also worth noting that during the first 200 days of corrosion, the silicon concentrations reached a plateau while the aluminum concentration continued to increase. And when the aluminum concentration began to increase suddenly, the silicon concentrations began slowly decreasing.

The events that occur for all three blends in the CGS experiment are distinctive and very different features from the PCT experimental data that cannot be explained solely by the difference in SA/V. Moreover, there appears to be a systematic order in the onset of the transition. This is discussed further in the discussion section.

Table 4. All three CGS glass blends reach a maximum aluminum concentration at different (but systematic) elapsed times, listed below with the max concentration of aluminum just before the drops occurred.

Glass	Time (days)	pH	Max Al (ppm)
S_25	420	10.5	57.0
S_50	778	10.0	50.2
S_75	905	10.3	53.1

The total amount of strong base and weak acid was calculated (Equation 3) for the CGS solution data and plotted versus solution pH in Figure 7. From days 1 to 300, the S_75 glass is predominantly in the

neutral buffered region with equal parts strong base to weak acid while both S_50 and S_25, even more so, are in the excess strong base region with S_25 above the critical pH 10.7 for a possible Stage III event to occur. It may be recalled that the Al concentration reached a maximum for each of these glasses between 420 and 905 days (Table 4), with subsequent spikes in other elements. This correlates with the [SB]-[WA] plot from 318-1035 days showing a partial shift for all glasses into the weak acid region below pH 10.7.

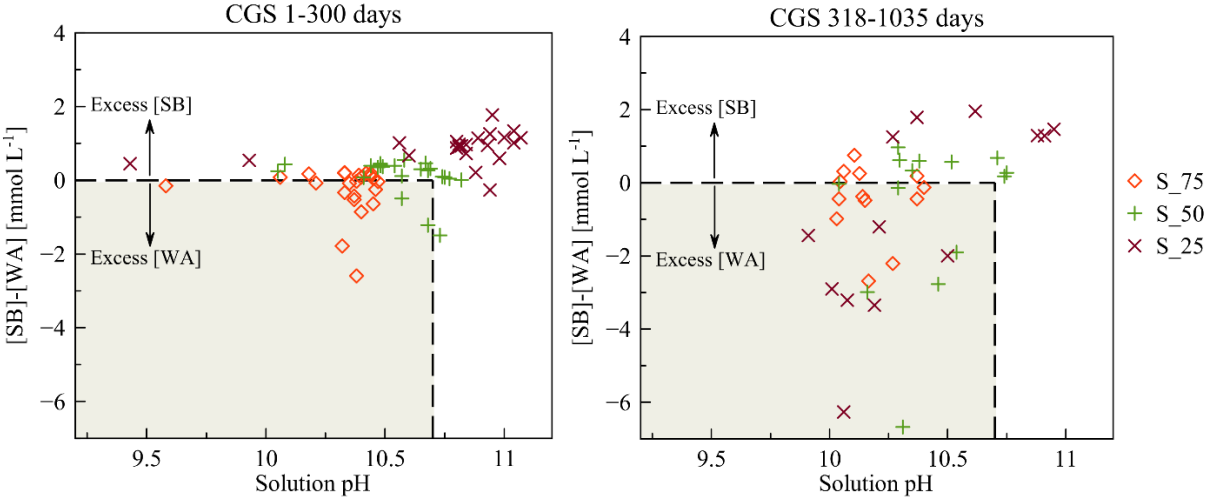

Figure 8. During days 1-300, high pH and excess strong base dominate for the S_25 and S_50 glass. Between 318-1035 days the amount of weak acid increases and lower pH's prevail for all glasses.

As proposed by Jantzen et al. [6], the reacted glass with its contacting solution high in strong base and a solution pH at or above pH 10.7 is likely to transition to Stage III corrosion. These data are consistent, with the added observation that the maximums in pH rank with the time to transition; ie, S_25 experienced the first Stage III transition and was followed by S_50 and lastly S_75.

3.2. Spiking the pH in the PCT Samples

After 253 days with no indication of a Stage III event for the PCT-original solutions, the solution pH of the duplicate "ghost" PCT samples was increased to $pH_{90°C}$ 11.5 to promote a Stage III transition. The solution pH was artificially increased by adding small amounts of concentrated 10 M KOH solution to each sample. In addition, 124 days post $pH_{90°C}$ 11.5 spiking and 377 days total elapsed time, the solution pH was increased again up to $pH_{90°C}$ 12.0.

Prior to increasing the pH of the PCT-ghost samples, the graph inset in Figure 8 shows that the solution pH was ordered the same as PCT-original solution pH (Figure 2), but ~0.1-0.3 pH units lower. The lower pH values for the PCT-ghost samples is understandable because the solution removed was replenished with fresh water.

Subsequent to the first spike, an immediate increase in pH occurred with all pH values tracking closely with one another beyond 250 days. But unlike the solution pH of the PCT-original samples, the distribution was flipped, with S_100 remaining at a higher pH and A_100 the lowest. Likewise, for the second spike after 377 days, the solution pH values are closely grouped, but shortly after, the pH of A_100 diverges from the other four glasses and decreases. The pH values shown in Figure 8 are all greater than the target values (11.5 and 12.0 at 90C) because the solution pH was measured at room temperature and not at 90°C.

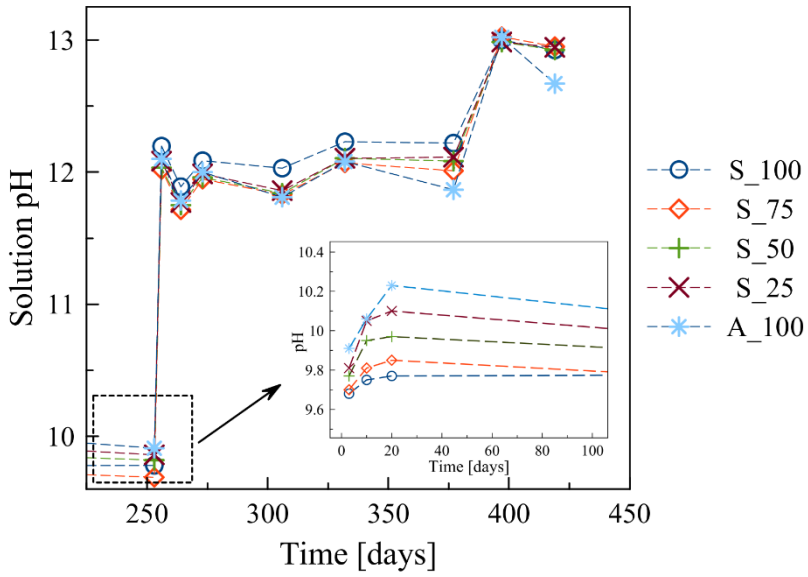

Figure 9. Measured room temperature solution pH for the spiked PCT-ghost samples

Prior to spiking, the solution concentrations were measured with ICP-AES for the first 25 days, and then again just before the concentrated KOH solution was added to the PCT-ghost samples. Because of the replenishment with water, and depending on the element, the concentration values are 1-4 ppm lower than the respective PCT-original element concentration. Nevertheless, the initial solution data distribution directly matched the solution data for the PCT-original experiments (Figure 3).

Naturally, after the increase to pH 11.5, the concentration of each element analyzed, silicon, aluminum, boron, and sodium, all increase (Figure 9). Prior to spiking, the aluminum concentration distribution based was ordered with A_100 showing the highest concentration and S_100 the lowest value. After spiking, however, the normalized loss levels of aluminum in solution were all within 0.5 g m^{-2} of one another. After ~20 days, the S_100 aluminum concentration quickly drops, holding just above S_75. And after ~50 days, A_100 aluminum concentration plummets, followed shortly by a rapid increase in silicon, boron, and sodium concentrations. The increase in concentrations for A_100 is only increased with the next spike of KOH solution to pH 12.0 at 377 days. In addition, the spike to pH 12.0 increases aluminum concentration as well.

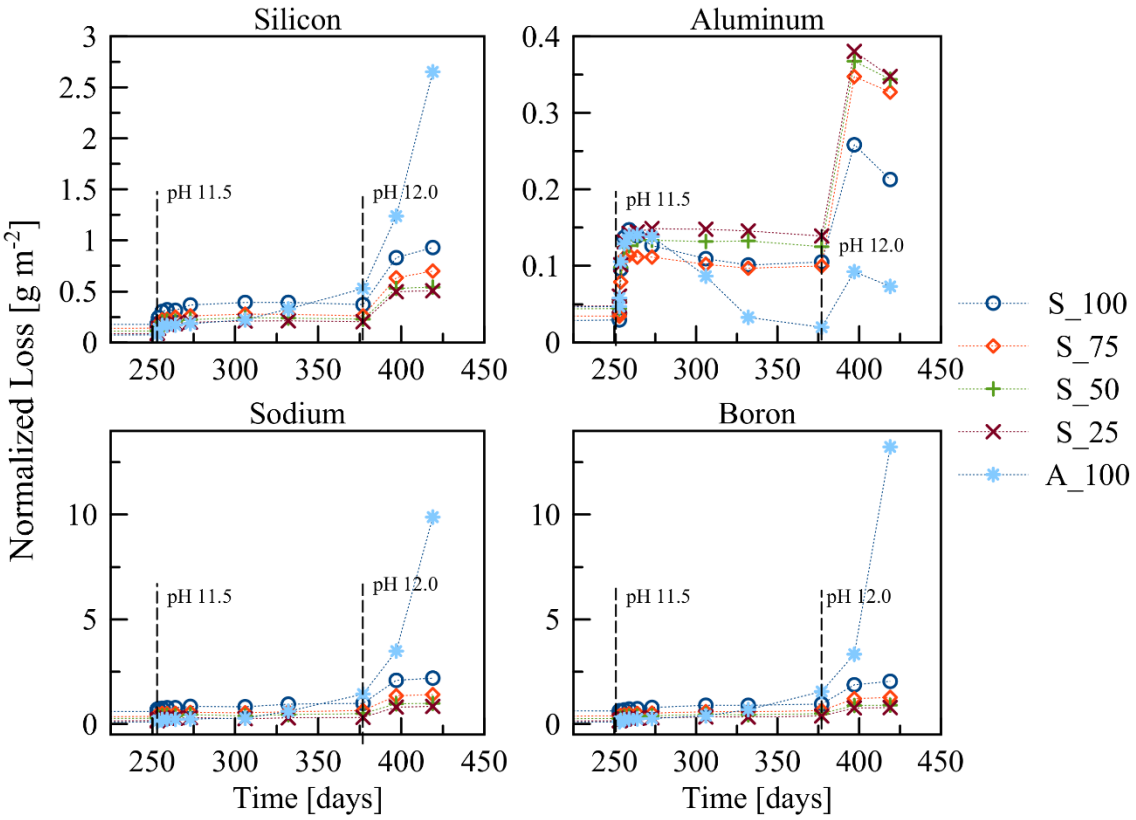

Figure 10. Normalized loss for the PCT ghost samples after increasing the pH to 11.5 (253 days) and pH 12.0 (377 days) with 10 M KOH solution

As observed for the CGS solution data (Figure 6), the drops in aluminum concentrations were met with dramatic increases in concentration for the other elements. In the case of the spiked PCT samples, it is important to note that for S_100, after ~260 days, a ~27% decrease in aluminum concentration occurs which is met by an 11-16% increase in silicon, sodium, and boron concentrations. While for A_100 the ~67% decrease in aluminum concentration is met by an ~62% increase in boron, ~60% increase in sodium, and 42% increase in silicon. The drastic increase in concentrations for the spiked PCT A_100 is characteristic of a Stage III transition.

Based on the strong base-weak acid plot in Figure 10, just before spiking all the glasses hover within the WA region below 0 and below the critical pH 10.7. A_100 is closest to the excess strong base region, with a few points just above neutral. Understandably, after spiking the solution pH increases to the values seen in Figure 8, above pH 10.7. However, the weak acids (silicon, boron, aluminum, Equation 3) dominate the ionic strength of the solution. This suggests the precipitation of minerals which consume Al.

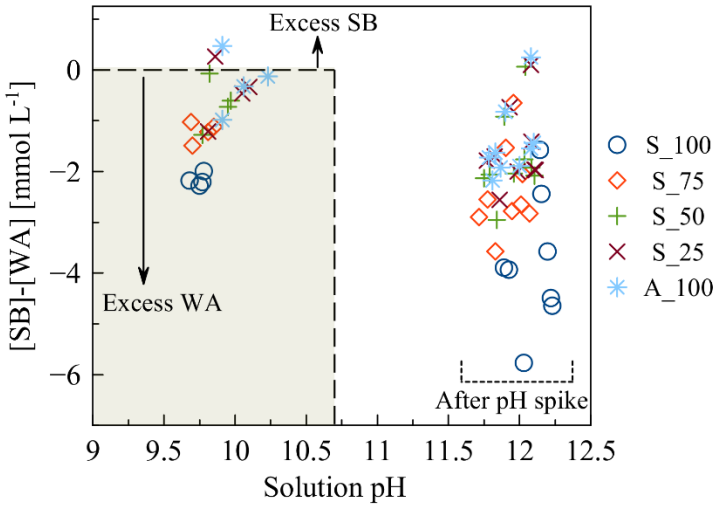

Figure 11. All five glasses hover in the excess weak acid region below pH 10.7 prior to spiking with 10 M L^{-1} solution. Even after the increases to pH 11.5 and 12.0 most of the data remains in the excess weak acid regime

1.1. Characterization

1.1.1. Spiked PCT Powder Characterization

Small amounts of reacted glass powder (<200 mg) were occasionally removed from the spiked PCT-KOH samples and examined with scanning electron microscopy (SEM). The reacted surface was examined specifically for the presence of precipitated crystals and/or clay formations.

Twenty days after spiking with KOH solution (273 days elapsed time), small amounts of powder were removed from each vessel and examined with SEM and XRD. The XRD data displayed an amorphous hump indicating <5% crystallinity. SEM observation confirmed that there were no detectable crystals present on any of the five glasses.

Just before the solution pH for each vessel was increased to pH 12 (377 days elapsed time), solution and powder was removed. A collage of images representing the surface of particles from each composition is shown in Figure 11. A general trend exists with respect to a phyllosilicate clay that densely covers the surface of all S_100 particles, and decreases in density with increasing AFCI content. It is clear that the fuzzy clay covers S_100 and S_75 particles, but noticeably decreases in coverage for the S_50 particles. On the surface of S_25 glass, there are some wisps of the clay formation. For A_100 there is no phyllosilicate present, but there are small some crystalline formations scattered on the surface of the particles. From the solution analysis (Figure 9), it can be assumed that the concentration of elements silicon, sodium, and boron are increasing for A_100 at 378 days, while aluminum concentration is decreasing. At this time too, the surface of most of the A_100 glass particles had some crystalline formations like the inset of Figure 11 shows. X-ray diffraction was performed on these samples as well, with no crystalline patterns detected.

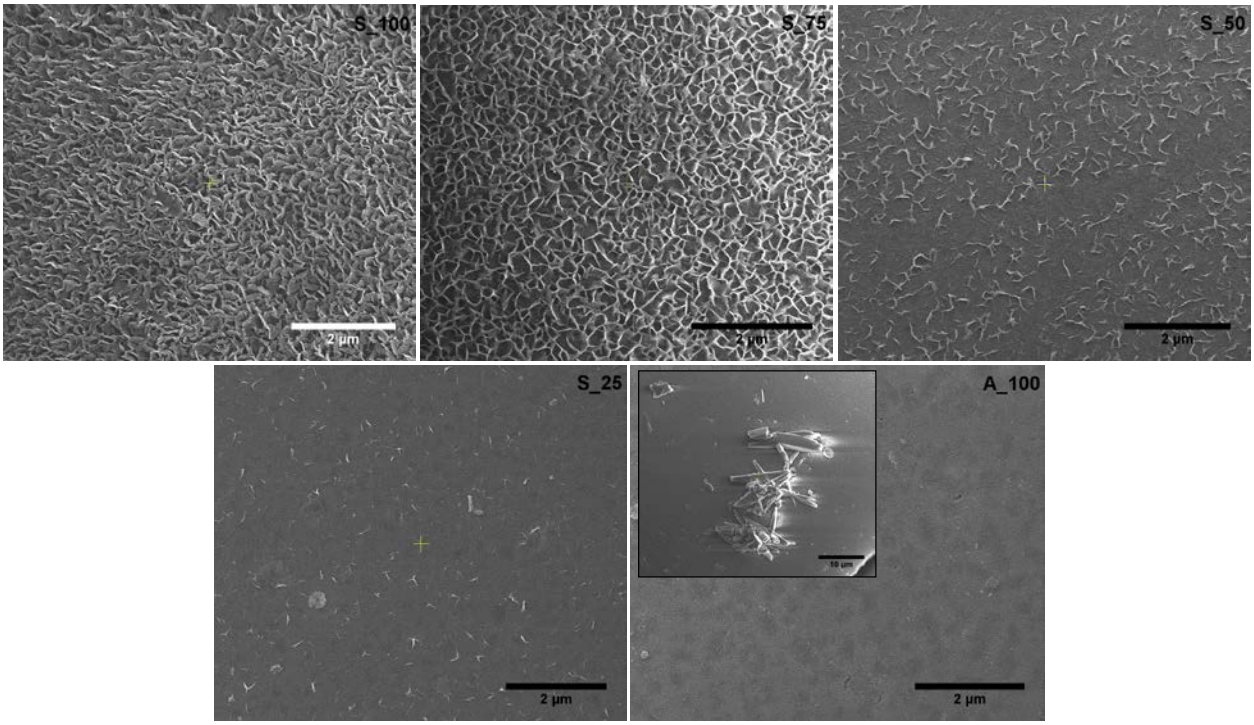

Figure 12. Powder was sampled just before increasing pH a second time to pH 12. The images were taken of powder samples after 124 days (377 days elapsed) in pH 11.5 spiked solution.

After the second pH increase, up to pH 12, A_100 has clearly gone through a Stage III transition by 397 days elapsed time (124 days after the initial solution increase to pH 11.5 and 20 days after increasing the pH to 12.0). The concentrations of silicon, sodium, and boron have increased dramatically (Figure 9) and the surface of the particles are covered in crystalline material (Figure 12).

In Figure 12-B, which shows A_100 particles after 397 days elapsed time, the spherical fibrous balls resemble the small discs that were seen on A_100 20 days after spiking to pH 11.5. Around the edge of these round formations, the underlying glass is severely scoured and cracked, as if the formations were ripping the surface of the glass off. The fibrous needles that were seen in places on particles at 377 days (Figure 11) are seen in more abundance by 397 days. In Figure 12-C, the long needles appear to be imbedded and growing out of the glass surface. They were not detectable by XRD.

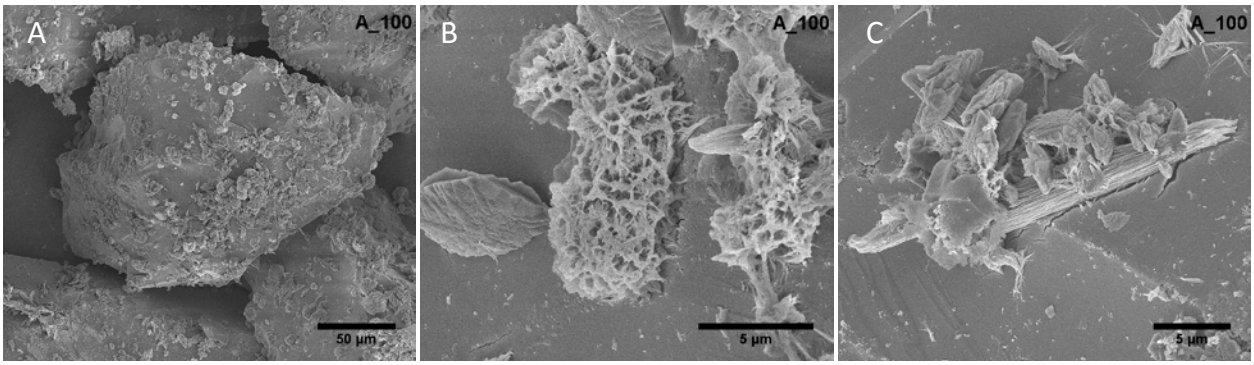

Figure 13. Crystal like formations appeared on the surfaces of A_100 particles 20 days after again increasing solution to pH 12.0, 397 total days.

The glass with the next highest AFCI content, S_25, shows formations very similar to those seen on A_100. Although not in the same quantity, the surface of S_25 particles are speckled with the fibrous spherical clusters as seen in Figure 13-A and B, as well as the needle-like formations in Figure 13-C. Unlike A_100, in Figure 13-C a small amount of phyllosilicate mineral can be seen on the surface of S_25. However, from solution data, it does not appear that S_25 has experienced a Stage III transition.

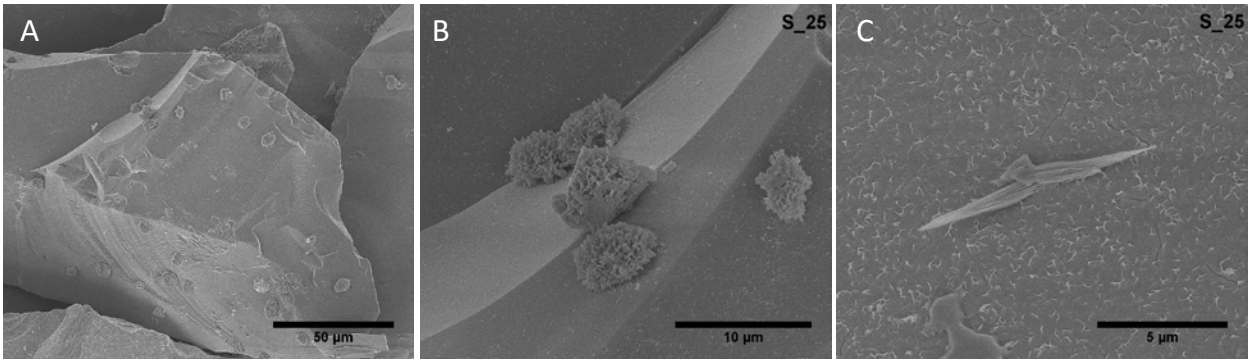

Figure 14. The S_25 sample after 144 days has many similar formations to those seen on A_100 after its Stage III transition.

The other three samples, S_100, S_75, and S_50 do not appear to have changed significantly (Figure 14). The phyllosilicate is still present and densely covers S_100 and S_75, but does not appear to have grown since 124 days on the S_50 sample. The phyllosilicate that covers these samples clearly becomes a dense layer. From the image of S_75 in Figure 14, the dried clay mineral has cracked and separated from the underlying bulk glass, visible in the bottom right corner.

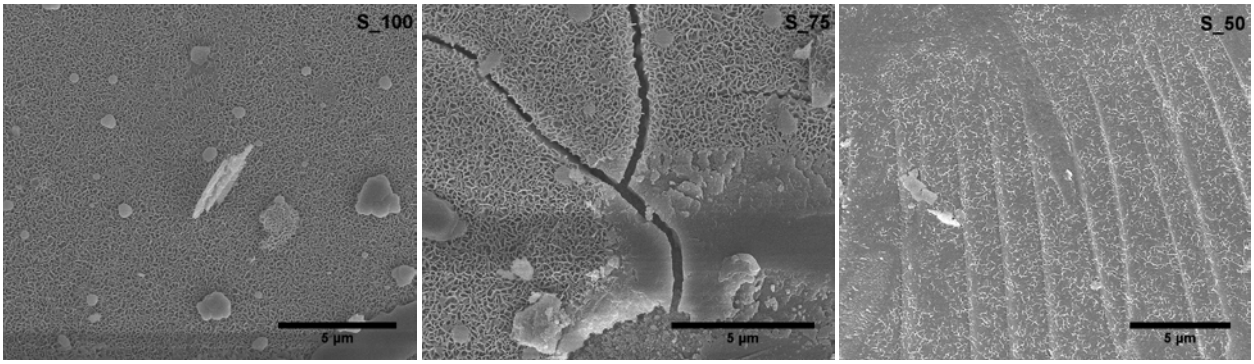

Figure 15. The surfaces of reacted glass particles after 144 days elapsed time in spiked solution.

3.2.1. Concentrated Glass Solution Powder Characterization

At 700 days, powder was removed from all the CGS samples. During this time, S_25 CGS sample was in the midst of a Stage III resumption. The aluminum in solution was at a minimum, and silicon, sodium, and boron was increasing; 78 days later, S_50 would tip into a Stage III transition as well. Images of powder surfaces are shown for each glass composition in Figure 15.

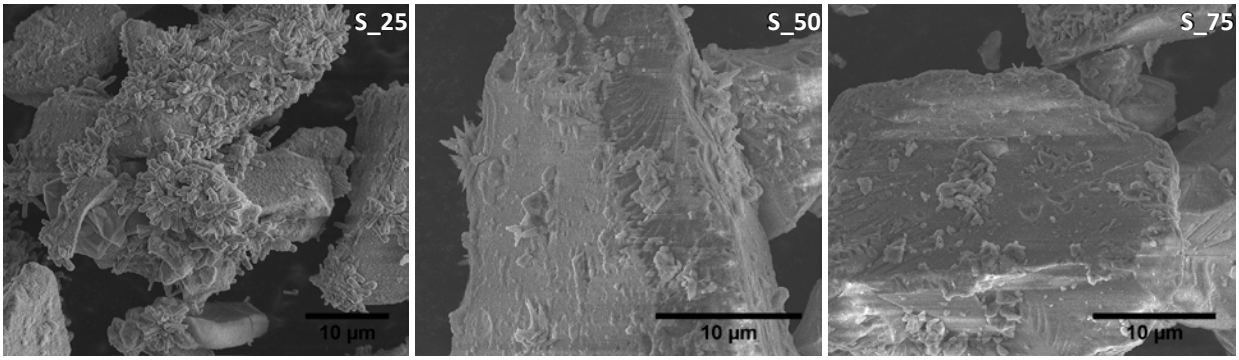

Figure 16. The surface of S_25 is covered in crystal like formations, S_50 has not tipped into Stage III, but there are small amounts of crystal-like formations present, and S_75 is nearly free of all such formations.

The surface of all S_25 glass powder is covered, and nearly encased, in crystal-like formations. Similar looking formations are present on the S_50 glass particles, but not in the same abundance as S_25. In select places there are crystal-like formations on the surfaces of S_75 particles, but most of the glass powder did not have significant features. X-ray diffraction was performed on the 700 day S_25 powder, identifying the formations as Zeolite-P ($Na_{3.6}Al_{3.6}Si_{12.4}O_{32}\bullet 14H_2O$) (Figure 16).

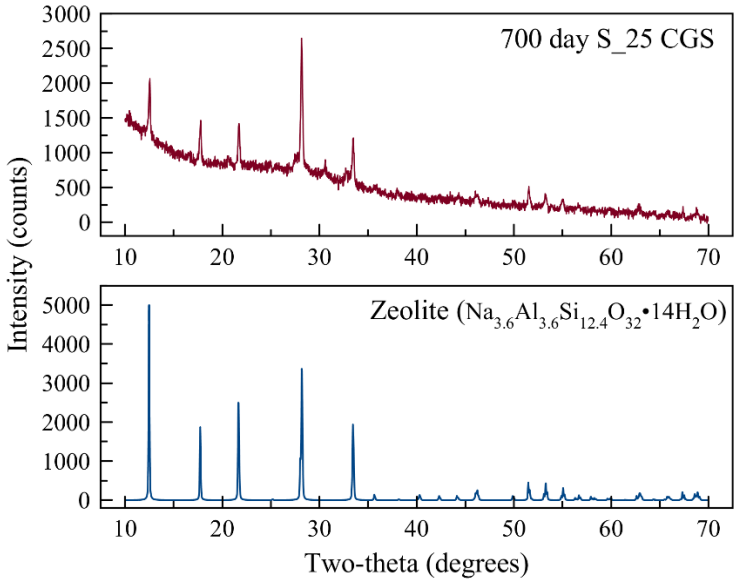

Figure 17. X-ray diffraction pattern of S_25 glass powder from the CGS sample at 700 days identified as Zeolite-P.

Powder was sampled again at 1035 days from all the samples and analyzed with XRD. The same zeolite crystalline phase that was identified at 700 days on S_25 glass was now detected on all three glasses (Figure 17). The peak intensity for peaks 2θ 12.5 and 28.2 are low for S_75, but nonetheless are present. S_75 also only recently transitioned to Stage III (the last CGS blend to transition), and so the crystal formations may not have fully developed.

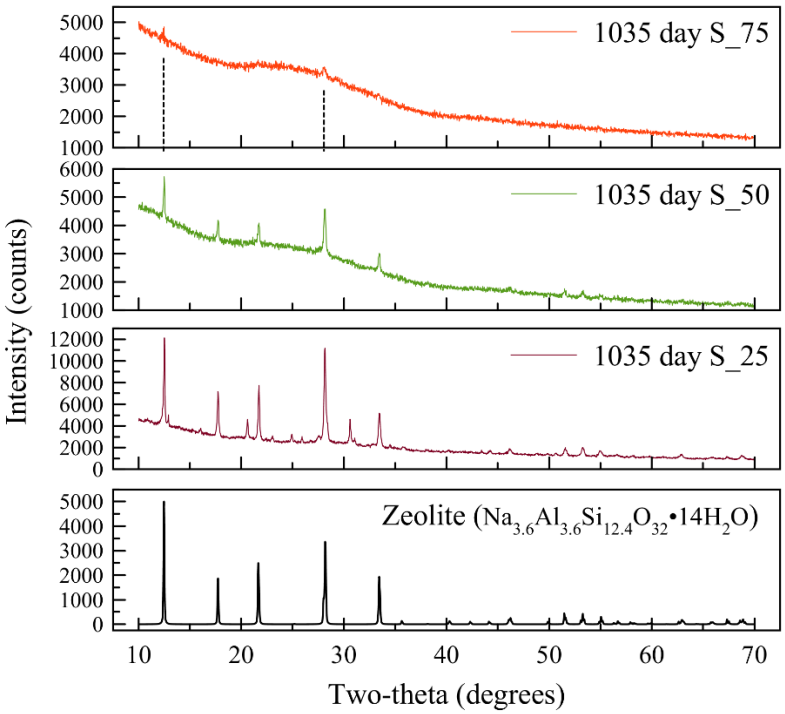

Figure 18. The precipitates on all three CGS powders after 1035 days were confirmed with XRD to be zeolite.

4.0 Discussion

Based on both solution analysis and characterization of the PCT test data, it is clear that none of those samples have experienced a Stage III transition. There was no resumption of alteration observed through the rapid increase of elements in solution (Figure 3) or precipitation of zeolitic-phases. Furthermore, the [SB]-[WA] versus pH plot (Figure 4) confirmed that for all five glasses there was not enough excess strong base, and the pH was too low for a Stage III event relative to the ALTGLASS database.

After the artificial increase of solution pH due to spiking the PCT samples, there was a general increase in soluble species released from each glass. Even after 260 days, however, AFCI is the only glass that exhibits any hint of resumption, with a drop in aluminum and an increase in silicon, sodium, and boron concentrations in solution (Figure 9). The crystals present on the surface of the KOH-spiked A_100 sample (Figure 12) provided further indication that it was on the verge of a Stage III event. It should be recalled that the A_100 glass has the highest concentration of aluminum out of all the glasses (See Appendix A, Table 3).

The three glasses that did experience systematic Stage III transitions were from the Concentrated Glass Solution (CGS) experiments. The solution analysis showed a distinct tipping point in aluminum concentration (~53 ppm) that occurred for all three glasses (Figure 6). Aluminum has been the target of many studies aimed at understanding Stage III because aluminum appears to inhibit or prompt the release of other elements. The inverse relationship between aluminum and silicon in solution is most notable for all the experiments in this study.

It has been proposed that aluminum in solution inhibits glass hydrolysis [11, 12, 13] by reducing the silicon activity at saturation [14] via the "Sorption of aluminum at silanol sites and precipitation as surface aluminum oxyhydroxides… [9]" [15]. Iler proposed that the negatively charged aluminosilicate sites at the surface of amorphous silica prevent the necessary hydroxyl ions from attacking the surface which is required to catalyze silica dissolution [16].

While the higher aluminum content in solution may inhibit the hydrolysis of a glass, aluminum is also a crucial building block for zeolites [17]. Many studies agree that have zeolite is the mineral precipitate associated with and/or responsible for a resumption of alteration (Stage III corrosion). Van Iseghem and Grambow came to a similar conclusion in their study of a Belgian reference waste glass, noting that the high aluminum content in the glass SAN60 (unrelated to SON68) appeared to lower the forward rate. With the low Si/Al ratio, it tended to form the zeolite analcime [18], a common reaction product phase that is common for AFCI and has been known to cause an increase in the dissolution rates of many glasses [9] [19, 20, 21, 22, 23]. In our characterization of reacted CGS glass powder samples with XRD and SEM, the formation and presence of zeolite is apparent, contributing to the sudden drop in aluminum concentration. However, zeolites were not seen on any of the surfaces for reacted SON68 (Figure 14) nor detected with XRD. Others have not found zeolite formation on the surface layers of R7T7 glass [24], the radioactive version of SON68 glass, because these phases are not stable at the lower pH of the leachates characteristic of R7T7 and SON68 glass. The formation of mineral and other crystalline phases, or lack thereof, and differences in pH observed by many workers, are important distinctions between AFCI and SON68, both of which have been observed in the solution analysis and characterization data for SON68 and AFCI in these experiments.

Beyond the differences in these two glasses, there are also noticeable differences between the Concentrated Glass Solution (CGS) and Product Consistency Test (PCT) experiments themselves. Firstly, the transitions and events that occur for all three blends in the CGS experiment with respect to aluminum, and subsequently every other element, are distinctive and very different features from the PCT experimental data. The pH for the CGS solutions was about one-half a pH unit higher than the PCT blend solutions, and roughly 9-15 times greater amounts of aluminum in solution for CGS. Recalling that the surface area to volume ratio (SA/V) is 12.5x greater for CGS could explain the variation, as others have noted the influence of different SA/V ratios on solution and pH behavior [9, 2, 10]. But, it cannot be the single variation used to explain all the differences observed between CGS and PCT experiments.

The raw glass compositions for the CGS experiments (synthesized independently of the PCT glasses) were also measured directly with lithium-metaborate fusion analysis using the same procedure that was performed for the PCT glass samples (Table 3). This revealed that the CGS glass blends had ~2.0-2.5 weight% higher Al_2O_3 than was expected based on calculation; this was likely due to the use of alumina crucibles in the case of the CGS blended glass fabrication. The measured and calculated weight percent for Al_2O_3, Fe_2O_3, Na_2O, and SiO_2 can be seen in Table 5. Aside from the excess aluminum present in the three glass blends, all other elements scale according to the percentages of SON68 and AFCI combined. Note that the SON68 and AFCI source compositions for the CGS blends were melted in platinum-rhodium crucibles.

Table 5. The weight percentages for selected oxides in the CGS glass blends.

Glasses used for Concentrated Glass Solution tests						
Glass		S_100	S_75	S_50	S_25	A_100
Al_2O_3 wt%	Calculated	5.00	6.10	7.19	8.29	9.39
	Meassured	5.34	8.71	9.36	10.7	9.90
*Fe_2O_3 wt%	Calculated	3.03	2.27	1.52	0.76	0.00
	Meassured	3.07	2.16	1.47	0.72	0.00
Na_2O wt%	Calculated	10.2	9.42	8.61	7.81	7.01
	Meassured	10.2	8.97	8.15	7.42	6.83
SiO_2 wt%	Calculated	45.9	47.8	49.8	51.8	53.7
	Meassured	47.0	47.7	49.6	51.6	53.9

With the proposal that SA/V is not the only contributing factor responsible for the Stage III transitions of all three CGS blends, another PCT experiment was performed to independently test the importance of this excess aluminum in the blended compositions. An identical PCT experiment, labeled PCT-xs-Al to differentiate between the PCT-original, PCT-ghost, and PCT-spiked samples, as explained in Section 2.2, was started with the same glasses that were used for the CGS experiment (Appendix C, Table 5). Like the CGS solution data, the aluminum concentration in solution was markedly higher in the new PCT samples with xs-Al blends compared to the aluminum data from the PCT-original samples. In Table 6, the average maximum aluminum concentration is displayed for each glass from the PCT-original, CGS, and PCT-xs-Al experiments. From this data, the PCT-xs-Al samples, with identical 2000 m^{-1} SA/V ratio to PCT-original, had on average 6-10 times greater concentration of aluminum in the blends than the PCT-original aluminum concentration averages.

Table 6. Average aluminum saturation concentration for each experiment and its SA/V ratio.

Experiment	Glass Composition	S/V, m^{-1}	Average aluminum concentration, ppm				
			S_100	S_75	S_50	S_25	A_100
PCT-original	Table 3/Appendix A	2,000	1.16	2.09	3.45	4.56	5.22
CGS	Table 5/Appendix C	25,000	1.26	31.8	31.0	42.2	8.17
PCT (xs-Al)	Table 5/Appendix C	2,000	1.11	21.55	22.49	25.06	5.08

It is evident that the greater SA/V ratio (due to un-sieved powder/fines) in the CGS experiments play a role in the higher solution pH. However, the significance of that role is diminished with the additional knowledge that the PCT- xs-Al experiment with the lower SA/V ratio resulted in markedly higher values of aluminum in solution than the previous PCT-original experiment.

This information points to a potentially critical value of aluminum in the glass composition that promotes excess dissolution of aluminum from the glass network. It is important to mention, too, that the raw unreacted glasses were analyzed with XRD and no crystalline patterns were detected that could indicate a phase separated glass. From the molar ratio of Si/Al in each glass for both batches, shown in Table 7, the critical ratio may be somewhere around 8.0 to 9.0 Si/Al molar ratio in composition.

Table 7. Molar ratio of Si/Al for each glass from both batches and the experiments run with the respective batch.

molar Si/Al ratio	S_100	S_75	S_50	S_25	A_100
CGS, PCT xs-Al Glass	14.5	9.07	8.82	8.02	9.16
PCT-original Glass	15.6	13.3	11.7	10.6	9.71

The ratio of Si/Al in composition has been understood to be an important parameter in the synthesis of zeolites [25]. Increasing the Si/Al parameter from 0.5 to infinity can result in the increase of any number of other parameters, (i.e. acid resistivity, thermal stability, and hydrophobicity) [26] during synthesis of zeolites. Zeolites can form under a vast range of Si/Al ratios, but fast nucleation and growth of zeolite crystals has been seen in aluminum-rich systems [27].

It is worth mentioning again that the CGS blends all transitioned into Stage III corrosion, and occurred at very close to the same aluminum concentration (Table 4). Furthermore, the first blend to transition, S_25, has the highest aluminum concentration out of all the glasses at 10.7 wt% Al_2O_3 (Table 5) and a Si/Al ratio of 8.02. The other two glasses follow in order of decreasing Al_2O_3 compositional percentage, with S_50 transitioning after S_25 and before S_75, which transitions last and consequently has the lowest percentage of Al_2O_3 in composition at 8.71 weight % (Si/Al 9.07).

Along with the importance of aluminum, another key element that plays a role in the formation of secondary phases is iron. Iron, exclusive to the SON68 composition, is present in its respective percentage in the blends S_75, S_50, and S_25, but not in AFCI. It has been observed by others that during corrosion of SON68 and its radioactive glass counterpart, R7T7, zeolitic phases do not form or precipitate in solution. However, as is evident from the SEM images of the characterized PCT powders (Figure 11, Figure 14), a clay-like substance forms a uniform layer that coats the S_100 particles and decreases in coverage with increasing AFCI content. Muller et al. identify this phase, very similar in appearance to the formations on our PCT powders, as the phyllosilicate smectite. A corresponding SEM image along with the EDS spectra of the phyllosilicate smectite layer reported by Muller, et al is shown in Figure 18 [28].

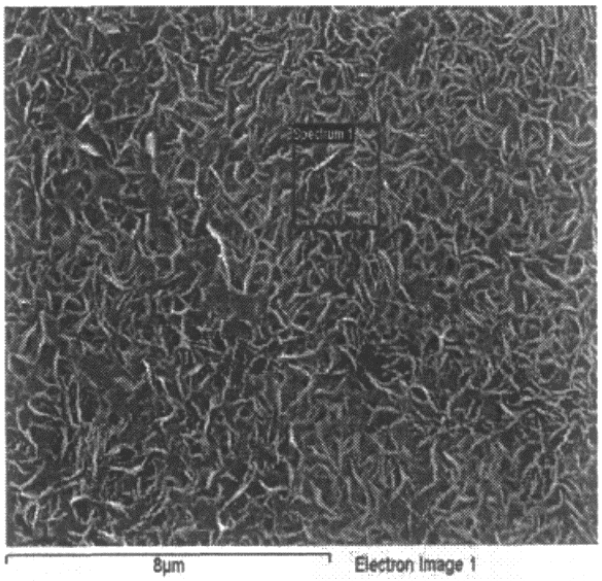

Element	Weight%	Atomic%
Na K	2.39	2.35
Mg K	0.78	0.73
Al K	3.89	3.26
Si K	27.50	22.12
P K	-0.39	-0.28
K K	5.01	2.90
Ca K	0.64	0.36
Fe K	16.26	6.58
O	43.91	62.00
Totals	100.00	

Figure 19. SEM/EDS image of the phyllosilicate layer Muller et al. observed on various glasses.

The phyllosilicate coverage on the surface of SON68 and its blends with AFCI observed in this study has also been reported by others to be a consistent occurrence for SON68 [19] [29, 30, 31]. Some have suggested this layer on the surface of reacted SON68 glass to be “protective”, or “un-protective”, depending on the glass composition and test conditions [32, 33, 34]. In a literature review on the formation of alteration layer effects on waste glass behavior, Feng et al. concluded that, in general, surface layers on glass can slow glass reaction via a barrier, the extent of which is dependent on glass composition, temperature, test conditions and “silicic acid gradient in the surface layers” [35].

It is worth mentioning that Muller et al. noticed that the glasses in their study that exhibited resumption of alteration had zeolite-type aluminosilicates phase in addition to the phyllosilicate on the surface of the glasses. This agrees with the behavior of the CGS blends that had phyllosilicate surface coverage and high aluminum in both the glass and solution. From the PCT spiked solution analysis, the only glass to exhibit any indication that a Stage III event would occur was AFCI, the glass with the highest aluminum content and no iron in the glass composition to form a smectite surface layer. It could be speculated then that the KOH spiked blends would transition to Stage III corrosion if given enough time, but the smectite surface layer served as a barrier for those glasses.

It is important to comment on the morphology of phyllosilicates as sheets of interconnected six member rings of SiO_4^{-4} tetrahedra. The basic structural unit of $Si_2O_5^{-2}$ comes as a result of three out of the four oxygen from each tetrahedra being shared. For most phyllosilicates, OH^- hydroxyl ions are located at the center of six-member rings. Other cations, typically Fe^{+2}, Mg^{+2}, and Al^{+3}, can be bonded to the SiO_4 sheets by sharing the hydroxyl ions in octahedral coordination. The basic structural units and their stacking can be seen in Figure 19. Some workers have observed and characterized the smectite phyllosilicate [28] [31] on glass surfaces, which are made up of tetrahedral-octahedral-tetrahedral sheets with water molecules between the sheets that increase in volume as water is incorporated into the structure [36].

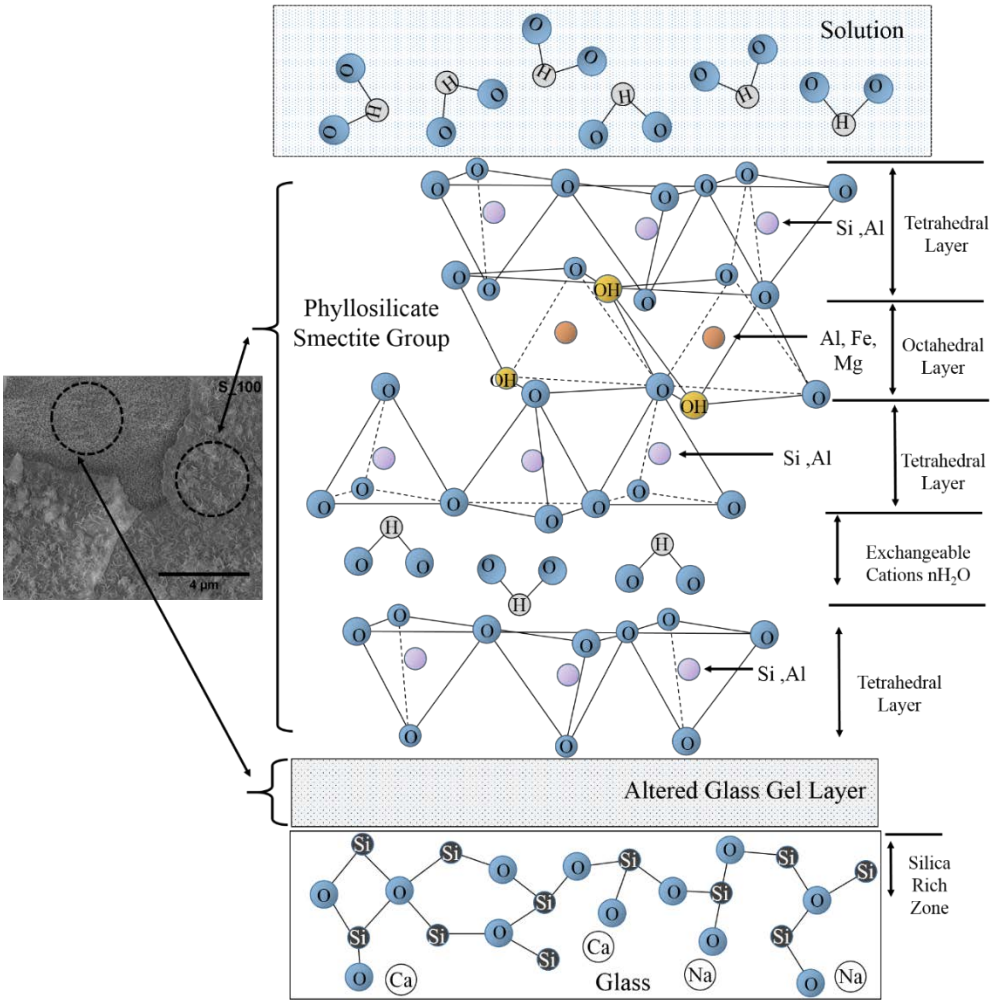

Figure 20. A representation of the basic structural units and stacking of a phyllosilicate (smectite) on an altered gel layer and bulk glass surface in solution. Only four layers are shown, but the structural units repeat (not to scale).

Smectite has the ability to absorb large amounts of water, creating a water tight barrier [37]. With the incorporation of OH^- and water into the octahedral and exchangeable cation layers, it could be that the approach of water molecules and hydrolysis of the bulk glass beneath the layer, is inhibited. The phyllosilicate mineral "sieve" size may be too large to completely stop OH^- (radius ~0.11 nm) and H_2O (radius ~0.138 nm), but saturation of the smectite layer with OH^- could bring the "surface layer" into local equilibrium with the solution. This formation of a dense OH^- saturated phyllosilicate could create a "chemically" protective barrier. It is possible that this barrier at the glass/solution interface, together with a silica-rich altered layer in the underlying glass layer, could contribute to the enhanced durability of SON68 over AFCI and perhaps also explain the systematic time dependence in the Stage III transition of some SON68-AFCI blends.

5.0 Conclusions

The non-radioactive waste glasses, SON68 and AFCI, were synthesized from raw chemical components. By combining these two end-point glasses in different ratios, three blends were also prepared for testing, totaling five-glass compositions. Standard methods of testing glass durability were used for three different experiments, two standard Product Consistency Tests with solution removed at select intervals, and the third was spiked with concentrated KOH solution to increase solution pH. Along with the standard tests, a non-standard Concentrated Glass Solution (CGS) test was performed with the SON68/AFCI glass blends, all three of which transitioned to Stage III.

These unique and systematically varied sets of glass compositions confirmed the critical importance of SA/V, and more so Al content, in promoting the transition to Stage III. The three blends that contained ~2.5 ^{w}/o excess Al_2O_3 and were tested at an SA/V of 25,000 m^{-1}, were the only samples which exhibited the transition to Stage III within the three-year period of this study. Moreover, the solution concentration of Al at the onset of the transition was between 50 and 60 ppm for all three compositions, suggesting a tipping point when the Al concentration reaches this maximum in solution. Equally interesting was the time sequence of the transition for the three glasses; the 25% SON68 composition occurred after 420 days, the 50% SON68 composition after 778 days and the 75% SON68 composition after 905 days. The associated solution data conformed to the ALTGLASS model proposed by Jantzen, while characterization of the sample surfaces suggested the possibility of a smectite OH barrier at the glass/solution interface that formed in proportion to the SON68 concentration in the glass. Altogether, the results suggest the presence of a critical element or elemental concentration in the AFCI glass, or chemical species in solution, that triggers the transition. It is likely associated with Al reaction products in the altered layer, the solution or both. Unfortunately, the identification of this critical constituent or reaction product could not be identified amongst the 20 common and 16 different oxides which constitute SON68 and AFCI.

6.0 References

[1] ASTM1285, "ASTM Standard C 1285-02: Standard Test Methods for Determining Chemical Durability of Nuclear, Hazardous, and Mixed Waste Glasses and Multiphase Glass Ceramics: The Product Consistency Test (PCT)," West Conshohocken, PA, 2008.

[2] C. M. Jantzen and N. E. Bibler, "The Product Consistency Test (PCT): How and Why it Was Developed," *Environmental Issues and Waste Management Technologies in the Materials and Nuclear Industries,* no. XII, 2009.

[3] E. D. Hespe, "Leach Testing of Immobilized Radioactive Waste Solids: A Proposal for a Standard Method," in *Atomic Engery Review*, Vienna, 1971.

[4] M. Fuhrmann, P. F. Pietrzak, J. Heiser, E. M. Franz and P. Columbo, "Accelerated Leach Test for Diffusive Releases from Solidified Waste and a Computer Program to Model Diffusive, Fractional Leaching from Cylindrical Waste Forms," Brookhaven National Laboratory, 1990.

[5] A. Barkatt, S. A. Olszowka, W. Sousanpour, T. Choudhury, Y. Gou, A. Barkatt and R. Adiga, "The Use of Partial-Replenishment Tests in Modeling the Leach Behavior of Glasses," in *Mater. Res. Soc. Symp. Proc.*, 1991.

[6] C. M. Jantzen, C. L. Trivelpiece, C. L. Crawford, J. M. Pareizs and J. B. Pickett, "Accelerated Leach Testing of Glass (ALTGLASS): II. Mineralization of hydrogels by leachate strong bases," *International Journal of Applied Glass Science,* vol. 8, no. 1, pp. 84-96, February 2017.

[7] C. M. Jantzen, K. G. Brown and J. B. Pickett, "Durable Glass for Thousands of Years," *International Journal of Applied Glass Science,* vol. 1, pp. 38-62, 2010.

[8] S. Ribet, I. S. Muller, I. L. Pegg, S. Gin and P. Frugier, "ompositional Effects on the Long-Term Durability of Nuclear Waste Glasses: A Statistical Approach," *Mat. Res. Soc. Symp. Proc.*, p. Vol 824, 2004.

[9] M. Fournier, S. Gin and P. Frugier, "Resumption of Nuclear Glass Alteration: State of the Art," *Journal of Nuclear Materials,* pp. 348-363, 448 (2014).

[10] S. O. Bates, G. F. Piepel and J. W. Johnston, "Leach Testing of Simulated Hanford Waste Vitrification Plant Reference Glass HW-39," Pacific Northwest National Laboratory Report PNL-6884, 1989.

[11] S. Gin, "Control of R7T7 Nuclear Glass Alteration Kinetics Under Saturation Conditions," in *Materials Research Society Proceedings*, 1995.

[12] E. H. Oelkers, "General kinetic description of multioxide silicate mineral and glass dissolution," *Geochimica et Cosmochimica Acta,* vol. 65, no. 21, pp. 3703-3719, 2001.

[13] E. H. Oelkers and S. R. Gislason, "The mechanism, rates and consequences of basaltic glass dissolution: I. An experimental study of the dissolution rates of basaltic glass as a function of

aqueous Al, Si and oxalic acid concentration at 25°C and pH = 3 and 11," *Geochimica et Cosmochimica Acta,* vol. 65, no. 21, pp. 3671-3681, 2001.

[14] N. Rajmohan, P. Frugier and S. Gin, "Composition Effect on Synthetic Glass Alteration Mechanisms: Part 1. Experiments," *Chemical Geology,* vol. 279, no. 3-4, pp. 106-119, 2010.

[15] J. R. Houston, J. L. Herberg, R. S. Mawell and S. A. Carroll, "Association of dissolved aluminum with silica: Connecting molecular structure to surface reactivity using NMR," *Geochimica et Cosmochimica Acta,* vol. 72, no. 14, pp. 3326-3337, 2008.

[16] R. K. Iler, "Effect of adsorbed alumina on the solubility of amorphous silica in water," *Journal of Colloid and Interface Science,* vol. 43, no. 2, pp. 399-408, 1973.

[17] C. M. Jantzen and J. M. Pareizs, "Glass Durability Modeling: Activated Complex Theory (ACT) Expressed by Quasi-Crystalline Structural Ratios (U)," U. S. Department of Energy, Savannah River National Laboratory, Aiken, SC, 2004.

[18] P. Van Iseghem and B. Grambow, "The long-term corrosion and modelling of two simulated Belgian reference high-level waste glasses," in *Mater. Res. Soc. Symp. Proc.*, Volume 112, Pages 631-639 (1988).

[19] W. L. Ebert, J. A. Fortner, A. L. Billings and C. Crawford, "Glass Testing Activities at ANL and SRNL: FY11 Progress Report," Savannah River National Laboratory, 2011.

[20] R. Haaker, G. Malow and P. Offermann, "The Effect of Phase Formation on Glass Leaching," in *Materials Research Society Proceedings,* Jan 1984.

[21] D. M. Strachan and T. L. Croak, "Compositional effects on long-term dissolution of borosilicate glass," *Journal of Non-Crystalline Solids,* vol. 272, pp. 22-33, 2000.

[22] W. L. Ebert, J. K. Bates and W. L. Bourcier, "The Hydration of Borosilicate Waste Glass in Liquid Water and Steam at 200°C," *Waste Management,* vol. 11, pp. 205-221, 1991.

[23] A. J. Bakel, W. L. Ebert and J. S. Luo, "Long-term performace of glasses for Hanford low-level waste," *Ceramic Transactions,* vol. 61, pp. 515-522, 1995.

[24] A. Abdelouas, J.-L. Crovisier, W. Lutze, B. Grambow, J.-C. Dran and R. Muller, "Surface layers on a borosilicate nuclear waste glass corroded in MgCl2 solution," *Journal of Nuclear Materials,* vol. 240, pp. 100-111, 1997.

[25] L. Bieseki, F. G. Penha and S. B. C. Pergher, "Zeolite A synthesis employing a Brazilian coal ash as the silicon and aluminum source and its applications in adsorption and pigment formulation," *Materials Research,* vol. 16, no. 1, 2012.

[26] S. M. Auerbach, K. A. Carrado and P. K. Dutta, Handbook of Zeolite Science and Technology, New York, NY: Marcel Dekker Inc., 2003.

[27] S. Mintova, V. Valtchev, T. Onfroy, C. Marichal, H. Knozinger and T. Bein, "Variation of the Si/Al ratio in nanosized zeolite Beta crystals," *Microporous and Mesoporous Materials,* vol. 90, no. 1-3, pp. 237-245, 2006.

[28] I. S. Muller, S. Ribet, I. L. Pegg, S. Gin and P. Frugier, "Characterization of Alteration Phases on HLW Glasses after 15 Years of PCT Leaching," in *in Environmental Issues and Waste Management Technologies in the Ceramic and Nuclear Industries XI*, Hoboken, NJ, USA., John Wiley & Sons, Inc., 2006.

[29] P. Frugier, S. Gin, J. E. Lartigue and E. Deloule, "Son68 Glass Dissolution Kinetics at High Reaction Progress: Mechanisms Accounting for The Residual Alteration Rate," in *Materials Research Society*, Volume 932 (2006).

[30] S. Gin and J. P. Mestre, "SON 68 nuclear glass alteration kinetics between pH 7 and pH 11.5," *Journal of Nuclear Materials,* vol. 295, no. 1, pp. 83-96, 2001.

[31] W. L. Gong, L. M. Wang, R. C. Ewing, E. Vernaz, J. K. Bates and W. L. Ebert, "Analytical electron microscopy study of surface layers formed on the French SON68 nuclear waste glass during vapor hydration at 200°C," *Journal of Nuclear Materials,* vol. 254, pp. 249-265, 1998.

[32] P. B. Adams, *Materials Research Society Symposium Proceedings,* pp. 115-127, 1988.

[33] W. H. Casey, C. Eggleston, P. A. Johnson, H. R. Westrich and M. F. Hochella, "Aqueous Surface Chemistry and Corrosion of Minerals," *Materials Research Society Bulletin,* vol. 5, no. 17, pp. 23-29, 1992.

[34] L. L. Hench, *Materials Research Society Symposium Proceedings,* vol. 125, pp. 189-200, 1988.

[35] X. Feng, J. C. Cunnane and J. K. Bates, "A Literature Review of Surface Alteration Later Effects on Waste Glass Behavior," in *American Ceramic Society*, Cincinnati, Ohio, 1993.

[36] S. A. Nelson, "Phyllosilicates (Micas, Chlorite, Talc, & Serpentine)," 18 Aug 2015. [Online]. Available: http://www.tulane.edu/~sanelson/eens211/phyllosilicates.htm. [Accessed 2016].

[37] W. K. Tong, "Introduction to Clay Minerals & Soils," 2000. [Online]. Available: http://www.oakton.edu/user/4/billtong/eas100/clays.htm. [Accessed 2016].

[38] C. M. Jantzen , N. E. Bibler, D. C. Beam, W. G. Ramsey and B. J. Waters, "Nuclear Waste Glass Product Consistency Test (PCT) Version 5.0(U)," Westinghouse Savannah River Company , 1992.

Appendix A

Table 8. Composition in weight and molar percent for nominal SON68, AFCI, and the blends used for the Product Consistency Test

			Weight% and Mol% of SON68 and AFCI Blends											
	Percent SON68		100%	75%	50%	25%	0%	100%	75%	50%	25%	0%		
	Percent AFCI		0%	25%	50%	75%	100%	0%	25%	50%	75%	100%		
	Oxide	MW, g/mol	weight%	weight%	weight%	weight%	weight%	mol%	mol%	mol%	mol%	mol%		
	Ag_2O	231.7	0.03%	0.03%	0.04%	0.04%	0.04%	0.01%	0.01%	0.01%	0.01%	0.01%		
	Al_2O_3	102.0	5.00%	6.10%	7.19%	8.29%	9.39%	3.39%	4.07%	4.74%	5.39%	6.02%		
	B_2O_3	69.6	14.14%	13.02%	11.90%	10.78%	9.66%	14.03%	12.74%	11.48%	10.26%	9.07%		
	BaO	153.3	0.62%	0.68%	0.73%	0.79%	0.85%	0.28%	0.30%	0.32%	0.34%	0.36%		
	CaO	56.1	4.07%	4.30%	4.54%	4.77%	5.01%	5.01%	5.23%	5.44%	5.64%	5.83%		
	CdO	128.4	0.03%	0.03%	0.04%	0.04%	0.04%	0.02%	0.02%	0.02%	0.02%	0.02%		
	Ce_2O_3	328.2	0.97%	1.03%	1.08%	1.14%	1.19%	0.20%	0.21%	0.22%	0.23%	0.24%		
	Cs_2O	281.8	1.12%	1.12%	1.11%	1.11%	1.11%	0.27%	0.27%	0.27%	0.26%	0.26%		
	La_2O_3	325.8	0.93%	0.85%	0.77%	0.69%	0.61%	0.20%	0.18%	0.16%	0.14%	0.12%		
	Li_2O	29.9	1.99%	2.62%	3.25%	3.88%	4.50%	4.60%	5.97%	7.30%	8.59%	9.85%		
	MoO_3	143.9	1.78%	1.71%	1.64%	1.57%	1.50%	0.85%	0.81%	0.77%	0.72%	0.68%		
	Na_2O	62.0	10.22%	9.42%	8.61%	7.81%	7.01%	11.39%	10.35%	9.34%	8.35%	7.39%		
	Nd_2O_3	336.5	2.04%	2.03%	2.03%	2.02%	2.01%	0.42%	0.41%	0.40%	0.40%	0.39%		
	Pr_2O_3	329.8	0.46%	0.48%	0.51%	0.53%	0.56%	0.10%	0.10%	0.10%	0.11%	0.11%		
	SiO_2	60.1	45.85%	47.82%	49.78%	51.75%	53.72%	52.73%	54.21%	55.66%	57.06%	58.43%		
	SnO_2	150.7	0.02%	0.02%	0.02%	0.03%	0.03%	0.01%	0.01%	0.01%	0.01%	0.01%		
	SrO	103.6	0.35%	0.36%	0.36%	0.37%	0.38%	0.23%	0.23%	0.24%	0.24%	0.24%		
	TeO_2	159.6	0.23%	0.24%	0.24%	0.25%	0.25%	0.10%	0.10%	0.10%	0.10%	0.10%		
	Y_2O_3	225.8	0.20%	0.21%	0.22%	0.23%	0.24%	0.06%	0.06%	0.07%	0.07%	0.07%		
	ZrO_2	123.2	2.75%	2.35%	1.95%	1.55%	1.15%	1.54%	1.30%	1.06%	0.83%	0.61%		
Exclusive to SON68	Cr_2O_3	*152.0*	*0.53%*	*0.40%*	*0.27%*	*0.13%*	*0.00%*	*0.24%*	*0.18%*	*0.12%*	*0.06%*	*0.00%*		
	Fe_2O_3	*159.7*	*3.03%*	*2.27%*	*1.52%*	*0.76%*	*0.00%*	*1.31%*	*0.97%*	*0.64%*	*0.31%*	*0.00%*		
	MnO_2	*86.9*	*0.39%*	*0.29%*	*0.20%*	*0.10%*	*0.00%*	*0.31%*	*0.23%*	*0.15%*	*0.07%*	*0.00%*		
	NiO	*74.7*	*0.43%*	*0.32%*	*0.22%*	*0.11%*	*0.00%*	*0.40%*	*0.29%*	*0.19%*	*0.10%*	*0.00%*		
	P_2O_5	*141.9*	*0.29%*	*0.22%*	*0.15%*	*0.07%*	*0.00%*	*0.14%*	*0.10%*	*0.07%*	*0.03%*	*0.00%*		
	ZnO	*81.4*	*2.53%*	*1.90%*	*1.27%*	*0.63%*	*0.00%*	*2.15%*	*1.59%*	*1.04%*	*0.51%*	*0.00%*		
Exclusive to AFCI	Eu_2O_3	*351.9*	*0.00%*	*0.02%*	*0.03%*	*0.05%*	*0.07%*	*0.00%*	*0.00%*	*0.01%*	*0.01%*	*0.01%*		
	Gd_2O_3	*362.5*	*0.00%*	*0.02%*	*0.03%*	*0.05%*	*0.06%*	*0.00%*	*0.00%*	*0.01%*	*0.01%*	*0.01%*		
	Rb_2O	*186.9*	*0.00%*	*0.04%*	*0.08%*	*0.12%*	*0.16%*	*0.00%*	*0.01%*	*0.03%*	*0.04%*	*0.06%*		
	RhO_2	*134.9*	*0.00%*	*0.01%*	*0.01%*	*0.02%*	*0.03%*	*0.00%*	*0.00%*	*0.01%*	*0.01%*	*0.01%*		
	SeO_2	*111.0*	*0.00%*	*0.01%*	*0.02%*	*0.02%*	*0.03%*	*0.00%*	*0.00%*	*0.01%*	*0.01%*	*0.02%*		
	Sm_2O_3	*348.7*	*0.00%*	*0.10%*	*0.21%*	*0.31%*	*0.41%*	*0.00%*	*0.02%*	*0.04%*	*0.06%*	*0.08%*		

Appendix B:

Differential Scanning Calorimetry plots for pure SON68 and AFCI glasses

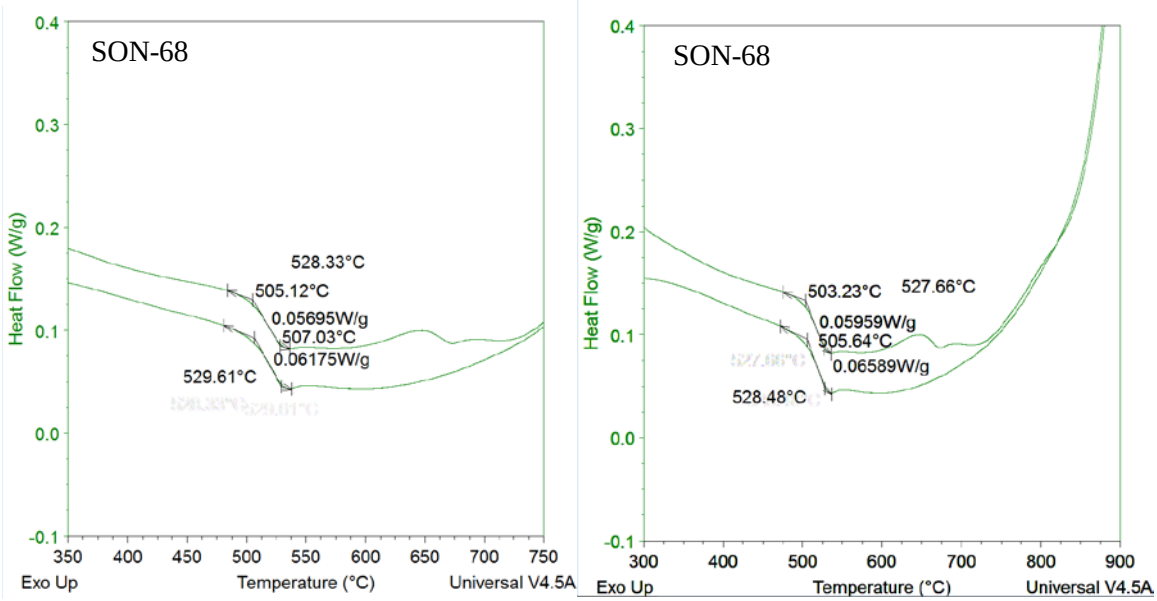

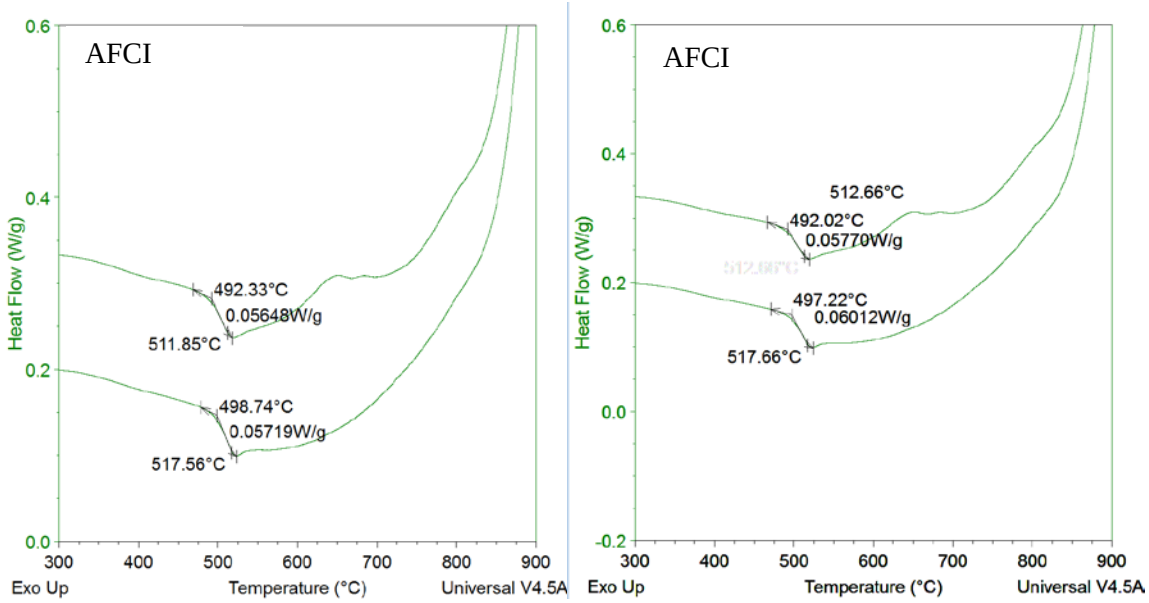

Appendix C:

Table 9. Composition in weight and molar percent for SON68, AFCI, and the blends, used for the Concentrated Glass Solution experiments, values corrected with respect to the actual aluminum content

			Weight% and Mol% of SON68 and AFCI for corrected Al2O3 weight%											
		Percent SON68	100%	75%	50%	25%	0%	100%	75%	50%	25%	0%		
		Percent AFCI	0%	25%	50%	75%	100%	0%	25%	50%	75%	100%		
	Oxide	MW, g/mol	weight%	weight%	weight%	weight%	weight%	mol%	mol%	mol%	mol%	mol%		
	Ag_2O	231.74	0.03%	0.03%	0.03%	0.04%	0.04%	0.01%	0.01%	0.01%	0.01%	0.01%		
	Al_2O_3	101.96	**5.34%**	**8.70%**	**9.36%**	**10.67%**	**9.90%**	3.62%	5.87%	6.21%	7.00%	6.36%		
	B_2O_3	69.62	14.09%	12.66%	11.62%	10.50%	9.60%	14.00%	12.50%	11.30%	10.08%	9.03%		
	BaO	153.33	0.62%	0.66%	0.72%	0.77%	0.84%	0.28%	0.30%	0.32%	0.34%	0.36%		
	CaO	56.08	4.06%	4.18%	4.43%	4.65%	4.98%	5.00%	5.13%	5.35%	5.54%	5.81%		
	CdO	128.41	0.03%	0.03%	0.04%	0.04%	0.04%	0.02%	0.02%	0.02%	0.02%	0.02%		
	Ce_2O_3	328.23	0.97%	1.00%	1.06%	1.11%	1.19%	0.20%	0.21%	0.22%	0.23%	0.24%		
	Cs_2O	281.81	1.12%	1.09%	1.09%	1.08%	1.10%	0.27%	0.26%	0.26%	0.26%	0.26%		
	La_2O_3	325.81	0.93%	0.83%	0.75%	0.67%	0.60%	0.20%	0.17%	0.16%	0.14%	0.12%		
	Li_2O	29.88	1.98%	2.55%	3.17%	3.78%	4.48%	4.59%	5.86%	7.19%	8.45%	9.82%		
	MoO_3	143.94	1.77%	1.66%	1.60%	1.53%	1.49%	0.85%	0.79%	0.75%	0.71%	0.68%		
	Na_2O	61.98	10.18%	9.16%	8.41%	7.61%	6.97%	11.37%	10.16%	9.19%	8.21%	7.36%		
	Nd_2O_3	336.48	2.03%	1.98%	1.98%	1.97%	2.00%	0.42%	0.40%	0.40%	0.39%	0.39%		
	Pr_2O_3	329.81	0.46%	0.47%	0.50%	0.52%	0.55%	0.10%	0.10%	0.10%	0.11%	0.11%		
	SiO_2	60.08	45.69%	46.49%	48.62%	50.41%	53.42%	52.60%	53.20%	54.79%	56.09%	58.22%		
	SnO_2	150.71	0.02%	0.02%	0.02%	0.02%	0.03%	0.01%	0.01%	0.01%	0.01%	0.01%		
	SrO	103.62	0.35%	0.35%	0.36%	0.36%	0.38%	0.23%	0.23%	0.23%	0.23%	0.24%		
	TeO_2	159.60	0.23%	0.23%	0.24%	0.24%	0.25%	0.10%	0.10%	0.10%	0.10%	0.10%		
	Y_2O_3	225.81	0.20%	0.20%	0.22%	0.23%	0.24%	0.06%	0.06%	0.06%	0.07%	0.07%		
	ZrO_2	123.22	2.74%	2.28%	1.90%	1.51%	1.14%	1.54%	1.27%	1.05%	0.82%	0.61%		
Exclusive to SON68	*Cr_2O_3*	*151.99*	0.53%	0.39%	0.26%	0.13%	0.00%	0.24%	0.17%	0.12%	0.06%	0.00%		
	Fe_2O_3	*159.69*	3.02%	2.21%	1.48%	0.74%	0.00%	1.31%	0.95%	0.63%	0.31%	0.00%		
	MnO_2	*86.94*	0.39%	0.28%	0.19%	0.09%	0.00%	0.31%	0.22%	0.15%	0.07%	0.00%		
	NiO	*74.69*	0.43%	0.31%	0.21%	0.10%	0.00%	0.40%	0.29%	0.19%	0.09%	0.00%		
	P_2O_5	*141.94*	0.29%	0.21%	0.14%	0.07%	0.00%	0.14%	0.10%	0.07%	0.03%	0.00%		
	ZnO	*81.39*	2.52%	1.84%	1.24%	0.62%	0.00%	2.14%	1.56%	1.03%	0.51%	0.00%		
Exclusive to AFCI	*Eu_2O_3*	*351.93*	0.00%	0.02%	0.03%	0.05%	0.07%	0.00%	0.00%	0.01%	0.01%	0.01%		
	Gd_2O_3	*362.50*	0.00%	0.02%	0.03%	0.05%	0.06%	0.00%	0.00%	0.01%	0.01%	0.01%		
	Rb_2O	*186.94*	0.00%	0.04%	0.08%	0.12%	0.16%	0.00%	0.01%	0.03%	0.04%	0.06%		
	RhO_2	*134.90*	0.00%	0.01%	0.01%	0.02%	0.03%	0.00%	0.00%	0.01%	0.01%	0.01%		
	SeO_2	*110.96*	0.00%	0.01%	0.02%	0.02%	0.03%	0.00%	0.00%	0.01%	0.01%	0.02%		
	Sm_2O_3	*348.72*	0.00%	0.10%	0.20%	0.30%	0.41%	0.00%	0.02%	0.04%	0.06%	0.08%		